PREDICTIVE CURRENT CONTROL OF PERMANENT MAGNET SYNCHRONOUS MOTOR FOR ELECTRIC VEHICLES

By Anisha Bheemolla

A Thesis
Submitted in Partial Fulfillment
of the Requirements for the Degree of
Master of Science
in Electrical Engineering

Northern Arizona University
December 2023

Approved:
Venkata Yaramasu, Ph.D., Chair
Truong Nghiem, Ph.D.
Rodolfo Echavarria Solis, Ph.D.

ABSTRACT

PREDICTIVE CURRENT CONTROL OF PERMANENT MAGNET SYNCHRONOUS MOTOR FOR ELECTRIC VEHICLES

ANISHA BHEEMOLLA

Electric vehicles (EVs) are becoming more popular and dominating internal combustion engine vehicles from a decade due to high efficiency, low emissions, high reliability, high availability, increased cost competitiveness, and improved vehicle ranges. Permanent magnet synchronous motors and two-level voltage source inverter are now a days popularly used in the EVs.

The digital control methods for traction inverter and motor improve the overall efficiency and performance of an EV and increase the range of EV for the given battery power. In the majority of commercial EVs, the linear control method such as maximum torque per ampere (MTPA) control with proportional-integral regulators and space vector modulation is a proven solution to control the interior permanent magnet synchronous motors with constant switching frequency and minimal steady-state errors. Despite the known control theory, the nonlinearities cannot be incorporated into the linear controllers. The low switching frequency operation of traction inverters lead to sluggish transient response. Moreover, proportional-integral regulators are highly sensitive to the parameter variations.

More advanced control methods are needed to increase the energy conversion efficiency and dynamic performance of permanent magnet synchronous motor in EV applications. Among the class of nonlinear control methods, predictive current control method gained attention in power electronics community as an attractive alternative to the classical linear control. This is due to many superior characteristics such as intuitive concept, digital

controller friendliness, fast dynamic response, and ability to handle constraints and nonlinearities. Due to the absence of modulator, the switching frequency becomes variable with the predictive current control method leading to high current ripples in steady-state.

To solve the variable switching frequency problem of classical predictive current control method, this thesis proposes an innovative control method named modulated model predictive current control (M^2PCC). The design concepts of classical MTPA control, space vector modulation, and classical predictive current control are integrated to create the suggested control system, preserving the best characteristics from each class. The proposed M^2PCC method produces fixed switching frequency operation and low current ripples in steady-state similar to that of classical MTPA control, and fast transient response similar to that of classical predictive current control method. Moreover, a matrix factorization method is developed for high-accuracy discrete-time models of motor. In contrary to the classical predictive current control method which selects optimal voltage vector of inverter as an actuation, the proposed method selects optimal sector of inverter as an actuation. The two active voltage vectors and a zero-voltage vector in the optimal sector are synthesized by the modulation stage consisting of seven-segment switching sequence.

Through MATLAB simulations on an interior permanent magnet synchronous motor-based EV system, the proposed control method is validated during transient and steady-state conditions. The proposed method is also compared with the classical predictive current control method. The findings show that the proposed control method helps to meet the requirements of EV operation, including torque and speed control and current control with superior power quality.

In simple words, this thesis discusses an innovative control method for EVs to improve the overall control performance and power conversion efficiency, and enable higher driving range for the given battery power.

ACKNOWLEDGEMENTS

I would like to explicit my heartfelt gratitude to the following people who have performed an enormous function in the crowning glory of this thesis:

First and foremost, I am immensely thankful to my thesis supervisor, Dr. Venkata Yaramasu, for your guidance, support, and invaluable insights throughout the research process. Your expertise and encouragement have been instrumental in shaping this work. My entire adventure in the United States would not have been possible without your leadership, and I will always be thankful. I genuinely appreciate your work ethic and the numerous hours you spent motivating me toward this outcome.

I would like to extend my appreciation to the members of my thesis committee, Dr. Venkata Yaramasu, Dr. Truong Nghiem, and Prof. Rodolfo Echavarria Solis, for the constructive feedback and valuable suggestions that have helped to improve the quality of this thesis.

My deepest thanks go to my family for their unwavering support, love, and understanding during my academic journey. I owe a debt of gratitude to my husband, Mr. Surender Rana, for his encouragement and belief in my abilities. Their encouragement and sacrifices have been the foundation of my success and sustained me through the challenges of this journey.

I would like to acknowledge my peers and colleagues Alexander Dahlmann and Ai Zhang for their discussions, brainstorming sessions, and the exchange of ideas that have enriched my research. Thanks for their assistance with equipment, software, and technical issues that arose during the research.

Finally, I am grateful to Northern Arizona University for providing me financial support by offering the GTA role. Your investment in my education has been essential. Thanks for providing access to resources, facilities that facilitated my research.

TABLE OF CONTENTS

LIST OF TABLES

LIST OF FIGURES

GLOSSARY OF ACRONYMS

2L	Two-Level
3L	Three-Level
AC	Alternating Current
BEV	Battery Electric Vehicle
BLDC	Brushless DC
DBPCC	Deadbeat Predictive Current Control
DC	Direct Current
DTC	Direct Torque Control
EV	Electric Vehicle
FCS-MPC	Finite Control Set-Model Predictive Control
FECI	Fuel Cell Electric Vehicle
FOC	Field-Oriented Control
HEV	Hybrid Electric Vehicle
ICE	Internal Combustion Engine
IGBT	Insulated Gate Bipolar Transistor
IM	Induction Motor
IPMSM	Interior Permanent Magnet Synchronous Motor
Li-Ion	Lithium-Ion
LTV	Linear Time-Variant
M^2PCC	Modulated Model Predictive Current Control
MPC	Model Predictive Control
MTPA	Maximum Torque Per Ampere
MOSFET	Metal-Oxide-Semiconductor Field-Effect Transistor
NiMH	Nickel-Metal Hybrid Batteries
NPC	Neutral Point Clamped

PCC	Predictive Current Control
PHEV	Plug-in Hybrid Electric Vehicle
PI	Proportional-Integral
PWM	Pulse Width Modulation
SiC	Silicon Carbide
SPMSM	Surface-Mount Permanent Magnet Synchronous Motor
SRM	Switched Reluctance Motors
SS	Steady-State
SVM	Space Vector Modulation
THD	Total Harmonic Distortion
V/f	Voltage and Frequency
VOC	Voltage-Oriented Control
VSI	Voltage Source Inverter
ZOH	Zero-Order Hold

CHAPTER 1

INTRODUCTION

1.1 History of Electric Vehicles

Exploiting clean and renewable energy has become a vital concern as environmental issues get more serious around the world. Vehicles are an essential part of modern society's transportation device, however, they're additionally certainly one of the most important contributors of pollution. The electric powered car is one way to decrease emissions. According to the Energy Policy Act of 1992 [1], electricity qualifies as an opportunity to gasoline. Natural gasoline, coal, nuclear, wind, hydropower, solar, and other energy resources can all be used to generate electricity, which can then be stored as hydrogen or in batteries. Electric vehicles (EVs) have the ability to take power from off-board electrical power sources, typically the electricity grid, and store that power for later use.

A blacksmith from Vermont was among the American and European inventors who experimented with the idea of a battery-powered vehicle in the early 1800s and built some of the earliest small-scale electric cars. Even though Robert Anderson, a British inventor, created the first rudimentary electric carriage around this time, some of the first functional electric cars weren't created by French and English inventors until the second half of the 19th century. The first successful electric car in the United States was built in 1890 by William

Morrison, a scientist from Des Moines, Iowa. His six-passenger vehicle, which could reach a top speed of 14 mph, was essentially an electrified wagon, but it contributed to the interest in electric cars. The following few years saw the emergence of electric automobiles from various manufacturers all around the country. Even a fleet of more than 60 electric taxis existed in New York City. EVs reached their peak in 1900, making up around one-third of all vehicles on the road. Early in the 20th century, there was a global fall in the usage of battery EVs (BEVs) as private motor vehicles due to their high cost, limited peak speed, and short range when compared to internal combustion engine (ICE) cars.

Over the past 10 years, there has been a noticeable growth in demand for EVs due to growing environmental concerns, more model availability, higher cost competitiveness with ICE vehicles, and longer vehicle ranges. Sales of new electric, plug-in hybrid electric, and hybrid vehicles are anticipated to increase by 19% of vehicle sales in 2050 from just 4% in 2017, according to the energy information administration's Annual Energy Outlook [2]. The graph representing EV sales worldwide from 2015 to 2040 is shown in Fig. 1.1 [3] and compared with the ICE vehicle sales.

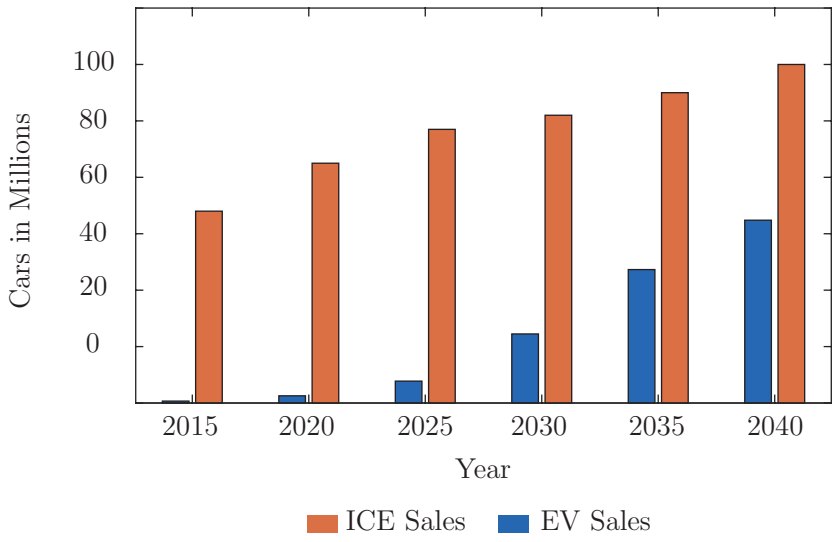

Figure 1.1: Growth in EV sales [3].

1.2 Classification of Electric Vehicles

With models offered in a variety of vehicle types, from compact cars and sedans to sport utility vehicles and pickup trucks, the EV market is expanding quickly. Some EVs run exclusively on batteries, while others are hybrid models that combine an ICE and an electric motor. An overview of EV types is provided in this section. The different kinds of electric cars available in the market are described below [4].

1.2.1 Hybrid Electric Vehicles

A hybrid vehicle that combines an electric propulsion system with a traditional ICE system is known as a hybrid EV (HEV) or also called hybrid vehicle drivetrain. The use of an electric powertrain aims to produce either higher performance or better fuel economy than a traditional car [5]. There are various HEV kinds, and each one differs in how much it functions as an EV. While hybrid electric buses, boats, cars, and tractors are all available, hybrid electric cars are the most popular type of HEV. Present HEVs use efficiency-enhancing technologies like regenerative braking, which transform the kinetic energy of the vehicle into electric energy, which is then stored in a battery or super capacitor. A motor-generator is a type of HEV that uses an ICE to drive an electrical generator, which in turn powers the vehicle's electric motors or recharges its batteries. Given that the hybrid's gasoline engine is often smaller than that of a gasoline-powered vehicle, an HEV emits fewer tailpipe emissions than a gasoline automobile of comparable size [4]. The engine can be geared to run at maximum efficiency if it is not directly needed to move the vehicle, thereby enhancing fuel economy. Based on how electricity is delivered to the drivetrain, hybrid electric cars can be further divided into the following categories [6]: parallel hybrid, series hybrid and series-parallel hybrid.

Parallel Hybrid Electric Vehicles: In parallel hybrids, the ICE and the electric motor are both attached to the mechanical transmission and are capable of concurrently transmitting power to drive the wheels, often through a standard transmission. Production parallel hybrids include the integrated motor assist system from Honda, which is installed in the Insight, Civic, and Accord models, and the belted alternator/starter system from General Motors, which is installed in the Chevrolet Malibu hybrids [7]. The block diagram for parallel hybrid EV is shown in Fig. 1.2.

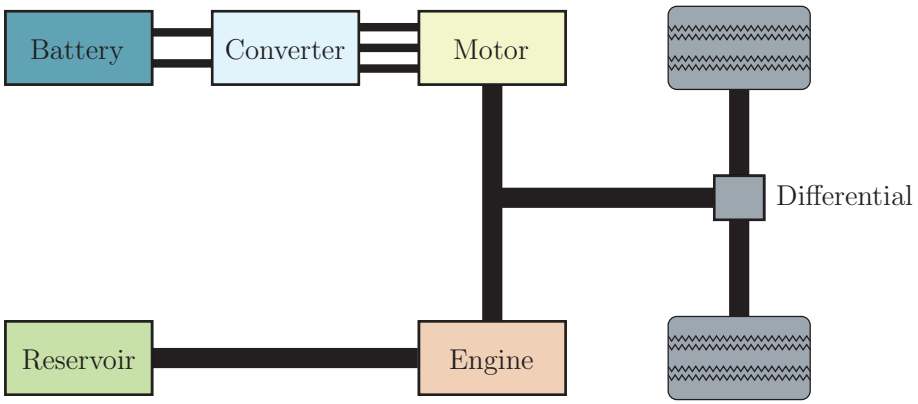

Figure 1.2: Schematic for parallel hybrid EV [7].

Several parallel hybrids have an ICE that can also function as a generator to provide alternative charging. Since the electric motor is designed to assist the primary engine rather than serve as the only source of motive power from launch, commercialized parallel hybrids as of 2013 use a full-sized combustion engine along with a single, tiny (20 kW) electric motor and small battery pack [6]. Parallel hybrids with more than 50 kW will be available after 2015, allowing for electric drive at moderate acceleration. Parallel hybrids are more efficient than comparable non-hybrid cars, especially on highways and in urban stop-and-go traffic when the electric motor is allowed to participate. One advantage of HEVs is their relatively fast refueling time compared to the longer charging times of traditional EVs. Examples for parallel hybrid EVs are Honda Insight, Chevy Malibu and Toyota Prius.

Series Hybrid Electric Vehicles: In series hybrids, the drivetrain is only propelled by an electric motor, and a smaller ICE, sometimes known as a range extender, serves as a generator to power the electric motor or to recharge the batteries [7]. They cost more than parallel hybrids because they often feature a bigger battery pack [6]. The basic schematic of series hybrid EV is shown in Fig. 1.3.

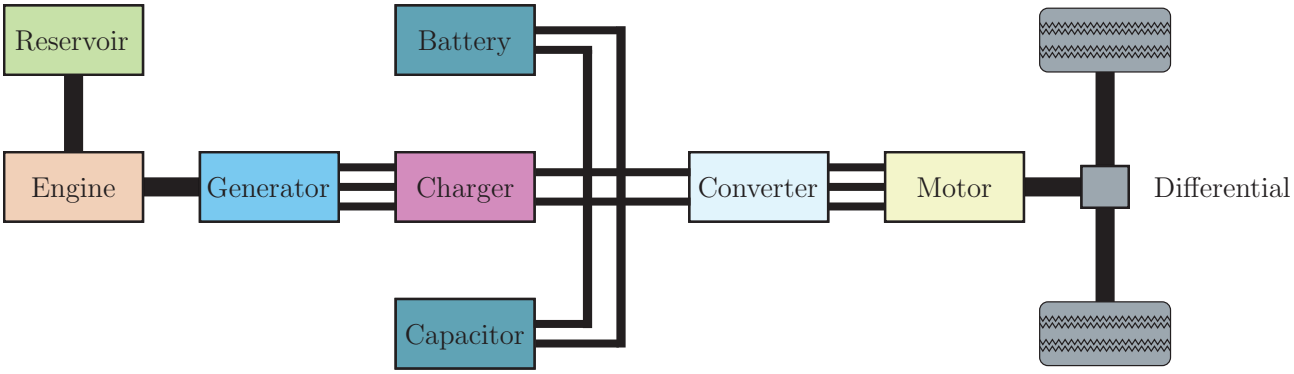

Figure 1.3: Schematic for series hybrid EV [7].

As the small combustion engine can always generate power at its best settings once the batteries are depleted, they become more effective for extended city driving. Examples for series hybrid EVs include Chevrolet Volt, Fisker Karma, etc.

Series-Parallel Hybrid Electric Vehicles: The advantages of combining series and parallel features can be found in series-parallel hybrid EVs. While series hybrids are typically more effective at slower speeds and parallel hybrids are typically more effective at faster speeds, total efficiency is higher as a result. However, there are also challenges, such as the added complexity and cost of having both an ICE and an electric propulsion system. The efficiency of series hybrids can depend on driving conditions and the size of the energy storage system. Advances in technology and ongoing research aim to address these challenges and further improve the performance of series hybrid EVs [6]. The block diagram for series-parallel hybrid EV is shown in Fig. 1.4. Examples of power-split hybrid powertrain includes

the models like Lexus RX-hybrid, Toyota hybrid.

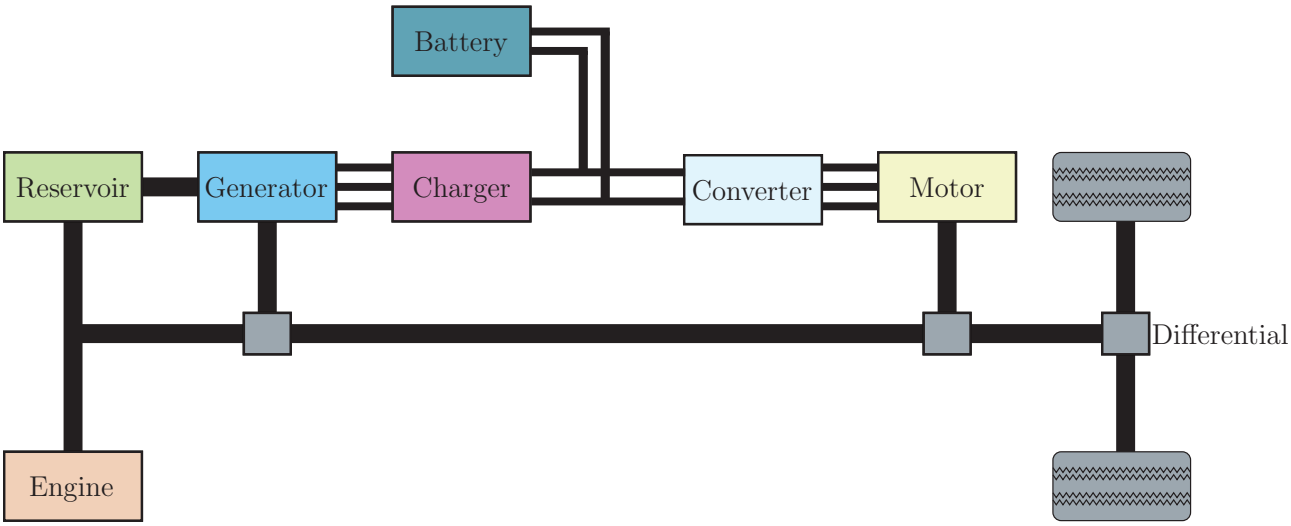

Figure 1.4: Schematic for series-parallel hybrid EV [6].

1.2.2 Plug-in Hybrid Electric Vehicles

An HEV having rechargeable batteries that can be fully charged by plugging into an external electric power source is referred to as a plug-in hybrid EV (PHEV) [4]. A PHEV has elements of both an all-electric car and a standard hybrid EV, including an electric motor and an ICE as well as a connector for connecting to the electrical grid. PHEVs, which use a combustion engine as a backup when the batteries run out, have a far greater all-electric range than traditional gasoline-electric hybrids and also do away with the "range anxiety" that is common with all-EVs. The schematic diagram for PHEV is shown in Fig1.5.

Examples for plug-in hybrid EVs includes Toyota RAV4 Prime, Lexus NX, Ford Escape etc. Based on the size and functions handled by electric system, hybrid EVs are distinguished as shown in table Table 1.1.

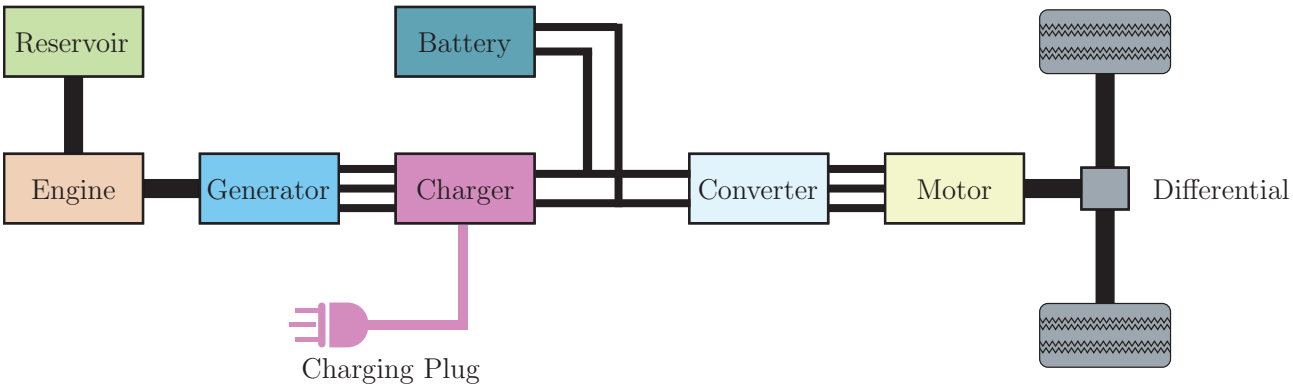

Figure 1.5: Schematic for series plug-in hybrid EV [4].

Table 1.1: HEV classification based on size and function [4].

Parameter/Function	**Micro Hybrid**	**Mild Hybrid**	**Full Hybrid**
Battery Voltage (V)	12	48–160	200–300
Motor Power (kW)	2–3	10–15	30–50
Generator Power (kW)	<3	10–12	30–40
Battery Capacity (kWh)	< 1	< 2	2–10
Fuel Economy (%)	2-4	1–20	> 25
EV Mode Range (km)	0	0	5–10
Idle Stop/Start	Possible	Possible	Possible
Electric Torque Assistance	Not possible	Possible	Possible
Regenerative Braking	Small or no R.B	Mild R.B	Full R.B
Battery Charging during Driving	Possible	Possible	Possible
Battery Charging from Grid	Not Possible	Not Possible	Not Possible

1.2.3 Fuel Cell Electric Vehicles

Fuel cell EV (FCEV), commonly referred to as fuel cell vehicle, is a type of zero-emission vehicle. It is a kind of electric car that makes use of "fuel cell technology" to produce the electricity needed to power the car. The chemical energy is instantly transformed into electric energy in these cars [8]. Fig. 1.6 shows the block diagram of FCEV.

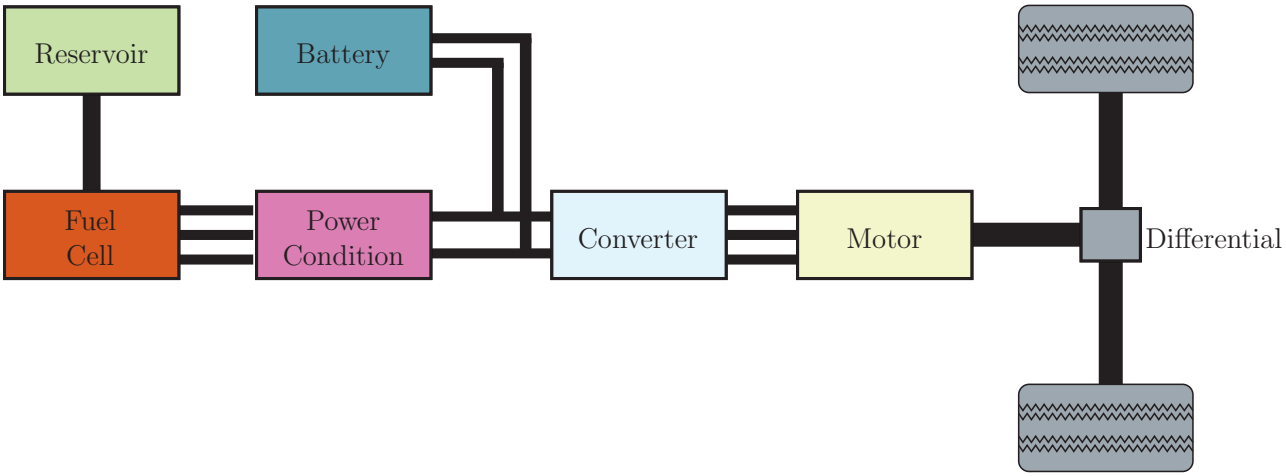

Figure 1.6: Schematic for fuel cell EV [8].

A "fuel cell" electric car operates on a distinct set of principles than a "plug-in" EV. This is so because the FCEV self-generates the electricity needed to power the car. Toyota is developing one such vehicle, the Toyota Mirai. Other examples of fuel cell EVs are Hyundai Nexo, Hyundai Tucson, Honda Clarity Fuel Cell.

1.2.4 Hydrogen Fuel Cell Electric Vehicles

The same kind of electric motor that a battery-electric car uses to turn the wheels also powers hydrogen fuel cell vehicles. But it is powered by a fuel-cell stack instead of a big, heavy battery, in which pure hydrogen travels through a membrane to react with airborne oxygen to create electricity that turns the wheels and water vapor. Schematic for hydrogen fuel cell EVs is shown in Fig. 1.7.

Because of this, fuel-cell vehicles are frequently referred to as fuel-cell hybrid EVs even though they are actually series hybrids. Driving a fuel-cell hybrid EV will essentially be the same as operating a battery-EV, but probably not one of the speedier ones [8]. The vehicle has regenerative braking to recover energy lost as it slows down and no transmission. Example of Hydrogen cars is Hyundai Nexo [7].

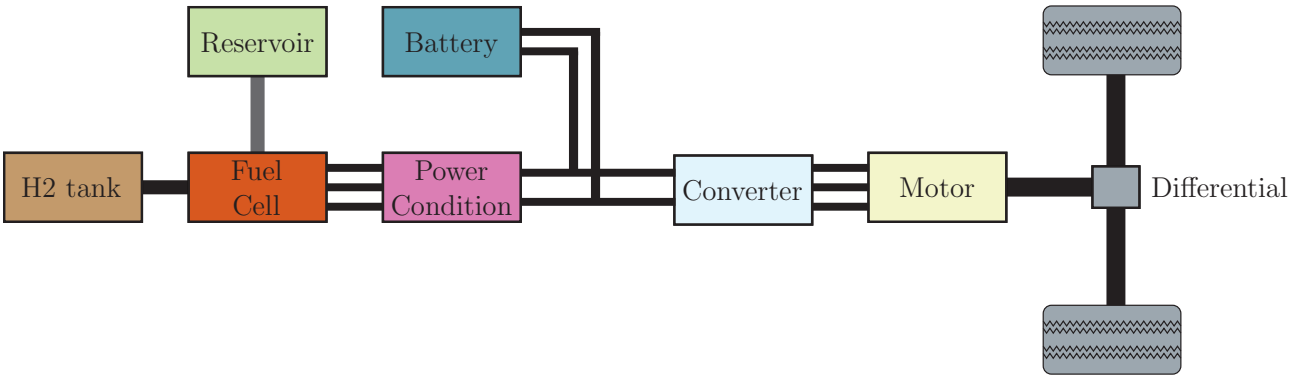

Figure 1.7: Schematic for hydrogen fuel cell EV [7].

1.2.5 Solar Electric Vehicles

A solar car, sometimes known as a solar EV, is an EV that is primarily or entirely powered by solar energy. Solar panels typically feature photovoltaic cells that convert solar energy directly into electric energy. Solar EV block diagram is shown in Fig. 1.8.

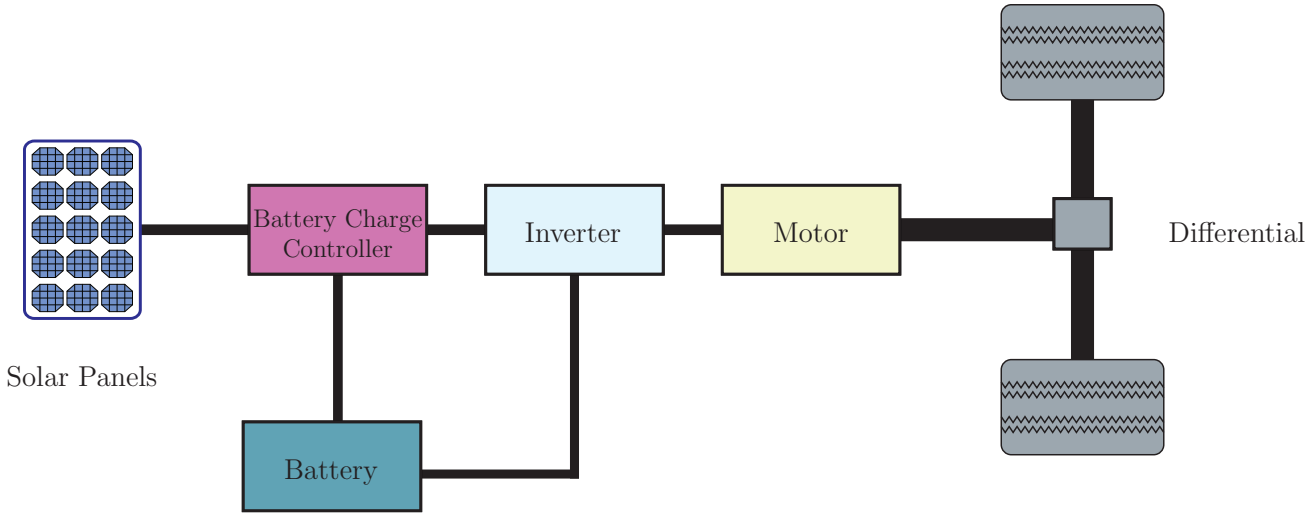

Figure 1.8: Schematic for solar EV [8].

The phrase "solar vehicle" typically implies that all or some of a vehicle's propulsion is powered by solar energy. Communications, controls, and other auxiliary operations might all be powered by solar energy. Nowadays, solar vehicles are marketed more as engineering

experiments and demonstration vehicles, frequently funded by government organizations, than as everyday mobility tools [8]. Yet, there are many vehicles that are indirectly powered by the sun, and solar boats are sold commercially.

1.2.6 Battery Electric Vehicles

Battery EVs, often known as "all-EVs", only use electricity and require an external power source to recharge. The battery of the EV is connected to the power converter to convert the dc voltage supplied by the battery to the three-phase alternating current (AC) voltage to power the permanent magnet synchronous motor (PMSM). The power converter is responsible for the conversion of direct current (DC) to AC to power the motor and adjust the voltage and frequency levels which are suitable to run the motor. Then the power from the motor is transmitted to the wheels of the EV through gear box. Gear box is used in the EVs in order to reduce the speed of the motor and also for torque multiplication. One or more electric motors that are powered by rechargeable battery packs are used to propel them [9]. A majority of new cars entering the market today have an all-electric range of 200 to 300 miles or more, and nearly all BEVs can travel at least 100 miles on a single charge. Schematic of BEV is shown in Fig. 1.9.

Using Level 1 and Level 2 EV chargers at home and Level 3 chargers at public charging stations, drivers may charge their vehicles. Because of advances in battery technology, the range of EVs is increasing. 210 million electric bikes were used daily in the world in 2016. Highway-capable light-duty pure EV sales on a global scale surpassed the million-unit mark in September 2016 [10]. The Tesla Model 3, with an estimated 645,000 sales as of October 2020, is the most popular all-EV ever sold worldwide. The Nissan Leaf is in second place with over 500,000 sales as of September 2020. Examples of BEVs includes Tesla Model 3, Tesla Model S, Tesla Model X, Tesla Roadster, Tata Nexon, Hyundai Kona and Kia Ev6.

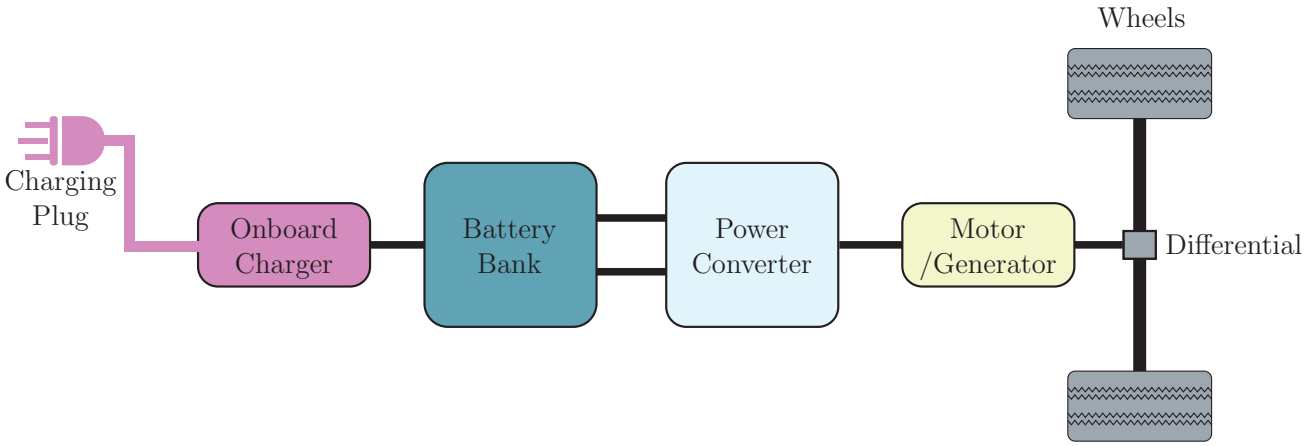

Figure 1.9: Schematic for battery EV [9].

BEVs are most popular used EVs currently due to its advantages like higher efficiency, no harmful emissions, low maintenance cost, etc.

1.3 Overview of Motors in Electric Vehicles

EVs are not new to the world, but with the technological advancements and growing attention to pollution management, they now have the reputation of being the form of transportation of the future. An electric motor serves as the primary component of an EV [11], which takes the place of ICEs. Several types of electric motors can now be employed in EVs thanks to the quickly evolving fields of power electronics and control systems. High starting torque, high power density, good efficiency, etc., are desirable qualities in electric motors used in automotive applications. The most commonly used electric motors in EVs are discussed below.

1.3.1 DC Motors

The DC motor is an excellent choice for traction applications because of its high beginning torque capacity. In the early 1900s, it was the motor that was most frequently employed

for traction applications. DC motor benefits include simple speed control and the ability to tolerate a rapid rise in load [12]. DC motor used in EVs is shown in Fig. 1.10.

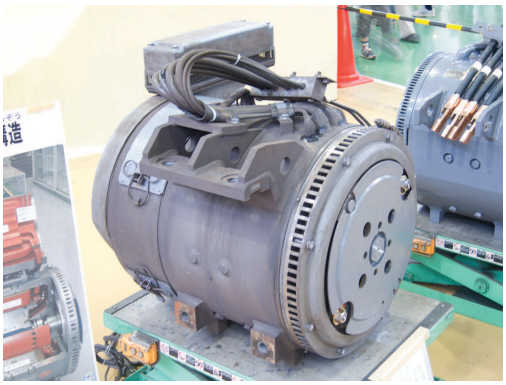

Figure 1.10: DC motor used in EVs (Photo credit : Wikipedia).

It is the optimum traction motor because of all these features. High maintenance required by brushes and commutators is the fundamental disadvantage of DC motors. DC motors are used in small EV applications golf carts, e-scooters, etc.

1.3.2 Brushless DC Motors

It resembles DC motors with permanent magnets in many ways. Because it does not have a commutator and brush setup, it is known as a brushless system. Due to the electronic commutation of this motor, brushless DC (BLDC) motors require no maintenance. The traction properties of BLDC motors include high starting torque, high efficiency of 95–98%, etc. One of the BLDC motor used in EVs is shown in Fig. 1.11.

For high power density design approaches, BLDC motors are appropriate. Due to their traction properties, BLDC motors are the most popular motors for use in EV applications [12]. The BLDC motors are used in one person mobility applications like unicycle, e-scooters, skate boards, gold carts and off-road vehicles.

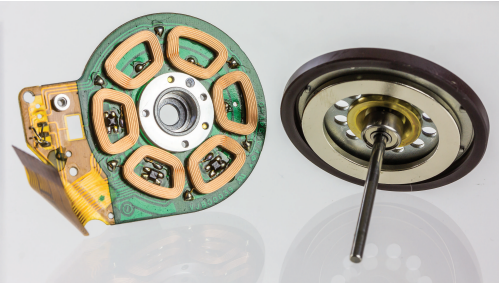

Figure 1.11: Brushless DC motor used in EVs (Photo credit : Wikipedia).

1.3.3 Three-Phase AC Induction Motors

In fixed voltage and fixed frequency operation, induction motors (IMs) do not have a high starting toque like DC series motors. But by utilizing different control techniques like field-oriented control (FOC) or V/f approaches, this characteristic can be changed. These control techniques enable the motor to start with the greatest torque, which is excellent for traction applications. Because they require less upkeep, squirrel cage IMs have a long lifespan. Up to 92–95 % efficiency can be achieved when designing IMs. An IM's disadvantage is that it requires a complicated inverter circuit and is challenging to control. In permanent magnet motors, the flux density B is influenced by the magnets [13]. As a result, IMs make changing the value of B much simpler than permanent magnet motors. That is thus because, depending on the required torque, the voltage and frequency, V/f ratio of IMs can be modified to change the value of B. This contributes to lowering losses, which raises efficiency. Three-phase IM used in Tesla cars is shown in Fig. 1.12.

The best illustration of the IMs' superior performance compared to competitors is the Tesla Model S. IMs are also used in automobiles and buses made by major automakers like TATA Motors [14]. Due to their low cost, IMs are the favored option for EVs that focus on performance. The ability to tolerate harsh weather conditions is another benefit.

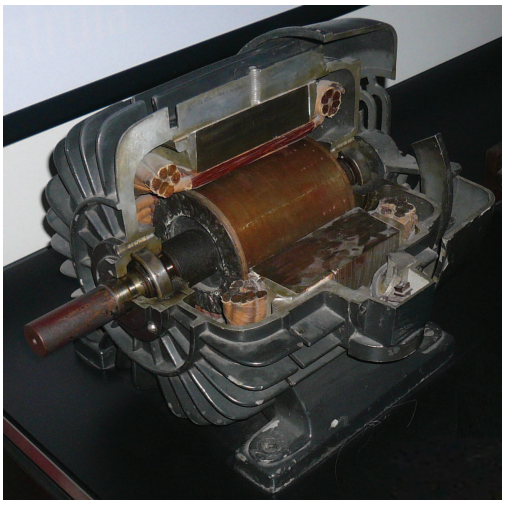

Figure 1.12: 3-phase ac induction motor used in tesla (Photo credit : Wikipedia).

1.3.4 Switched Reluctance Motors

Variable reluctance motors with two-fold saliency fall within the category of switched reluctance motors. Switched reluctance motors (SRMs) are dependable and have a straightforward design. The SRM's rotor is a piece of laminated steel that has neither permanent magnets nor windings attached to it. As a result, the rotor's inertia is reduced, aiding in rapid acceleration. Switched reluctance motor is shown in Fig. 1.13

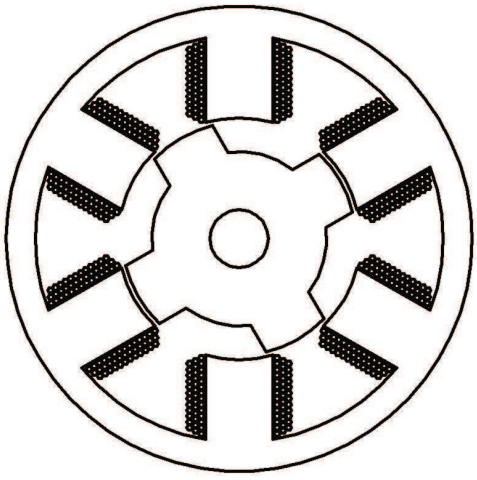

Figure 1.13: Switched reluctance motor used in EVs (Photo credit : Wikipedia).

SRM is a viable choice for the high-speed application due to its robustness. High power density is another feature that SRM delivers that is essential for EVs. It is simpler to cool the motor because the stator generates most of the heat [15]. The SRM's control complexity and expanding switching circuit are its two greatest flaws. It has some noise problems as well.

1.3.5 Permanent Magnet Synchronous Motors

PMSMs are most popularly used in EVs. This motor and the BLDC motor, which has permanent magnets on the rotor, are comparable. PMSMs share traction features like BLDC motors, such as high-power density and good efficiency. The back EMF in PMSM is sinusoidal, whereas the back EMF in BLDC is trapezoidal. Higher power ratings are possible with synchronous motors. For high performance applications like vehicles and buses, PMSM is the ideal option. Despite being more expensive, PMSM is giving IMs a tough fight because of its higher efficiency [15]. In addition, PMSM costs more than BLDC motors. PMSM motors are used by the majority of manufacturers in their HEVs and BEVs. For instance, the Nissan Leaf, Honda, Zero Motorcycles S/SR, Chevrolet Bolt EV, Ford Focus Electric, and Toyota Prius use PMSM motors for propulsion. PMSM offers advantages like high performance efficiency, smooth torque, no torque ripples etc. PMSMs are further classified into two types as shown in Fig. 1.14. The modern EVs and their key parameters are shown in Table 1.2.

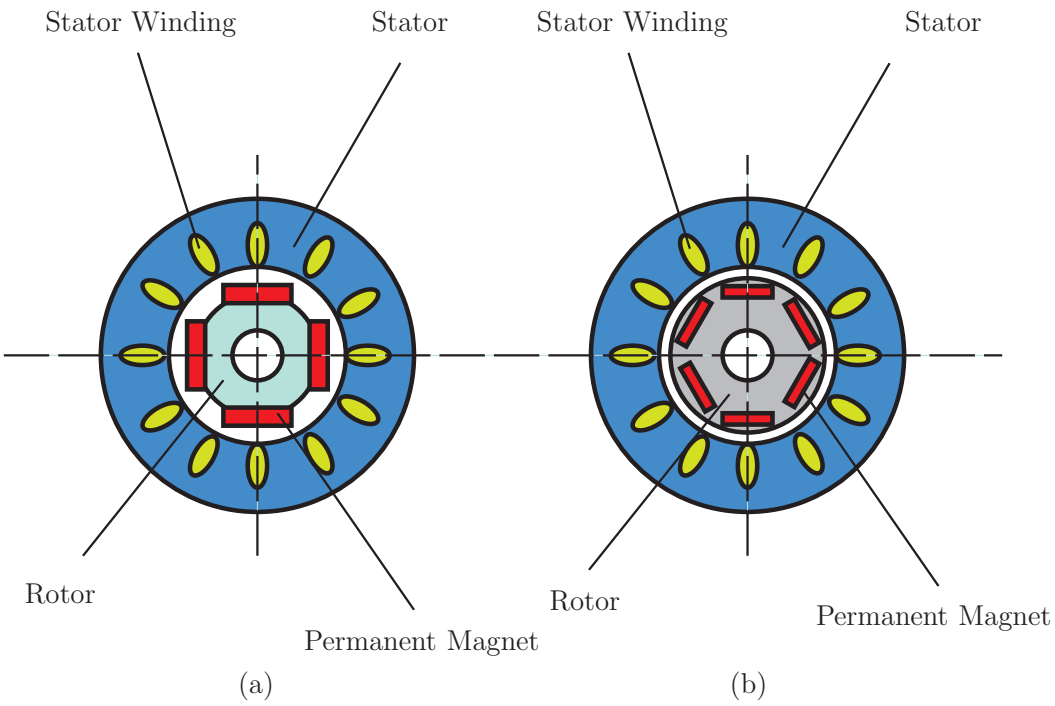

Figure 1.14: Classification of PMSM motors : (a) surface-mounted PM motor and (b) interior PM motor.

- **Surface-Mount Permanent Magnet Motors (SPMSMs):** The magnets on this motor are mounted to the rotor's outer surface. Their mechanical strength is lower than due to this construction type. The motor's maximum safe mechanical speed is constrained by the decreased mechanical strength [15]. These motors also have extremely low magnetic saliency ($L_{ds} = L_{qs}$). Regardless of the rotor position, inductance levels measured at the rotor terminals remain constant. Due to the saliency ratio being so close to 1, SPMSM motor designs heavily, if not entirely, rely on the magnetic torque component to generate torque.

- **Interior Permanent Magnet Synchronous Motors (IPMSMs):** these motors have the permanent magnet imbedded into the rotor itself. Unlike their SPMSM counterparts, the location of the permanent magnets makes IPMSMs mechanically sound, and suitable for operating at very high speeds [15]. These motors also are defined by their relatively

Table 1.2: Key parameters of modern EVs.

EV Model	Motor Type	No. of Motors	Motor HP	Battery Capacity (kwh)	EPA (miles)	Power (kW)
Tesla Model SP85D	IM	2	691	85	253	345
Tesla Model S Plaid	PMSM	3	1020	120	341	820
Tesla Model 3 Performance	PMSM	2	513	82	352	377
Tesla Model Y Standard Range	PMSM	2	351	50	230	258
Tesla Cybertruck	PMSM	4	800	123	500	596
Lucid Air Touring	PMSM	2	800	110	517	600
Audi e-tron	PMSM	2	402	95	303	300
Audi e-tron Sportback	IM	2	402	95	218	300
Audi e-tron GT	PMSM	2	470	93.4	303	350
Hyundai Kona	PMSM	1	201	64	258	150
Hyundai Ioniq 5	PMSM	1	320	77.4	287	226
Ford Mustang Mach	PMSM	1	290	98.9	300	216
Volvo XC40 Recharge	PMSM	2	408	78	200	300
BMW i3S	PMSM	1	181	42.2	153	135
BMW i4	PMSM	2	335	83.9	483	250
Volkswagen ID.3	PMSM	1	148	45	218	150
Chevrolet Bolt	PMSM	1	200	66	259	149
Nissan Leaf	PMSM	1	215	62	226	160
Mini Cooper	PMSM	1	181	32.6	114	135
Porsche Taycan Turbo S Cross	PMSM	2	750	93.4	202	559
Kia Niro	PMSM	2	201	64	239	150
Kia EV6 Long Range	PMSM	2	320	77.4	304	238

high magnetic saliency ratio ($L_{qs} > L_{ds}$). Due to their magnetic saliency, an IPMSMs have the ability to generate torque by taking advantage of both the magnetic and reluctance torque components of the motor. This is the reason; IPMSMs are widely used in the various applications and also more suitable for EV applications. Benefits of these motors include structural integrity, reducing back EMF, generate torque for both magnetic and reluctance components, high saliency ratio etc.

1.4 Overview of Power Converters in Electric Vehicles

Power electronic circuits have been increasingly evolving over the past ten years as the focus of automotive technology has shifted to the replacement of mechanical, hydraulic, or pneumatic systems with electrical systems. The demand for small and effective power electronic circuits has increased as a result of rising vehicular loads such as utility, entertainment, luxury, and safety loads. The voltage needs of the electric parts within the car vary, but most of them operate at lower levels. The radio, dashboard gauges, air conditioning, and built-in computers and displays are all examples of this [16]. The main components of an EV are AC-DC converter for charging, DC-AC inverter for controlling motor speed and torque, a DC-DC converter for battery pack voltage boosting and charging, a battery, and an electric motor.

- **DC-DC converter (Chopper):** DC-DC converters used in EVs can be divided into unidirectional and bidirectional converters. Diverse onboard loads like sensors, controls, entertainment, utility, and safety devices are accommodated by unidirectional DC-DC converters. They are also utilized in electric traction and DC motor drives. Bidirectional DC-DC converters are used in situations when backup power, regenerative braking, and battery charging are necessary.

- **AC-DC Converter (Rectifier):** The converter is an internal component of electric cars. Despite being a converter, it is referred to as the "onboard charger". It transforms power from AC to DC before supplying it to the vehicle's battery. The majority of EV chargers today use AC power, making this the most popular charging mode. The combination of rectifier and chopper configuration for EVs is shown in Fig. 1.15.

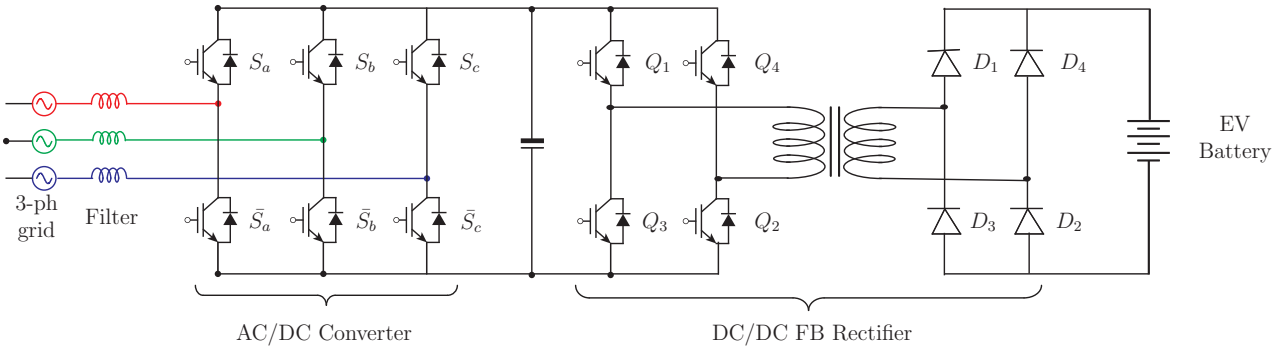

Figure 1.15: Configuration of EV using rectifier and chopper.

- **DC-AC Converter (Inverter):** An essential part of an EV is an inverter, which transforms the DC from the battery into the AC needed to power the electric motor. The direction of the flow of electricity is continually and routinely switched through an electronic switch (often a group of semiconductor transistors). The DC-AC converter acts as rectifier during regenerative braking converting AC output of generator to DC to charge the battery.

1.4.1 Inverter Topologies

An EV motor uses an inverter to convert DC electricity to the AC power it needs to run. By altering the alternating current's frequency, the converter can modify the motor's rotational speed. By changing the voltage amplitude, the motor's torque can be increased or decreased. The inverter topologies are broadly classified into two types in general. They are current source inverters and voltage source inverters. The voltage source inverters are

most popularly used in EVs and they are further classified into following categories:

- **2-Level Voltage Source Inverter (2L-VSI):** A 2L-inverter produces two distinct voltages for the load; for example, if we supply V_{dc} as an input, it will produce V_{dc} and 0 on the output. These two newly created voltages are typically switched in order to create an AC voltage.

  This way of producing AC is efficient, but it does have some drawbacks, such as harmonic distortions in the output voltage and a higher dv/dt than a multilevel inverter. I have considered this converter in this thesis as it is easy to understand, and it is widely used in the EVs. The schematic for 2L-VSI is shown in Fig. 1.16.

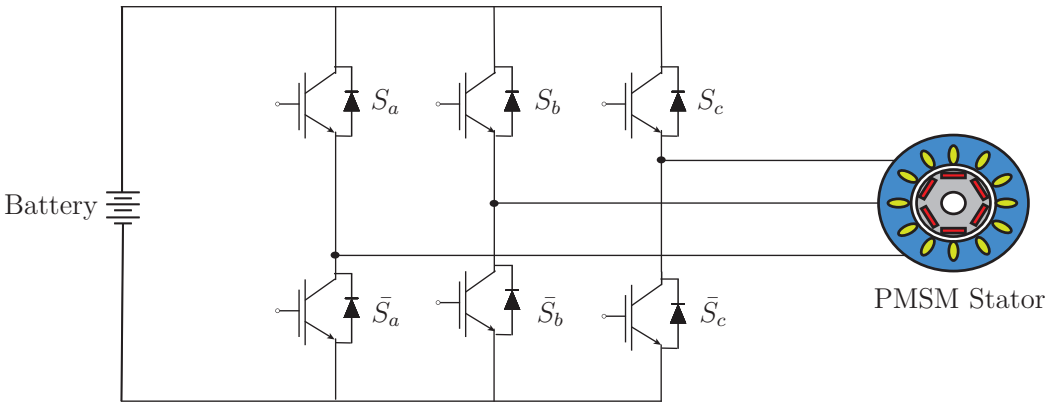

Figure 1.16: 2-level voltage source inverter.

- **Multilevel Inverters:** In multilevel inverter, more than two voltage levels are produced to make the output waveform that is smoother and has fewer harmonic distortions and dv/dt. This is done in order to avoid dealing with the 2L voltage output. Waveform smoothness is correlated with voltage levels; as voltage levels rise, the waveform becomes smoother, but the intricacy of the controller circuit and its components also rises. The waveform becomes smoother as the number of levels increase in multilevel inverter. These inverters are further classified into various categories as shown in Fig. 1.17 [17]:

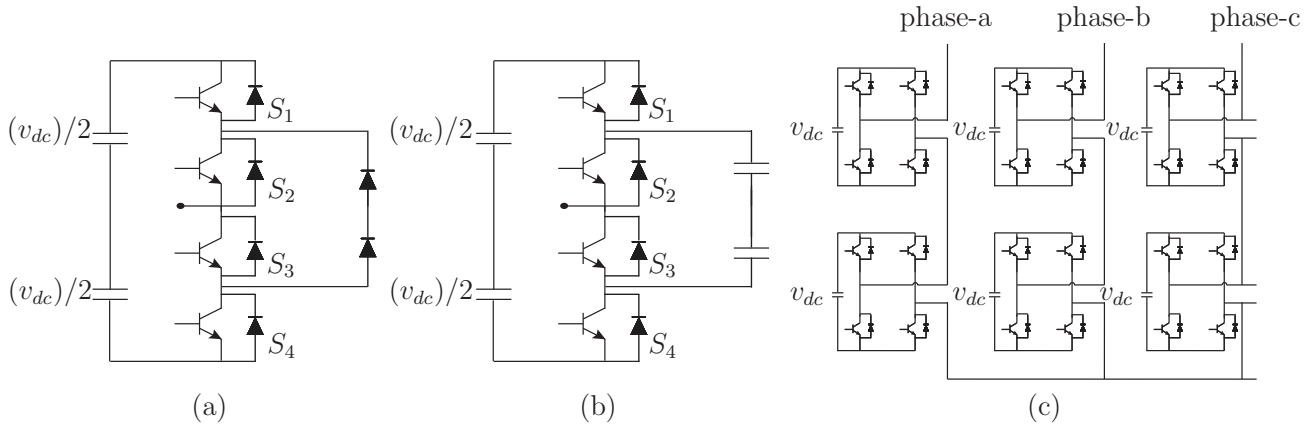

Figure 1.17: Multilevel inverters : (a) 3-level NPC inverter, (b) 3-level flying capacitor inverter, and (c) 5-level cascaded H-bridge inverter.

– **Neutral Point Clamped (NPC) Converters:** The use of clamping diodes to ensure appropriate voltage sharing across the power switches distinguishes NPC inverters from other multilevel power converter families. They continue to be the most popular and well-known multilevel converter topology in use today because they provide very attractive efficiency with minimal complexity. NPC (Fig. 1.17(a)) inverters provide better waveform clarity, reducing the need for filtering. Their superior blocking voltage capability is also a crucial prerequisite in medium voltage applications, where they are frequently used. However, due to the complicated mechanical configuration of the power devices with a greater number of levels, the industrial use of NPC-type inverters is generally restricted to three-level topologies [18].

– **Flying Capacitor Converter:** MLIs, which are frequently found in applications like EV inverters, battery management systems, renewable energy systems, and other power electronics, use flying capacitor converter (Fig. 1.17(b)) as an alternative to the NPC inverter [18]. Using several capacitors connected in series and parallel to create the desired voltage level, a flying capacitor's primary job is to store and transfer energy between source and load.

– **Cascaded H-Bridge Converter:** An electronic circuit known as an H-bridge changes the polarity of a voltage given to a load. The H-bridge (Fig. 1.17(c)) is frequently used in inverters. The system is occasionally referred to as a single-phase bridge converter. A square wave voltage waveform will be produced across the load by the H-bridge when powered by a DC source. The apex of the current waveform for an entirely inductive load would depend on the inductance, switching frequency, and input voltage [18].

1.4.2 Semiconductor Devices Used in the EV Inverters

Many EVs use insulated gate bipolar transistors (IGBTs) or metal-oxide-semiconductor field-effect transistors (MOSFET) in their inverters. The specific choice of semiconductor devices can vary between manufacturers and even between different models from the same manufacturer. The type of power semiconductor device used in inverters can impact the overall performance, efficiency, and cost of an EV [19].

Engineers have come to understand over time that inverters are essential to EV performance and driving range. Here, more energy might be extracted from the battery more efficiently by power-efficient components, extending the cruise range and requiring less space for the on-board battery. Silicon carbide (SiC) MOSFETs are now the preferred technology for EV traction inverters [20]. Subsequently, when EVs transitioned from 400-V to 800-V battery systems, automotive engineers started searching for parts that could effectively withstand greater working voltages and temperatures, even though EV driving range and battery size and weight have always been important factors [21].

IGBTs and MOSFETs are both commonly used in power electronics applications like inverters. IGBTs are often preferred for high-power applications due to their combination of the high input impedance of a MOSFET and the voltage and current-carrying capabilities of a bipolar transistor. MOSFETs, on the other hand, are known for their fast-switching

speeds and low conduction losses.

1.4.3 Inverters Used in the EV Market

- **Tesla:** Tesla produces its own drive inverter for the Model S/X at its Fremont factory, but the automobile company mainly uses TO-247 transistor packages, which are well-established commercial products. When developing the Roadster, the business adopted this strategy from the beginning. Tesla inverter is shown in Fig. 1.18.

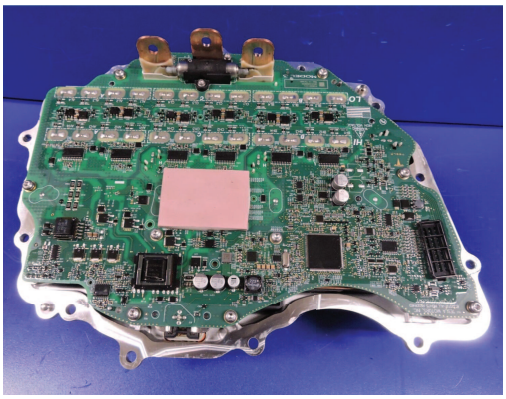

Figure 1.18: Tesla inverter (Photo credit : Wikipedia).

Tesla vehicles utilize SiC inverters, an innovative headway over conventional silicon-based inverters. SiC inverters offer improved effectiveness, flaunting up to a 20% improvement contrasted with their silicon partners. This elevated productivity converts into expanded range for Tesla vehicles, upgrading battery execution. Additionally, SiC inverters are strikingly more modest and lighter, up to half more reduced than customary inverters, adding to further developed weight conveyance and generally speaking vehicle productivity. The more powerful thickness of SiC inverters permits Tesla vehicles to keep up with execution with more modest and lighter parts. Explicit SiC inverters utilized in Tesla models incorporate a 24 SiC MOSFET module inverter for Model 3 and Model Y, and a 48 SiC MOSFET module inverter for Model S and Model X. This mechanical decision highlights

Tesla's obligation to delivering productive and strong EVs, situating them among the forerunners in the EV market. Tesla's continuous devotion to inverter advancement, especially in the domain of SiC innovation, is demonstrative of the organization's quest for constant improvement in its future vehicle plans.

- **Nissan:** Electric car inverters regulate the electricity coming from the power source, and their size frequently places restrictions on the design of the vehicle. The newly created inverter utilizes a new hetero junction diode structure from Nissan and uses SiC for the diodes, a semiconductor device used to regulate the flow of current in a single direction. Nissan inverter is shown in Fig. 1.19.

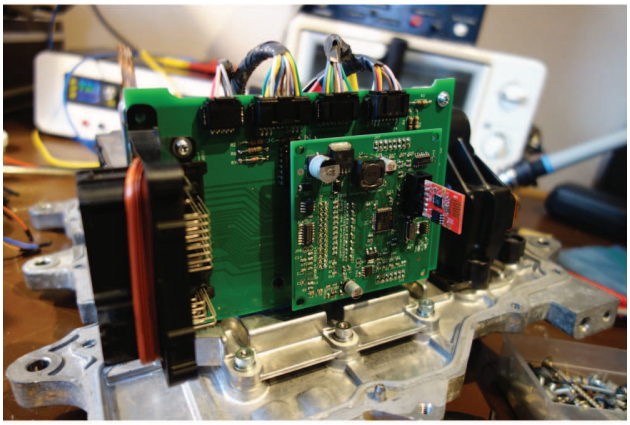

Figure 1.19: Inverter used in Nissan EVs (Photo credit : Wikipedia).

The inverter's total size and weight are decreased, and its reliability is significantly increased when the SiC diode and hetero junction diode structure are used together [22]. Earlier silicon diodes needed heat dissipation mitigation techniques and resulted in power losses when used in EVs. A high breakdown voltage, large capacity inverter is made possible by a newly developed SiC diode*2 that offers high power efficiency, better heat resistance, and increased dependability. In contrast to earlier diodes, the new SiC inverter's diode surface has been reduced by 70 %, and the circuit's energy efficiency has

increased by 20 %. Further size and weight reductions of the inverter of 15 % to 20 % are possible due to the simplification of the cooling systems in the system. Nissan is presently developing EVs and HEVs, but the new SiC diode technology is not just applicable to fuel cell vehicles. Along with the motor and the battery, the inverter is one of the important technologies in the development of EVs according to Nissan. By using SiC diodes on the transistor, the firm hopes to further reduce the size of the inverter.

- **Hyundai and Kia:** For its 800-volt parts, Vitesco Technologies has gotten a significant order. Hyundai is receiving 800-volt inverters with SiC technology from Continental's drive division for the first time in sizable amounts. Inverter used in Hyundai and Kia motors is shown in Fig. 1.20.

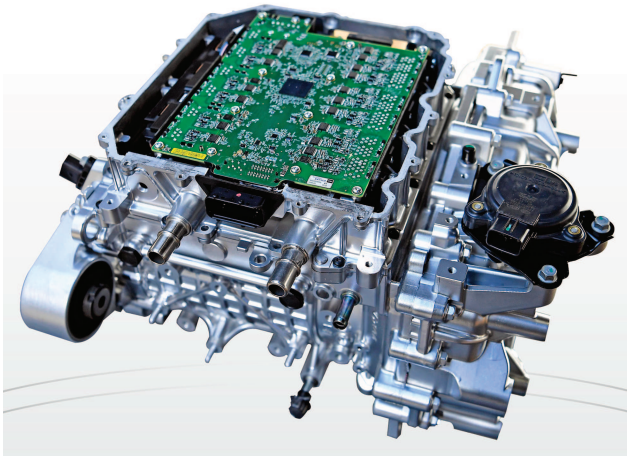

Figure 1.20: Hyundai and Kia power inverter (Photo credit : Wikipedia).

The largest purchase from the Korean business, according to Vitesco, has a three-digit million-euro sales volume. With the E-GMP, Hyundai and Kia hope to make 800-volt technology more widely available. The Hyundai Ioniq 5 and the Kia EV6 are the first cars to be unveiled. Prices for the Kia variant is still unavailable. The starting price for the Ioniq 5 is 41,900 euros before discounts.

- **Volkswagen:** Delphi Technologies announced that it will be the first significant auto industry supplier to make an 800-volt inverter. Delphi emphasizes that this component is one of the enablers to allow 800-volt charging and effectively cut charging times in half compared to today's 400-volt systems. According to Delphi, automakers have more flexibility with 800-volt systems because they can choose to use smaller, lighter cables and connectors, generate more power through regenerative braking, or choose ultra-fast charging. And it has at least one more manufacturer on board. Volkswagen inverter is shown in Fig. 1.21.

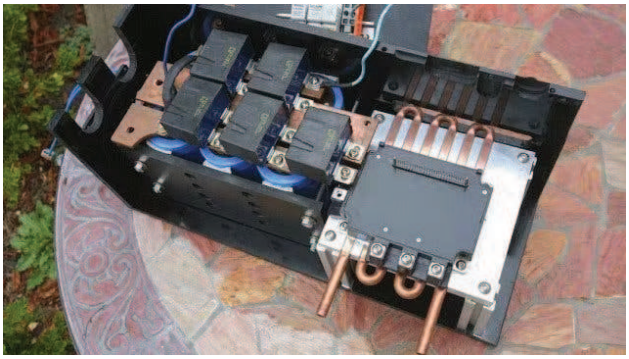

Figure 1.21: Inverter in Volkswagen EVs (Photo credit : Wikipedia).

According to Delphi, it has a $ 2.7 billion contract with "a premier global OEM" for the 800-volt inverter's volume manufacturing over an eight-year period, with the product launch of "a high-performance vehicle" scheduled for 2022. A lengthy list of possible products appears as a result. It is predicted that the premium electric platform used by the Volkswagen Group will be used in some or all of the upcoming Porsche and Audi vehicles, as well as the Genesis electric luxury cars from Hyundai. The BEV3 architecture from General Motors is anticipated to debut in a Cadillac, along with high-end EVs from Mercedes-Benz.

1.5 Overview of Batteries in Electric Vehicles

A BEV or HEVs electric motors are powered by a rechargeable battery known as an EV battery (often referred to as a traction battery). The starting, lighting, and ignition batteries used in EVs are typically lithium-ion batteries with high power-to-weight ratios, specific energies, and energy densities. Smaller, lighter batteries are preferred because they lighten the load on the vehicle and enhance its performance. The majority of today's battery technologies have substantially lower specific energies than liquid fuels, which frequently reduces the maximum range of all-electric cars. Lithium-ion and lithium polymer batteries are the most prevalent battery types in contemporary EVs. Lead-acid ("flooded", "deep-cycle", and "valve-regulated lead acid"), nickel-cadmium, nickel-metal hydride, and, less frequently, zinc-air and sodium nickel chloride (zebra) batteries are other types of rechargeable batteries used in EVs. Batteries electrical capacity, or "electric charge," is measured in ampere hours or coulombs, with the total energy being expressed in kilowatt-hours (kWh) [23].

Lithium-ion (Li-ion) battery technology has advanced since the late 1990s as a result of demands from portable devices, laptop computers, mobile phones, and power tools. These improvements in performance and energy density have benefited the BEV and HEV market. Lithium-ion batteries, in contrast to prior battery chemistries like nickel-cadmium, allow for daily discharge and recharge at any level of charge. A BEV or HEV's battery pack accounts for a sizeable portion of the cost. Since 2010, the price of EV batteries has decreased 87 % per kilowatt-hour as of December 2019. As of 2018, vehicles like the Tesla Model S that have an all-electric range of more than 250 miles (400 km) are commercially available in a wide range of vehicle segments. Because BEVs are more energy efficient, their running costs are lower than those of comparable ICE vehicles because they use less power. The most common type of batteries used in EVs are described below.

1.5.1 Lead-Acid Batteries

Lead-acid batteries have a low specific energy (30-50 Wh/kg) despite their low cost (100-150 dollars/kWh), making them unsuitable for the majority of electric road transport vehicles (such as forklifts) (even HEVs) [23]. Lead-acid batteries used in EVs is shown in Fig. 1.22.

Figure 1.22: Lead-acid batteries (Photo credit : Wikipedia).

It also only lasts a brief time (3–5 years). Lead-acid battery producers may be able to significantly enter the micro-hybrid automotive industry with intermediate storage batteries that are smaller than rival battery technologies or with contemporary, compact, and lighter capacitor banks/supercapacitors. The medium-term development of micro-hybridization for small cars is in jeopardy (5-10 years).

1.5.2 Nickel-Metal Hybrid Batteries

Nickel-Metal Hybrid Batteries (NiMHs) are generally utilized in HEVs with limited storage capacity because their specific energy (100 Wh/kg) does not match the standards for fully EVs. PHEVs have an onboard NiMH storage capacity of 30 kilometers [23]. It is problematic because these batteries' anode and cathode both contain nickel and rare earths.

The high nickel content limits potential for further cost reduction and, thus, application in future EVs. nickel costs are also projected to be rising. NiMH batteries are used in Toyota Prius and is shown in Fig. 1.23.

Figure 1.23: Nickel-metal hybrid batteries (Photo credit : Wikipedia).

1.5.3 Sodium Nickel Chloride Batteries

ZEBRA (Zero Emission Battery Research Activities) batteries, or sodium nickel chloride batteries, are a novel and exciting development in high-temperature rechargeable battery technology. The solid beta-alumina electrolyte used in these batteries enables the passage of sodium ions between the negative sodium electrode and the positive nickel chloride electrode. ZEBRA battery is shown in Fig. 1.24.

The high working temperature of sodium nickel chloride batteries—typically between 270 and 350 degrees Celsius—is one of its distinguishing characteristics. This higher temperature encourages a longer cycle life and increases efficiency. Because of its reputation for stability, safety, and dependability, batteries made of sodium nickel chloride are a good fit for some uses, such electric cars and stationary energy storage.

Figure 1.24: Sodium nickel chloride batteries (Photo credit : Wikipedia).

1.5.4 Solid State Batteries

Solid-state batteries, which use solid electrolytes rather than liquid components, provide a potential development in energy storage technology. Solid-state batteries provide a number of benefits over conventional lithium-ion batteries, including increased safety since they are less prone to leaks and overheating. These batteries also provide the possibility of higher energy density, which might result in power sources that are more effective and long-lasting. Solid-state batteries are lighter and more compact due to the lack of liquid electrolytes, which makes them especially desirable for uses like electric cars where weight and size are important factors. For the future of portable devices, electric cars, and renewable energy storage, solid-state batteries show considerable potential, even if research and development in this sector must still solve issues like manufacturing complexity and cost. Solid state batteries look like as shown in Fig. 1.25.

In terms of power storage, solid state batteries are the holy grail. Indeed, it has been under development for close to ten years. There hasn't been a significant advancement in performance that is commercially viable yet [23].

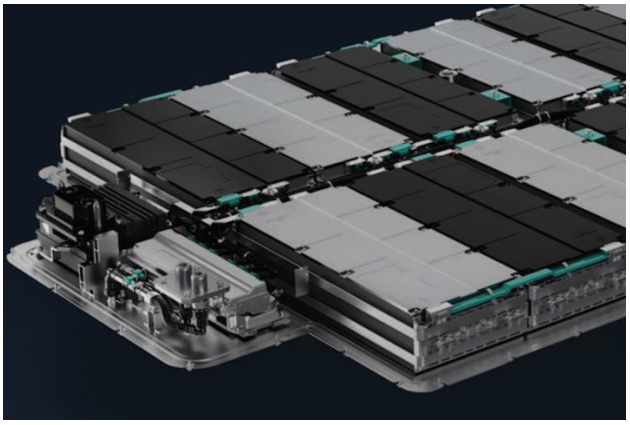

Figure 1.25: Solid state batteries (Photo credit : Wikipedia).

1.5.5 Lithium-Ion Batteries

The majority of new EVs worldwide use these batteries. Currently, Li-ion battery packs which frequently contain heat control devices are used by all EVs with ranges greater than 150 km [23]. Li-ion batteries used in EVs is shown in Fig. 1.26.

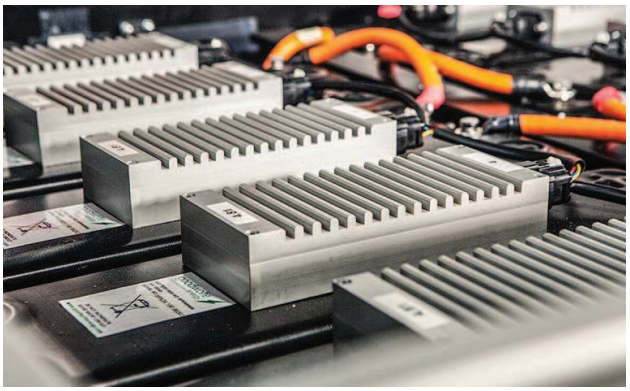

Figure 1.26: Lithium-ion batteries (Photo credit : Wikipedia).

The high specific energy of this technology is now an advantage. Although Li-ion batteries for electric cars have specifications of 160 Wh/kg and 450 Wh/l, the expense of these batteries (700–1000 dollars/kWh) is still a drawback. Li-ion batteries used in Tesla cars is shown in Fig. 1.27. The primary goals are to increase performance and reduce expenses while protecting the environment.

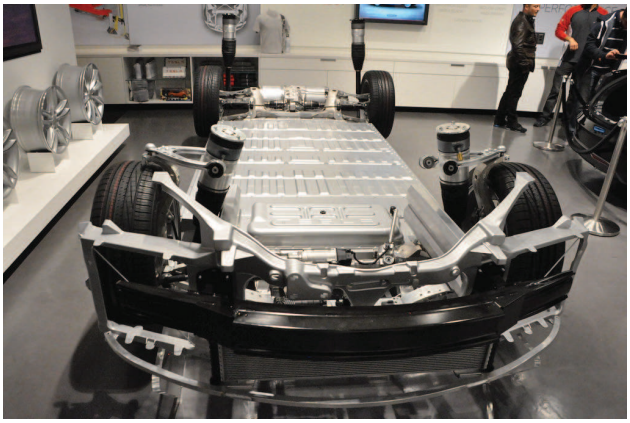

Figure 1.27: Lithium-ion batteries used in Tesla (Photo credit : Wikipedia).

1.6 Overview of Digital Control Methods

The overall control of PMSM for EV application is shown in Fig. 1.28. The battery voltage from EV is given to 2L-VSI to produce three-phase voltages with variable amplitude and frequency to the PMSM. Motor currents and speed are measured and given as a feedback to the digital controller. The vehicle control system converts the drive cycle into reference speed. The digital controller adjust the speed to its reference speed by turning the switching signals to the inverter.

We have different type of control methods used to control the motor based on application. Accurate control methods are required to control the PMSM speed and torque in order to fulfill the overall control objectives of an EV. The electric powertrain components of EVs are managed and optimized using a range of control strategies. In order to achieve optimum performance, maximize vehicle range, and ensure efficient energy consumption, certain control techniques are essential. The following are some essential control methods seen in EVs.

- **Field-Oriented Control (FOC)**: Also referred to as vector control, used in EVs to maximize the performance of electric motors is called field-oriented control, or FOC. In

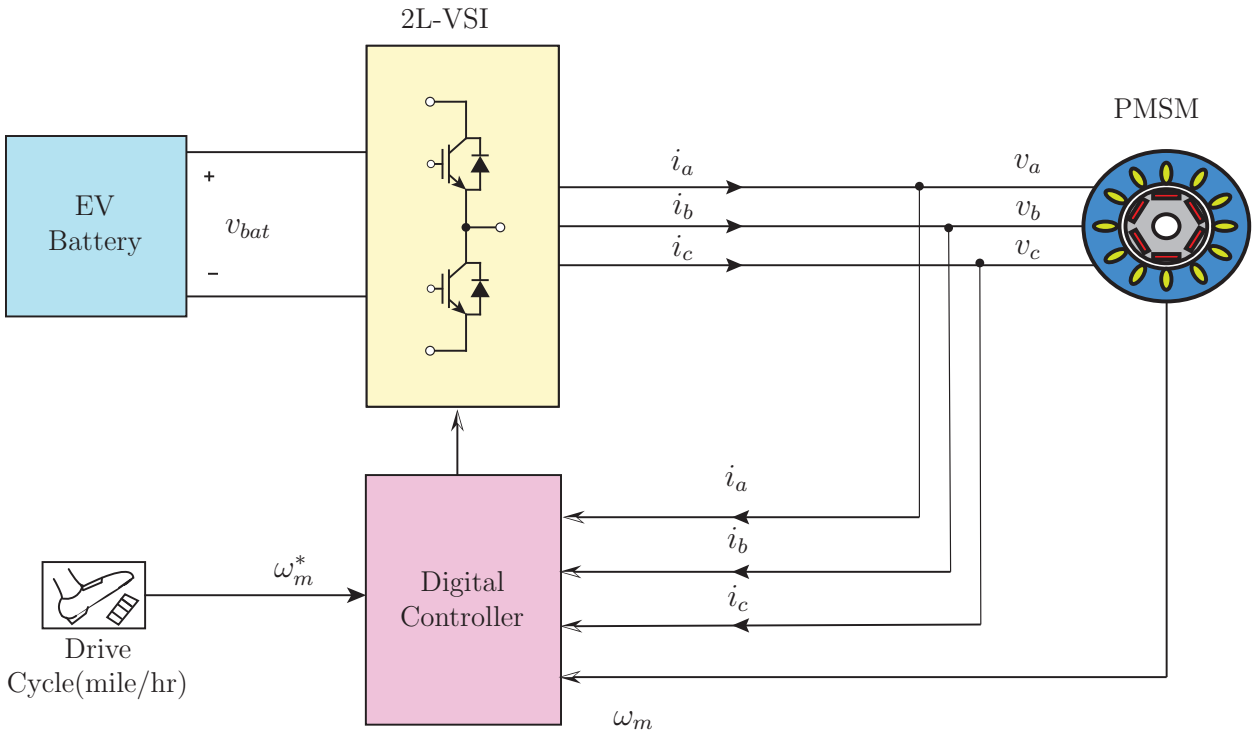

Figure 1.28: Layout of EV control system.

order for FOC to function, the motor is split into two orthogonal parts: the d-axis, which controls magnetic flux, and the q-axis, which controls torque. Exact control over the torque and speed of the motor is ensured by FOC, which lines up the d-axis with the rotor flux [24]. By improving efficiency, this strategy enables dynamic and seamless functioning under a range of driving circumstances. FOC is a commonly used technique in EV propulsion systems because of its ability to separately control torque and flux, which improves overall performance [25].

- **Direct Torque Control (DTC)**: this is a sophisticated control strategy implemented in EVs to enhance the precision and efficiency of electric motor operation. DTC controls the torque and flux of the motor directly, eliminating the need for intricate coordinate conversions, in contrast to standard control techniques. With this method, the torque of the motor can be quickly and precisely adjusted, giving the driver rapid and dynamic

control over the acceleration and deceleration of the car [26]. By reducing torque and flux ripple, DTC enhances energy efficiency and produces smoother operation. Direct torque control, which can react quickly to shifting load situations, is becoming a crucial component of contemporary electric propulsion systems, advancing the general development and dependability of EVs.

- **Pulse Width Modulation (PWM) and Space Vector Modulation (SVM)**: In the world of EVs, PWM and SVM are essential methods, especially for power electronic converter management [27]. PWM controls the average power supplied to a load, such an electric motor in an EV, by altering the width of the pulses in a square wave signal. Because of its ease of use and effectiveness in controlling motor speed and torque, this modulation approach is extensively employed. SVM, on the other hand, is a more sophisticated modulation method that produces a smoother output waveform by efficiently distributing the voltage vectors in a three-phase system. By lowering torque and flux ripples in the motor and minimizing harmonic distortion, SVM improves performance and efficiency. In EV motor drive systems, PWM and SVM are essential components that impact factors like energy economy, motor control accuracy, and overall system dependability [28]. The development and widespread use of electric cars are made possible by these modulation techniques, which are crucial to the progress of electric propulsion technology.

- **Model Predictive Control (MPC)**: An essential component in improving the efficiency and performance of EVs is MPC. Because EV systems are dynamic and linked, a comprehensive approach to vehicle control is made possible by this advanced control method. The use of MPC in electric cars is anticipated to have a major impact on the continuous development of intelligent and effective mobility solutions [29]. This method uses an inverter system prediction model to forecast future behavior and adjust the control inputs

appropriately. MPC is concerned with controlling the current that is provided to the electric motor in the context of EV inverters. MPC minimizes mistakes in the present and reacts fast to variations in the load or operating circumstances by taking into account the dynamic behavior of the system and forecasting future states. Because of its predictive nature, EVs' electric power conversion process can be precisely controlled, which lowers harmonic distortions and boosts overall efficiency.

- **Modulated Model Predictive Control ($\mathbf{M^2PCC}$)**: this method represents an advanced and innovative approach to optimizing the performance of EVs. This strategy integrates the principles of MPC with modulation techniques to achieve more refined control over key parameters. This approach enables the optimization of control inputs, such as motor torque and power distribution, through the incorporation of modulation strategies like PWM or SVM. This method guarantees effective energy conversion and enhanced motor drive performance by allowing the EV inverter to dynamically modify the modulation pattern in real-time. Because of its versatility and predictive power,M^2PCC is essential to optimizing the effectiveness of electric power supply in EVs, which improves overall system performance and extends driving range [30].

1.6.1 Linear Control

Linear control method with proportional-integral (PI) regulator and modulation stage is shown in Fig. 1.29. The drive cycle produces reference speed ω_m^*. The measured motor speed ω_m is compared with the reference speed ω_m^* and the error is given to the PI controller. The PI controller produces reference currents $\mathbf{i}^*(k)$ for the motor. The measured motor currents $\mathbf{i}(k)$ are compared with the reference currents $\mathbf{i}^*(k)$, and the current error $\Delta\mathbf{i}(k)$ is sent as an input to the PI controller. The PI controller then processes the current error and produces reference voltage (also called modulating waveform) $\mathbf{v}^*(k)$ for use with the modulation stage.

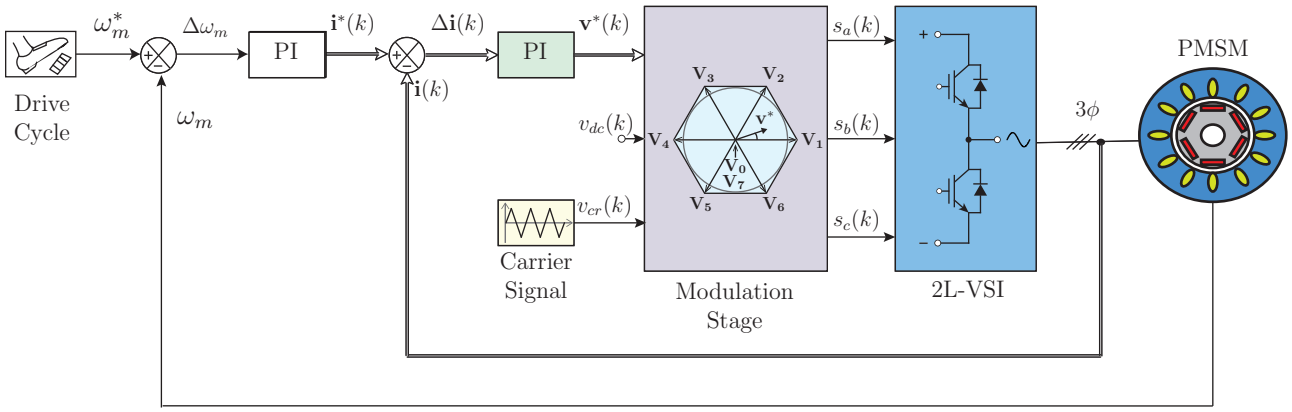

Figure 1.29: Block diagram of the linear control method.

The modulation stage requires a carrier (triangular) waveform v_{cr} and DC-link voltage v_{dc}, reference frame transformation, comparators, and switching logic internally to produce gating signals for 2L-VSI. PWM and SVM are the most commonly used modulation methods. The linear control method using PWM/SVM is operated with a fixed switching frequency, dictated by the carrier frequency. The performance of this control method greatly depends on the PI controller parameters and modulation type.

1.6.2 Hysteresis Control

Hysteresis control for three-phase systems is shown in Fig. 1.30. This is also known as non-linear control technique. In this scheme, the measured currents of the three-phase system are compared with the reference currents and the error is passed through to the relays as shown in the Fig. 1.30. This relays are also known as hysteresis comparators. This relays are responsible for determining the switching signals to the converter in such a way that measured values are confined within the range of hysteresis bandwidth set by the user.

The total bandwidth is symmetrically distributed around the sinusoidal reference current. When the motor current hits the upper band limit $(i_a^* + \frac{\delta}{2})$, the switching signal s_a is set to a logic low (0). The converter output voltage v_{aN} becomes zero, thus causing i_a to decay.

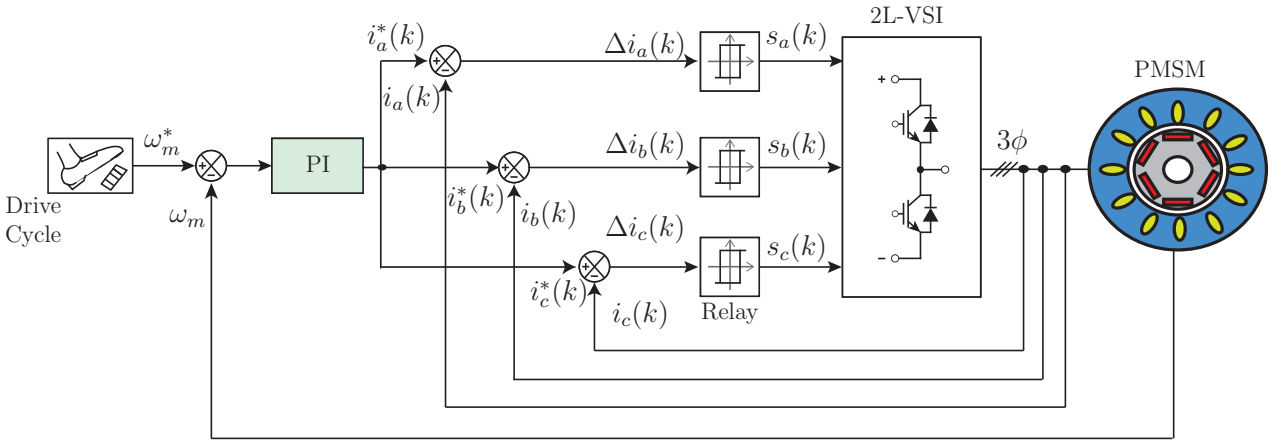

Figure 1.30: Hysteresis current control method for regulating three-phase load currents.

Similarly, the s_a is set to a logic high (1) when the motor current crosses the lower band limit $(i_a^* - \frac{\delta}{2})$. v_{aN} then becomes equal to v_{dc}, thus forcing i_a to increase. The advanced versions of hysteresis control method include Direct torque control and direct power control.

1.6.3 Finite Control-Set Model Predictive Control

Fig. 1.31 presents an FCS-MPC method for regulating motor currents. When compared to linear control, this method does not need to use linear PI regulators and modulation stage. This method offers a different concept and approach for power converters controlling [31]. This is truly a model-based optimization control method, and involves a large number of calculations.

The continuous time dynamic model of load current with RL-load for the 2L-VSI is simplified as:

$$\frac{d\,\mathbf{i}(t)}{dt} = -\frac{R}{L}\,\mathbf{i}(t) + \frac{1}{L}\,\mathbf{v}(t). \tag{1.1}$$

The above continuous-time dynamic model of load current is converted into a discrete-time model, as depicted below, for a sampling time T_s:

$$\mathbf{i}(k+1) = \mathbf{\Phi}\,\mathbf{i}(k) + \mathbf{\Gamma}\,\mathbf{v}(k) \tag{1.2}$$

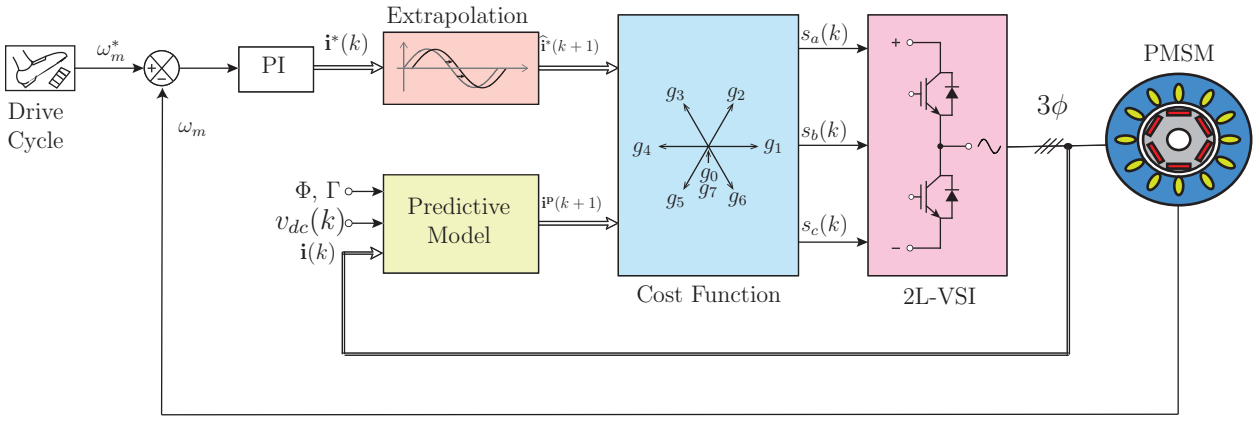

Figure 1.31: Block diagram of the FCS-MPC method.

where $\mathbf{\Phi}$ and $\mathbf{\Gamma}$ are the discrete time equivalents of the continuous time parameters $-R/L$ and $1/L$, respectively, and $\mathbf{i}(k+1)$ is the future load current.

The predictive model in (1.2) is used to calculate the future load current values. Where (n) is the number of switching states allows these values to be enumerated for all feasible switching states from 1 to n.

As a final stage, the predicted variables $i_0(k+1)$ to $i_7(k+1)$ are compared with their reference currents $\widehat{\mathbf{i}}^*(k+1)$ using a cost function $g(k)$ shown below:

$$g(k) = \left| \widehat{\mathbf{i}}^*(k+1) - \mathbf{i}(k+1) \right|. \tag{1.3}$$

The main objective of cost function optimization is to achieve g value which is close to zero. At the subsequent sampling instant, the switching state that minimizes the cost function is applied. At the $(k)^{th}$ instant, the algorithm selects a switching state which would minimize the cost function at the $(k+1)$ instant, and then applies this optimal switching state during the whole $(k+1)$ period. We could achieve fast transient response with this method. The time-average switching actions are not considered in this method, thus resulting cost function optimization process of the inherently produce variable switching frequency. This

is one of the disadvantage of FCS-MPC which produces higher current ripples and a wide distributed harmonic spectrum that can cause resonances in input and output filters [32].

1.6.4 Deadbeat Predictive Control

Fig. 1.32 presents a deadbeat predictive current control (DBPCC) method with a modulation stage. This method is similar to that of liner PI control method, but the PI regulator in linear control is replaced by the deadbeat controller. Deadbeat controller used in this method is responsible to predict future current behaviors during every sampling period similar to the FCS-MPC method using the load and converter models . Similarly, the controller selects the most appropriate reference voltage vector $\mathbf{v}^*$ and applies it to the modulation stage [33]. A PWM/SVM modulator is used to produce the gating signals to the power converter, resulting in a fixed switching frequency operation.

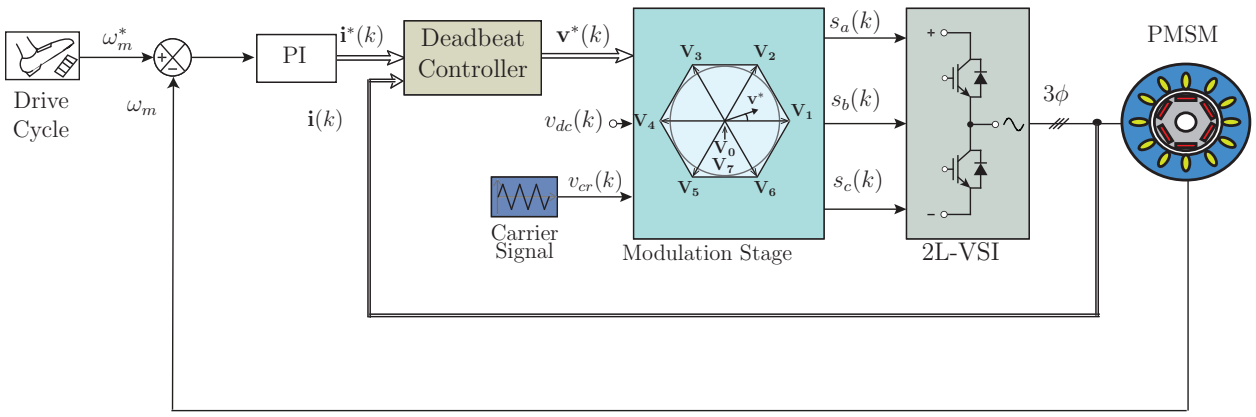

Figure 1.32: Block diagram of the deadbeat predictive control method.

This method uses the system model to predict the future behavior of the variables which needs to be controlled. This information is used by the controller to get estimate the optimal actuation. This control method mainly consists of the extrapolation of reference currents from $(k)^{\text{th}}$ to $(k+1)$ sampling instant. Following with a predictive model for calculating

future load currents similar to (1.2) in the FCS-MPC method.

Based on the Discrete Time model in (1.2), $\mathbf{v}^*(k)$ is calculated as follows:

$$\mathbf{v}^*(k) = \mathbf{\Gamma}^{-1}\left[\widehat{\mathbf{i}}^*(k+1) - \mathbf{\Phi}\,\mathbf{i}(k)\right] \tag{1.4}$$

where $\widehat{\mathbf{i}}^*(k+1)$ is the extrapolated reference current.

An optimal reference voltage vector $\mathbf{v}^*(k)$ produces zero current error at the next sampling instant $(k+1)$. This method uses a very simple approach and does not require any tuning in the process of optimization.

1.6.5 Modulated Model Predictive Control

Fig. 1.33 shows the block diagram of the M^{2}PCC method for regulating motor currents. The M^{2}PCC method is designed in such a way that it combines the operating principles of MPC and SVM [34,35]. M^{2}PCC method performs the process of cost function optimization in terms of duty cycles and then applies optimal voltage vectors corresponding to minimum cost function value to the converter through the SVM stage.

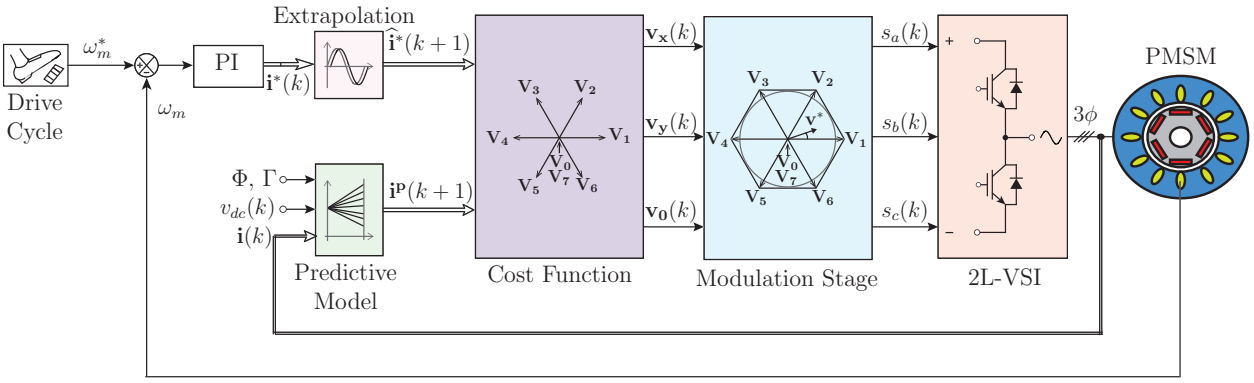

Figure 1.33: Block diagram of the modulated model predictive control method.

Just like in case of the FCS-MPC method, the M^{2}PCC method consists of the extrapolation of reference currents from $(k)^{\text{th}}$ to $(k+1)$ sampling instant. The predictive model

predicts the future behavior of load currents using the load model similar to (1.2). A cost function is formulated as in (1.3) to calculate the load current error for all the possible switching state.

In M^{2}PCC method, the reference voltage vector that lies in optimal sector is computed by using 8 functional values in (1.3). The active and zero vectors $\mathbf{V_x}$, $\mathbf{V_y}$ and $\mathbf{V_0}$ corresponding to the optimal sector are chosen in each sampling period to obtain fixed switching frequency for 2L-VSI. The cost functions corresponding to the voltage vectors $\mathbf{V_x}$, $\mathbf{V_y}$ and $\mathbf{V_0}$ are defined by g_x, g_y and g_0, respectively.

The duty cycles for three stationary voltage vectors are calculated as follows [34]:

$$\left.\begin{aligned} d_x &= \frac{g_y}{g_x + g_y + \frac{g_x g_y}{g_0}} \\ d_y &= \frac{g_x}{g_x + g_y + \frac{g_x g_y}{g_0}} \\ d_0 &= 1 - d_x - d_y. \end{aligned}\right\} \tag{1.5}$$

A new optimization function is used to compute the average load current tracking error in the six sectors of 2L-VSI as shown below:

$$J(k) = d_x\, g_x + d_y\, g_y + d_0\, g_0. \tag{1.6}$$

Finally, the three stationary vectors corresponding to the minimum cost function value in (1.6) are utilized by a modulation subsystem to produce switching signals for 2L-VSI. As a result, the switching frequency becomes fixed and steady-state error becomes lower than the FCS-MPC method. The transient response becomes faster since no PI controller is used in this method.

1.6.6 Summary of Main Features of Control Methods

Table 1.3 summarizes the popular features of the four control methods discussed above. These are described based on their control complexity, requirement for converter model and parameters, requirement for modulation stage, flexibility to include constraints and restrictions, steady-state error, dynamic response, and nature of converter switching frequency. In EV applications, the classical linear control with PI regulator and modulation stage method is the most popularly employed. On the other side, FCS-MPC, DBPCC and M^{2}PCC methods are recently developed and these method involves new concepts, designer's intuition, complex calculations, reference frame transformations, and often required powerful microprocessors.

Table 1.3: Summary of main features of digital current control methods.

	Linear (Fig. 1.29)	**Hysteresis (Fig. 1.30)**	**FCS-MPC (Fig. 1.31)**	**DBPCC (Fig. 1.32)**	**M^{2}PCC (Fig. 1.33)**
Control Complexity	Medium	Medium	Low-Medium	Medium	High
Model & Parameters	Needed	Needed	Needed	Needed	Needed
Modulation Stage	Needed	Not Needed	Not Needed	Needed	Needed
Constraint Inclusion	Not Possible	Not Possible	Possible	Not Possible	Possible
Steady-State Error	Low	Low	High	Low	Low
Dynamic Response	Average	Average	Excellent	Good	Excellent
Switching Frequency	Fixed	Fixed	Variable	Fixed	Fixed

1.6.7 Control Methods used in Commercial EVs

The motors in Tesla and Nissan electric cars notably use more advanced control methods, such as FOC, which adds to their high performance and efficiency. Tesla is known for its advanced EV technology, and while specific details about their control strategies are not

always publicly disclosed, it is widely believed that they use predictive control methods, including MPC, in various aspects of their vehicles, such as motor control and battery management [36]. Nissan has shown interest in advanced control strategies for their EVs. They have explored the use of predictive control in areas like regenerative braking and overall energy management for maximizing range.

Hyundai has been exploring advanced control methods for EVs. The Hyundai Motor Group, which includes Hyundai and Kia, has expressed interest in predictive control for aspects such as regenerative braking and overall energy management. The EV industry is dynamic, with ongoing research and development to improve efficiency, range, and overall performance.

1.7 Prior Research Works

The following configuration is considered for this thesis research:

- PMSM + 2L-VSI – Fig. 1.16.

As referenced before, advancement of refined control techniques is essential in expanding EVs proficiency and to build scope of EV. The improvement of control techniques for the power converters is a continuous exploration subject. The traditional direct control, FCS-MPC and M^{2}PCC strategies in the ongoing writing are summed up in Table 1.4 for the previously mentioned power transformation design. The traditional maximum torque per ampere (MTPA) control and MPC techniques are generally concentrated on in the ongoing writing. The M^{2}PCC strategy is at present read up for the power converters and engines. There are no examinations in applying M^{2}PCC technique for EV application. It is very important to consider the parameters like fixed switching frequency, low steady-state error, fast transient response in EVs for the smooth and efficient operation. These key parameters

are explained in more detail below.

- **Fixed Switching Frequency:** the purpose of maintaining a fixed switching frequency in EVs lies in achieving stable and predictable control of the power electronic devices within the motor drive system. By keeping the switching frequency constant, EV manufacturers can streamline the design and implementation of control algorithms, providing a consistent framework for optimal performance. Predictability in the switching frequency facilitates easier modeling of the system, enabling efficient hardware and software integration. Harmonics, which are unwanted sinusoidal components of the electrical waveform, can significantly impact the operation of motors in EVs. These harmonics, often introduced by power electronic converters in the EVs, can lead to increased losses, additional heating in the motor windings, and distorted current and voltage waveforms. The presence of harmonics may compromise the overall efficiency and performance of the motor [37]. High levels of harmonics can contribute to increased eddy current losses, hysteresis losses, and additional torque ripples, affecting the smoothness and reliability of the motor operation. Fixed switching frequency approach simplifies the design of filters, reduces harmonic distortion in output waveforms, and contributes to more straightforward thermal management in power electronic devices. Ultimately, the use of a fixed switching frequency in EVs enhances overall control precision, system reliability, and electromagnetic compatibility, promoting the efficient and reliable operation of EVs.
- **Low Steady-State Error:** achieving low steady-state error in EVs is paramount for ensuring accurate and responsive control of various systems within the vehicle. Steady-state error refers to the difference between the desired and actual states of a system once it has stabilized under a specific input. In the context of EVs, low steady-state error is crucial for precision in tasks such as speed regulation, torque control, and battery state-of-charge

maintenance. This precision is essential for providing a smooth and predictable driving experience while optimizing energy efficiency. Low steady-state error allows the control systems to accurately track reference signals, facilitating precise speed and torque control during acceleration, deceleration, and cruising. Additionally, in battery management, maintaining low steady-state error helps ensure that the actual state of the battery closely aligns with the desired state, contributing to accurate range estimation, effective energy utilization, and prolonging battery life. In summary, minimizing steady-state error in EVs is fundamental for achieving the desired performance, efficiency, and reliability in the various control systems that govern EV operation [38].

- **Fast Transient Response:** Fast transient response in EVs is crucial for ensuring dynamic and responsive control during rapid changes in driving conditions. Transient response refers to how quickly a system can adjust to sudden variations in input or operating conditions. In EVs, fast transient response is essential for achieving swift and precise control over the electric motor, ensuring rapid acceleration, deceleration, and effective energy recuperation during braking. It plays a critical role in enhancing overall vehicle performance, responsiveness, and drivability [39]. Fast transient response is particularly important for electric propulsion systems in scenarios such as sudden acceleration demands, abrupt changes in terrain, or quick adjustments in regenerative braking. This capability not only contributes to a more enjoyable and seamless driving experience but also plays a key role in optimizing energy efficiency and extending the range of EVs. In summary, fast transient response is a fundamental requirement for EVs, enabling them to adapt swiftly to varying driving conditions and deliver high-performance, dynamic control [40].

As summarized in Table 1.4, classical MTPA control discussed in [41,42] has fixed switching frequency and low steady-state error. By utilizing a fixed switching frequency, the control

Table 1.4: Key comparison between the prior works related to this thesis.

Work in	Applied to	Fixed Sw. Freq. ?	Low SS Error?	Fast Tran. Res.?	Applicable to EVs?
PMSM based EV with the 2L-VSI					
[41, 42]	Classical MTPA	✓	✓	✗	✓
[43, 44]	Classical PCC	✗	✗	✓	✓
[34, 35, 45, 46]	M^{2}PCC for 2L-VSI	✓	✓	✓	✗
[47–51]	M^{2}PCC for PM Motor	✓	✓	✓	✗
This Thesis	**M^{2}PCC 2L-VSI in PMSM based EVs**	✓	✓	✓	✓

algorithm simplifies the implementation and provides a consistent framework for managing power electronics. This stability is essential in MTPA control, allowing for precise and controlled adjustments to the motor current and voltage, optimizing torque output. The fixed switching frequency ensures a predictable operating environment, aiding in the management of electromagnetic interference, harmonic distortion, and overall system reliability. Low steady-state error in MTPA control contributes to optimized energy utilization, enhanced torque accuracy, and overall system reliability in EVs and other applications. It allows for consistent and accurate torque production, ensuring that the motor operates in line with the desired performance characteristics. Though MTPA has fixed switching frequency and low steady-state error, there is a drawback of slow transient response. One reason for the slow transient response in MTPA control is the nature of the control algorithm itself. MTPA control often involves complex computations and iterative processes to determine the optimal current vectors for achieving MTPA. These calculations, when performed in real-time, can introduce delays in the control system's response to sudden changes in input or operating conditions.

Predictive current control (PCC) is renowned for its fast transient response due to its

unique predictive and optimization-based approach. Unlike traditional control methods, PCC considers the future evolution of the system by solving an optimization problem over a specified time horizon. This predictive capability allows PCC to anticipate changes in the system's behavior and generate control actions that optimize a predefined objective. As discussed in [43,44], the iterative optimization process in PCC enables it to continually refine its predictions and adapt to dynamic changes, resulting in a rapid response to varying operating conditions. Furthermore, PCC incorporates constraints on the system variables, ensuring that the generated control inputs adhere to physical limitations and constraints. This adaptability to constraints contributes to stability and allows for a quick and accurate response during transient events. Overall, the combination of predictive modeling, optimization-based decision-making, and constraint handling makes PCC well-suited for achieving fast and precise transient responses in dynamic systems, such as electric motor drives in EVs. On the other hand, PCC has variable switching frequency and also have high steady state error due to inadequate handling of constraints and limited prediction horizon.

M^2PCC method has advantages of both PCC and linear control strategies. It has fixed switching frequency, low steady-state error and fast transient response unlike other control strategies. As discussed in [34, 35, 45, 46], M^2PCC is a control strategy that combines the advantages of predictive control with modulation techniques in electric motor drives. One notable characteristic of M^2PCC is the use of a fixed switching frequency, ensuring stability and simplifying the control implementation. This fixed frequency aids in predictable and consistent operation. Additionally, M^2PCC aims for low steady-state error, minimizing discrepancies between desired and actual system states during steady operation. This precision is crucial for accurate torque and current control. Simultaneously, M^2PCC achieves high transient response, allowing the system to quickly and effectively respond to changes in operating conditions. This combination of fixed switching frequency, low steady-state error,

and high transient response makes M^{2}PCC a robust and effective strategy for optimizing the performance of electric motor drives. Also, the performance of the PMSM using M^{2}PCC is explained in [47–51].

This thesis gives an overview of M^{2}PCC method of PMSM using 2L-VSI in EV applications. It explains how fixed switching frequency, low steady-state error and fast transient response is achieved using M^{2}PCC method for 2L-VSI and PMSM in EVs.

This thesis fills the gap in the current literature by performing the modeling, design and analysis of the M^{2}PCC method for the 2L-VSI in PMSM based EV applications.

1.8 Objectives of Thesis

The target application for this thesis research is 2L-VSI in PMSM based EV. The classical linear control, also known as MTPA, predictive current control (PCC) and M^{2}PCC methods are investigated in this thesis and applied to the EV converters. The proposed M^{2}PCC method exhibit fast transient response as in the classical PCC method, and fixed switching frequency operation and low steady-state error as in the classical MTPA control.

The thesis objectives in this regard are summarized as follows:

- The predictive control uses the model of system to predict the future behavior of system. To aid the design of control methods, the continuous- and discrete-time models of the PMSM and 2L-VSI are developed.
- To develop PCC method for the 2L-VSI in EV application.
- To develop M^{2}PCC method for the 2L-VSI for EV application.
- To analyze the performance of the PMSM based EV with 2L-VSI during steady-state and transient operation and verify the proposed mathematical models and control methods.

- To compare the performance of the proposed M^{2}PCC method with the classical MTPA and classical PCC methods through steady-state and transient studies.

1.9 Thesis Overview

The research presented in this thesis is organized into 5 chapters. The work carried out in each chapter is summarized as follows:

- **Introduction:** In this chapter, an overview of EVs, different power converters and control methods are discussed.
- **Modeling of PMSM and 2L-VSI:** The continuous-time and discrete-time dynamic models of the PMSM and 2L-VSI are obtained in the *dq*-reference frame. To improve the accuracy of predictions with less computational burden, a new discretization method based on matrix factorization is introduced.
- **Current Control of PMSM:** In this chapter, classical MTPA, PCC and M^{2}PCC methods are discussed for the EV application. The speed control loop, current control loop and calculation of reference motor currents are discussed in detail. A step-by-step procedure for the implementation of control schemes is discussed.
- **Simulation Results and Analysis:** In this chapter, simulation and results are discussed. Torque and speed of the motor with different conditions are analyzed. Also, stator currents for different control methods are also discussed. Results for classical PCC and M^{2}PCC methods are analyzed. The control methods are also compared during steady-state, transient conditions, and also through harmonic analysis.
- **Conclusion:** The conclusion and major contributions of this thesis research are summarized in this chapter. Possible extensions to the research presented in this thesis are also suggested.

CHAPTER 2

Modeling of PMSM and 2L-VSI

2.1 Introduction

As discussed in the chapter 1, main objective is to regulate the stator currents for the motor with 2L-VSI configuration. In general, the PCC scheme for 2L-VSI with PMSM based EVs have two predictive models in it. one corresponds to the 2L-VSI and other is related to the PMSM. The first predictive model is used to predict the output voltages of 2L-VSI by using eight switching state combinations and by measuring the battery (or dc-link) voltage. The output voltages which are predicted in this method are of synchronous frame. The second predictive model is used to predict the dq-axis stator currents by using the inverter output voltages along with feedback currents and rotor speed. The main purpose of in this chapter is to model the PMSM and 2L-VSI and combine these models. To improve the accuracy of predictions with less computational burden, a new discretization method based on matrix factorization is introduced.

Before discussing the modeling in detail, it is important to know the different types of reference frames and their transformations. These are explained in detail in the below section.

2.2 Reference Frame Transformations

To make the modeling, analysis, and simulation of balanced three-phase circuits, power converters, and electric machines simpler, reference frame theory applies mathematical transformation. In order to simplify the design, advanced digital control methods heavily depend on this principle and algorithm complexity. Reference frames are frequently used in three main categories in electrical engineering. These reference frames are categorized according to their speed of the variables' contexts and types of reference frames [52].

- Natural (abc) Reference Frame
- Stationary ($\alpha\beta$) Reference Frame
- Synchronous (dq) Reference Frame

2.2.1 Transformation Between Natural and Stationary Frames

The natural frame to stationary frame transformation projects the three-phase time-varying variables along the a, b, and c-phase axes onto two-phase time-varying variables along a pair of orthogonal axes (i.e., α and β).

The transformation of natural frame variables into stationary frame variables is also referred to as the $abc/\alpha\beta$ transformation:

$$\begin{bmatrix} i_\alpha \\ i_\beta \end{bmatrix} = \frac{2}{3} \begin{bmatrix} 1 & -\frac{1}{2} & -\frac{1}{2} \\ 0 & \frac{\sqrt{3}}{2} & -\frac{\sqrt{3}}{2} \end{bmatrix} \begin{bmatrix} i_a \\ i_b \\ i_c \end{bmatrix}. \tag{2.1}$$

For a three-phase balanced system, $i_a + i_b + i_c = 0$; thus, i_α becomes equal to i_a. The coefficient 2/3 is arbitrarily added to the equation to preserve equal magnitudes for three- and two-phase variables after transformation [52].

The inverse transformation (i.e., $\alpha\beta/abc$) from the stationary frame variables into the natural frame variables is obtained as:

$$\begin{bmatrix} i_a \\ i_b \\ i_c \end{bmatrix} = \begin{bmatrix} 1 & 0 \\ -\frac{1}{2} & \frac{\sqrt{3}}{2} \\ -\frac{1}{2} & -\frac{\sqrt{3}}{2} \end{bmatrix} \begin{bmatrix} i_\alpha \\ i_\beta \end{bmatrix}. \tag{2.2}$$

2.2.2 Transformation Between Natural and Synchronous Frames

Similar to the $abc/\alpha\beta$ transformation, three-phase natural frame variables are transformed into a two-phase synchronous reference frame along a pair of orthogonal axes d and q.

By simple calculations, the transformation of the abc-frame to the dq-frame is obtained as follows:

$$\begin{bmatrix} i_d \\ i_q \end{bmatrix} = \frac{2}{3} \begin{bmatrix} \cos\theta_r & \cos(\theta_r - \frac{2\pi}{3}) & \cos(\theta_r - \frac{4\pi}{3}) \\ -\sin\theta_r & -\sin(\theta_r - \frac{2\pi}{3}) & -\sin(\theta_r - \frac{4\pi}{3}) \end{bmatrix} \begin{bmatrix} i_a \\ i_b \\ i_c \end{bmatrix} \tag{2.3}$$

where, θ_r is PMSM rotor electrical position.

Similarly, the transformation of the dq-frame to the abc-frame is determined by the following equation:

$$\begin{bmatrix} i_a \\ i_b \\ i_c \end{bmatrix} = \begin{bmatrix} \cos\theta_r & -\sin\theta_r \\ \cos(\theta_r - \frac{2\pi}{3}) & -\sin(\theta_r - \frac{2\pi}{3}) \\ \cos(\theta_r - \frac{4\pi}{3}) & -\sin(\theta_r - \frac{4\pi}{3}) \end{bmatrix} \begin{bmatrix} i_d \\ i_q \end{bmatrix}. \tag{2.4}$$

2.2.3 Transformation Between Stationary and Synchronous Frames

Stationary frames variables are transformed into synchronous frame (i.e., $\alpha\beta/dq$ transformation) to convert two-phase stationary variables into rotating variables. This transfor-

mation matrix uses the angle of the space phasor as defined below:

$$\begin{bmatrix} i_d \\ i_q \end{bmatrix} = \begin{bmatrix} \cos\theta_r & \sin\theta_r \\ -\sin\theta_r & \cos\theta_r \end{bmatrix} \begin{bmatrix} i_\alpha \\ i_\beta \end{bmatrix}. \tag{2.5}$$

The inverse transformation (i.e., $dq/\alpha\beta$ transformation) from the synchronous reference frame into stationary reference frame is given by the following:

$$\begin{bmatrix} i_\alpha \\ i_\beta \end{bmatrix} = \begin{bmatrix} \cos\theta_r & -\sin\theta_r \\ \sin\theta_r & \cos\theta_r \end{bmatrix} \begin{bmatrix} i_d \\ i_q \end{bmatrix}. \tag{2.6}$$

2.3 Modeling of PMSM

In this section, detailed modeling of PMSM used for EV applications is presented. The configuration of IPMSM using 2L-VSI for EV application is shown in Fig. 2.1. 2L-VSI contains insulated gate bipolar transistor. The output of the motor is connected to the wheels of the EV through its gear box [52].

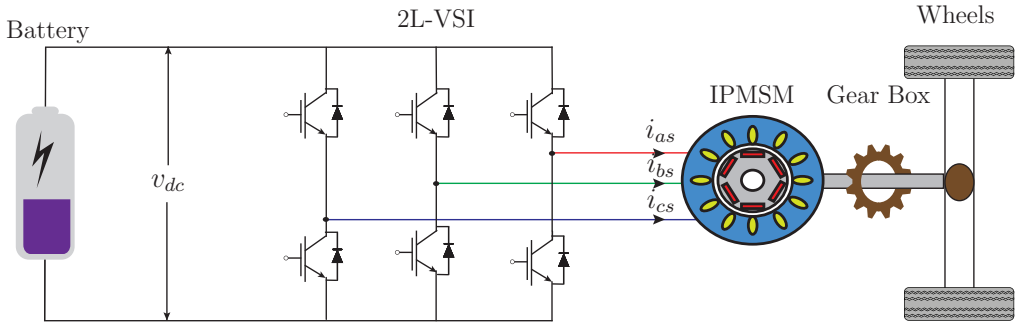

Figure 2.1: Configuration of the PMSM with 2L-VSI for EV applications.

2.3.1 Natural Frame

In a natural reference frame, the PMSM stator voltages are expressed below in terms of stator currents and flux linkages:

$$\begin{bmatrix} v_{as} \\ v_{bs} \\ v_{cs} \end{bmatrix} = \begin{bmatrix} R_s & 0 & 0 \\ 0 & R_s & 0 \\ 0 & 0 & R_s \end{bmatrix} \begin{bmatrix} i_{as} \\ i_{bs} \\ i_{cs} \end{bmatrix} + \frac{d}{dt} \begin{bmatrix} \psi_{as} \\ \psi_{bs} \\ \psi_{cs} \end{bmatrix} + \begin{bmatrix} v_{ns} \\ v_{ns} \\ v_{ns} \end{bmatrix} \tag{2.7}$$

where,

- v_{as}, v_{bs}, and v_{cs} are the machine phase *abc* stator voltages (V),
- i_{as}, i_{bs}, and i_{cs} are the machine phase *abc* stator currents (A),
- ψ_{as}, ψ_{bs}, and ψ_{cs} are the machine phase *abc* stator flux linkages (Wb),
- v_{ns} is the machine neutral-point voltage (V),
- R_s is the machine stator winding resistance (Ω).

The *abc* frame stator flux linkages originate from the permanent magnetic flux linkages and the current flowing through the machine self and mutual inductances. This process is demonstrated as follows:

$$\begin{bmatrix} \psi_{as} \\ \psi_{bs} \\ \psi_{cs} \end{bmatrix} = \begin{bmatrix} L_{aa} & M_{ab} & M_{ac} \\ M_{ab} & L_{bb} & M_{bc} \\ M_{ac} & M_{bc} & L_{cc} \end{bmatrix} \begin{bmatrix} i_{as} \\ i_{bs} \\ i_{cs} \end{bmatrix} + \begin{bmatrix} \psi_r \cos\theta_r \\ \psi_r \cos\left(\theta_r - \frac{2\pi}{3}\right) \\ \psi_r \cos\left(\theta_r - \frac{4\pi}{3}\right) \end{bmatrix} \tag{2.8}$$

where,

- L_{aa}, L_{bb} and L_{cc} are the machine phase *abc* self-inductances,
- M_{ab}, M_{bc} and M_{ac} are the machine mutual inductances between phase *abc*,
- ψ_r is the peak value of flux linkage created by the permanent magnets.

The three-phase PMSM stator voltages are expressed as below in natural reference frame.

$$\frac{d}{dt}\begin{bmatrix} v_{as} \\ v_{bs} \\ v_{cs} \end{bmatrix} = \begin{bmatrix} R_s & 0 & 0 \\ 0 & R_s & 0 \\ 0 & 0 & R_s \end{bmatrix} \begin{bmatrix} i_{as} \\ i_{bs} \\ i_{cs} \end{bmatrix} + \frac{d}{dt}\begin{bmatrix} \psi_{as} \\ \psi_{bs} \\ \psi_{cs} \end{bmatrix} + \begin{bmatrix} v_{ns} \\ v_{ns} \\ v_{ns} \end{bmatrix}. \tag{2.9}$$

2.3.2 Synchronous Frame

The inductances in the three-phase model vary with respect to the rotor position, making the modeling complex. To obtain the final model of PMSM in natural frame, derivative and inverse operations must be performed on the third order time varying matrix which is very much complex. For this reason, the modeling of PMSM in synchronous frame is presented in this section. Subscripts d and q correspond to the orthogonal synchronous-frame axes. All the dq-frame variables are DC in nature.

To obtain the voltage equations into synchronous reference frame, the voltages in natural (abc) frame are converted into stationary reference frame ($\alpha\beta$) using the (2.3) [52]. Now the voltage equations in the synchronous frame can be written as follows:

$$\begin{bmatrix} v_{ds} \\ v_{qs} \end{bmatrix} = \begin{bmatrix} R_s & 0 \\ 0 & R_s \end{bmatrix} \begin{bmatrix} i_{ds} \\ i_{qs} \end{bmatrix} + \frac{d}{dt}\begin{bmatrix} \psi_{ds} \\ \psi_{qs} \end{bmatrix} + \begin{bmatrix} 0 & -\omega_r \\ \omega_r & 0 \end{bmatrix} \begin{bmatrix} \psi_{ds} \\ \psi_{qs} \end{bmatrix} \tag{2.10}$$

where, v_{ds} and v_{qs} are PMSM stator voltages, i_{ds} and i_{qs} are PMSM stator currents, ψ_{ds} and ψ_{qs} are stator flux linkages, ω_r is rotor electrical speed.

The stator flux linkages in synchronous reference frame are represented as below:

$$\begin{bmatrix} \psi_{ds} \\ \psi_{qs} \end{bmatrix} = \begin{bmatrix} L_{ds} & 0 \\ 0 & L_{qs} \end{bmatrix} \begin{bmatrix} i_{ds} \\ i_{qs} \end{bmatrix} + \begin{bmatrix} \psi_r \\ 0 \end{bmatrix}. \tag{2.11}$$

By combining the equations (2.10) and (2.11), the final stator voltages in synchronous

reference frame can be calculated as demonstrated below:

$$\begin{bmatrix} v_{ds} \\ v_{qs} \end{bmatrix} = \begin{bmatrix} R_s & -\omega_r L_{qs} \\ \omega_r L_{ds} & R_s \end{bmatrix} \begin{bmatrix} i_{ds} \\ i_{qs} \end{bmatrix} + \begin{bmatrix} L_{ds} & 0 \\ 0 & L_{qs} \end{bmatrix} \frac{d}{dt} \begin{bmatrix} i_{ds} \\ i_{qs} \end{bmatrix} + \begin{bmatrix} 0 \\ \omega_r \psi_r \end{bmatrix}. \tag{2.12}$$

2.3.3 Continuous-Time Model

The continuous-time model of IPMSM dq-axis stator currents is defined as follows:

$$\frac{d}{dt} \begin{bmatrix} i_{ds} \\ i_{qs} \end{bmatrix} = \mathbf{A_s}(t) \begin{bmatrix} i_{ds} \\ i_{qs} \end{bmatrix} + \mathbf{B_s} \begin{bmatrix} v_{ds} \\ v_{qs} \end{bmatrix} + \mathbf{w}(t). \tag{2.13}$$

The continuous-time matrices in the system are expressed in terms of rotor electrical speed (ω_r) and generator parameters as,

$$\mathbf{A_s}(t) = \begin{bmatrix} -\frac{R_s}{L_{ds}} & \frac{\omega_r L_{qs}}{L_{ds}} \\ -\frac{\omega_r L_{ds}}{L_{qs}} & -\frac{R_s}{L_{qs}} \end{bmatrix}, \quad \mathbf{B_s} = \begin{bmatrix} \frac{1}{L_{ds}} & 0 \\ 0 & \frac{1}{L_{qs}} \end{bmatrix}, \quad \mathbf{w}(t) = \begin{bmatrix} 0 \\ -\frac{\omega_r(t)\,\psi_r}{L_{qs}} \end{bmatrix}. \tag{2.14}$$

The above continuous-time linear time-variant (LTV) state-space model shown in (2.13) is presented in a generic form as follows:

$$\begin{aligned} \dot{\mathbf{x}}(t) &= \mathbf{A}\,\mathbf{x}(t) + \mathbf{B}\,\mathbf{u}(t) + \mathbf{w}(t) \\ \mathbf{y}(t) &= \mathbf{C}\,\mathbf{x}(t) \end{aligned} \tag{2.15}$$

where $\mathbf{x}(t)$ is the state vector, $\mathbf{u}(t)$ is the input or control vector, $\mathbf{w}(t)$ is a disturbance vector, and $\mathbf{y}(t)$ is the output vector. The matrices are as follows: $\mathbf{A}$ is the state or system matrix, $\mathbf{B}$ is the input or control or disturbance matrix, and $\mathbf{C}$ is the output matrix.

Therefore, the overall equation can be represented as:

$$\underbrace{\frac{d}{dt}\begin{bmatrix} i_{ds} \\ i_{qs} \end{bmatrix}}_{\dot{\mathbf{x}}(t)} = \underbrace{\begin{bmatrix} -\frac{R_s}{L_{ds}} & \frac{\omega_r L_{qs}}{L_{ds}} \\ -\frac{\omega_r L_{ds}}{L_{qs}} & -\frac{R_s}{L_{qs}} \end{bmatrix}}_{\mathbf{A}} \underbrace{\begin{bmatrix} i_{ds} \\ i_{qs} \end{bmatrix}}_{\mathbf{x}(t)} + \underbrace{\begin{bmatrix} \frac{1}{L_{ds}} & 0 \\ 0 & \frac{1}{L_{qs}} \end{bmatrix}}_{\mathbf{B}} \underbrace{\begin{bmatrix} v_{ds} \\ v_{qs} \end{bmatrix}}_{\mathbf{u}(t)} + \underbrace{\begin{bmatrix} 0 \\ -\frac{\omega_r(t)\,\psi_r}{L_{qs}} \end{bmatrix}}_{\mathbf{w}(t)}. \tag{2.16}$$

2.3.4 Discrete-Time Model using Forward Euler Method

Due to $\omega_r(t)$ term in state matrix $\mathbf{A_s}(t)$ in (2.14), the model is linearly time-varying. Therefore, it is difficult to obtain the exact discrete models by using the zero-order hold (ZOH).

To obtain the approximate discrete-time equivalent of continuous-time matrices in (2.13), the forward Euler method shown in can be used as follows.

$$x(k+1) \approx x(k) + T_s \left\{ \frac{d\,x(t)}{dt} \right\}_{t=k}, \quad x \in \{i_{ds},\, i_{qs}\}\,. \tag{2.17}$$

By substituting (2.17) into (2.13), the approximate discrete-time matrices are derived as,

$$\begin{bmatrix} i^p_{ds}(k+1) \\ i^p_{qs}(k+1) \end{bmatrix} = \mathbf{\Phi_s}(k) \begin{bmatrix} i_{ds}(k) \\ i_{qs}(k) \end{bmatrix} + \mathbf{\Gamma_s} \begin{bmatrix} v^p_{ds}(k) \\ v^p_{qs}(k) \end{bmatrix} + \mathbf{\Gamma_w}(k) \tag{2.18}$$

where, p is the predicted variable.

The discrete-time matrices are computed as,

$$\mathbf{\Phi_s}(k) \approx [\mathbf{I} + \mathbf{A_s}(k)\,T_s] \approx \begin{bmatrix} 1 - \frac{R_s\,T_s}{L_{ds}} & \frac{\omega_r(k) L_{qs} T_s}{L_{ds}} \\ \frac{-\omega_r(k) L_{ds} T_s}{L_{qs}} & 1 - \frac{R_s\,T_s}{L_{qs}} \end{bmatrix}, \tag{2.19}$$

$$\mathbf{\Gamma_b} \approx \mathbf{B_s}\,T_s \approx \begin{bmatrix} \frac{T_s}{L_{ds}} & 0 \\ 0 & \frac{T_s}{L_{qs}} \end{bmatrix}, \tag{2.20}$$

$$\mathbf{\Gamma_w}(k) \approx \mathbf{w}(k)\,T_s \approx \begin{bmatrix} 0 \\ -\frac{\omega_r(k)\,\psi_r\,T_s}{L_{qs}} \end{bmatrix}. \tag{2.21}$$

The discrete-time counterpart of the continuous-time LTV state-space model shown in (2.15) is defined by the following:

$$\begin{aligned} \mathbf{x}(k+1) &= \mathbf{\Phi_s}\,\mathbf{x}(k) + \mathbf{\Gamma_b}\,\mathbf{u}(k) + \mathbf{\Gamma_w}(k) \\ \mathbf{y}(k) &= \mathbf{x}(k+1) \end{aligned} \tag{2.22}$$

where $\mathbf{\Phi_s}(k)$, $\mathbf{\Gamma_b}$, and $\mathbf{\Gamma_w}(k)$ are the discrete-time matrices corresponding to continuous-time matrices $\mathbf{A_s}$, $\mathbf{B_s}$, and $\mathbf{w}$, respectively.

2.3.5 Discrete-Time Model using Matrix Decomposition Method

The forward Euler approximation method is simple and straightforward; however, the discretization accuracy deteriorates. Matrix decomposition method for an IPMSM is discussed in this chapter obtain the discrete-time models with higher discretization accuracy. As a first step in the discretization, matrix $\mathbf{A_s}(t)$ is split into $\mathbf{A_{cs}}$ and $\mathbf{A_{\omega s}}(t)$. The matrix $\mathbf{A_{cs}}$ contains time-invariant variables and the matrix $\mathbf{A_{\omega s}}(t)$ is made-up of time-variant variable, $\omega_r(t)$. With this matrix decomposition, the discretization of $\mathbf{\Phi_s}(k)$ is given as,

$$\mathbf{\Phi_s}(k) = e^{\mathbf{A_{cs}}T_s} \cdot e^{\mathbf{A_{\omega s}}(k)T_s} = \begin{bmatrix} e^{-\frac{R_s\,T_s}{L_{ds}}} & 0 \\ 0 & e^{-\frac{R_s\,T_s}{L_{qs}}} \end{bmatrix} \begin{bmatrix} \cos\,(\omega_r\,T_s) & \frac{L_{qs}\sin\,(\omega_r\,T_s)}{L_{ds}} \\ -\frac{L_{ds}\sin\,(\omega_r\,T_s)}{L_{qs}} & \cos\,(\omega_r\,T_s) \end{bmatrix}. \tag{2.23}$$

The quasi-exact discrete-time matrices $\mathbf{\Gamma_s}$ and $\mathbf{\Gamma_w}(k)$ are computed as follows:

$$\mathbf{\Gamma_s} \cong \mathbf{A_{cs}^{-1}}\left(e^{\mathbf{A_{cs}}T_s} - \mathbf{I}\right)\mathbf{B_s},\ \mathbf{\Gamma_w}(k) \cong \mathbf{A_{cs}^{-1}}\left(e^{\mathbf{A_{cs}}T_s} - \mathbf{I}\right)\mathbf{w}(k). \tag{2.24}$$

2.3.6 Mechanical Equations

The mechanical rotor speed dynamics are given as

$$J_m\,\frac{d}{dt}\,\omega_m + B_m\,\omega_m = T_e - T_m \tag{2.25}$$

where,

- ω_m is rotor mechanical speed (rad/s),
- T_e and T_m are electromagnetic and shaft mechanical torques (N.m),
- J_m and B_m are shaft moment of inertia (kg.m^2) and viscous friction (N.m.s).

In motor drive applications, T_e and T_m have positive signs. In steady state, the derivative term in (2.25) becomes zero. The value of T_e must be slightly higher than T_m to compensate for the loss due to viscous friction ($T_e - T_m = B_m\,\omega_m$). By substituting values for T_m and T_e in (2.25), the overall difference in steady state becomes the same as with the motor drive case, i.e., $T_e - T_m = B_m\,\omega_m$. The mechanical rotor speed ω_m is related to the electrical rotor speed ω_r as demonstrated below [53]:

$$\omega_m = \frac{1}{P_p}\,\omega_r \tag{2.26}$$

where, P_p represents number of pole pairs of PMSM.

By combining (2.25) and (2.26), the electrical rotor speed dynamics are given below:

$$\frac{J_m}{P_p}\,\frac{d}{dt}\,\omega_r + \frac{B_m}{P_p}\,\omega_r = T_e - T_m \tag{2.27}$$

from which,

$$\frac{d}{dt}\,\omega_r = \frac{P_p}{J_m}\,(T_e - T_m) - \frac{B_m}{J_m}\,\omega_r. \tag{2.28}$$

The mechanical and electrical rotor position angles are given as

$$\theta_m = \frac{d}{dt}\,\omega_m, \quad \theta_r = \frac{d}{dt}\,\omega_r, \quad \theta_m = \frac{1}{P_p}\,\theta_r. \tag{2.29}$$

2.3.7 Active and Reactive Power Calculation

The stator active and reactive powers are computed as follows:

$$P_s = \frac{3}{2}\,(v_{ds}\,i_{ds} + v_{qs}\,i_{qs})\,, \tag{2.30}$$

$$Q_s = \frac{3}{2}\,(v_{qs}\,i_{ds} - v_{ds}\,i_{qs})\,. \tag{2.31}$$

After substituting the v_{ds} and v_{qs} values from (2.10) into (2.30), the stator active power

is expressed as follows:

$$P_s = \frac{3}{2} R_s \left(i_{ds}^2 + i_{qs}^2 \right) + \frac{3}{2} \left(i_{ds} \frac{d\,\psi_{ds}}{dt} + i_{qs} \frac{d\,\psi_{qs}}{dt} \right) + \frac{3}{2} \omega_r \left(\psi_{ds}\, i_{qs} - \psi_{qs}\, i_{ds} \right) \tag{2.32}$$

where, the first term represents the Ohmic losses in the stator winding resistance, the second term corresponds to the stored power in the magnetic field, and the third term expresses the air gap power, which is responsible for the production of T_e.

Similarly, the stator reactive power is computed as follows:

$$Q_s = \frac{3}{2} \left(i_{ds} \frac{d\,\psi_{qs}}{dt} - i_{qs} \frac{d\,\psi_{ds}}{dt} \right) + \frac{3}{2} \omega_r \left(\psi_{ds}\, i_{ds} + \psi_{qs}\, i_{qs} \right). \tag{2.33}$$

Similarly, the electromagnetic torque for IPMSM can be calculated using:

$$T_e = \frac{3\,P_p}{2} \left[\psi_r\, i_{qs} + \left(L_{ds} - L_{qs} \right) i_{ds}\, i_{qs} \right]. \tag{2.34}$$

2.4 Modeling of 2L-VSI

This section deals with the modeling of stator current dynamics in terms of 2L-VSI terminal voltages and switching states.

2.4.1 Power Circuit

To analyze the three-phase or multi-phase applications, only one phase of 2L-VSI can be considered first and to the models can be extended to required number of phases. The power circuit diagram for one phase in the 2L-VSI is shown in Fig. 2.2.

2.4.2 Modes of Operation

Considering a 2L-VSI with two switches for each phase, there are two possible modes of operation. The operating modes for 2L-VSI are shown in Fig. 2.3. The switching actions

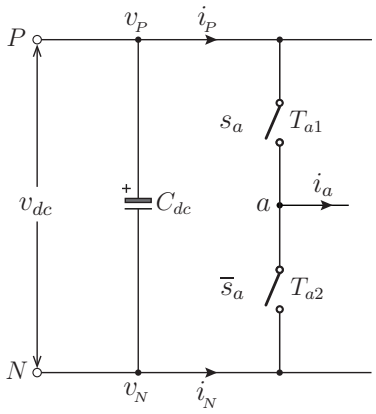

Figure 2.2: Per-phase 2L-VSI power circuit using generic switches.

and corresponding converter output voltages in the two operating modes for phase a are presented as follows:

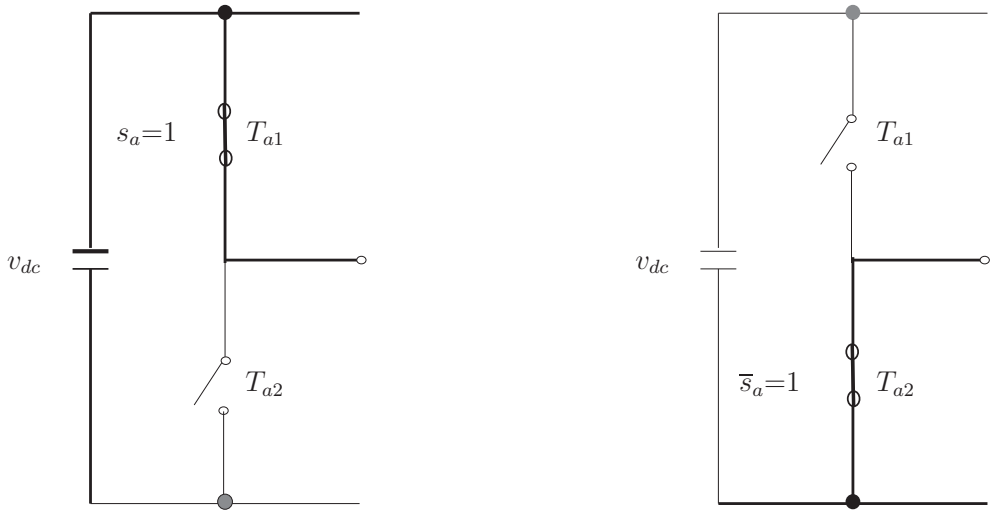

(a) (b)

Figure 2.3: Operating modes of 2L-VSI per phase (a) Mode-I : $s_a = 1$ (a) Mode-II : $\overline{s}_a = 1$

Mode-I: As shown in Fig. 2.3(a), the upper switch T_{a1} is closed by enabling the switching signal s_a and lower switch T_{a2} is opened by disabling switching signal s_a. Therefore, the output voltage of 2L-VSI phase-a with respect to negative dc-bus N becomes equal to that of input voltage v_{dc}.

Mode-II: In mode 2, the upper switch T_{a1} is opened by disabling the switching signal s_a and lower switch T_{a2} is closed by enabling switching signal $\overline{s}_a$ [46]. Therefore, the output voltage of 2L-VSI phase-a with respect to negative dc-bus N becomes zero. The inverter output voltages for a three-phase 2L-VSI can be written as below for all $x\epsilon\{a,b,c\}$.

$$v_a = \begin{cases} v_{dc} & ;T_{a1} = \text{on},\ T_{a2} = \text{off} \\ 0 & ;T_{a1} = \text{off},\ T_{a2} = \text{on} \end{cases} \tag{2.35}$$

2.4.3 Switching States

To simplify the analysis and perform comparison between different variables of 2L-VSI, a switching vector is defined as follows.

$$\mathbf{S_a} = \begin{cases} [\mathbf{1}] & \text{if } T_{a1} \text{ is on} \quad (s_a = 1), \\ [\mathbf{0}] & \text{if } T_{a1} \text{ is off} \quad (s_a = 0). \end{cases} \quad \forall\ a \in \{x, y, z\} \tag{2.36}$$

The relationship between the switching vector $\mathbf{S_x}$ and their corresponding switching signals, converter output voltages, and DC branch currents are listed in Table 2.1.

Table 2.1: Switching states and output voltages for a 2L-VSI $\quad \forall\ a \in \{x, y, z\}$.

Switching Vector	**Switching Signals**		**Output Voltage**	**Input Currents**	
$\mathbf{S_a}$	s_a	$\overline{s}_a$	v_{aN}	i_P	i_N
[**1**]	1	0	v_{C1}	i_x	0
[**0**]	0	1	0	0	i_x

The possible number of combinations for a three-phase 2L-VSI becomes eight with two switching vectors [1] and [0] in each phase. A space vector diagram that contains these eight combinations is shown in Fig. 2.4 [46].

As shown in the Fig. 2.4, the switching vector combinations are used to represent the

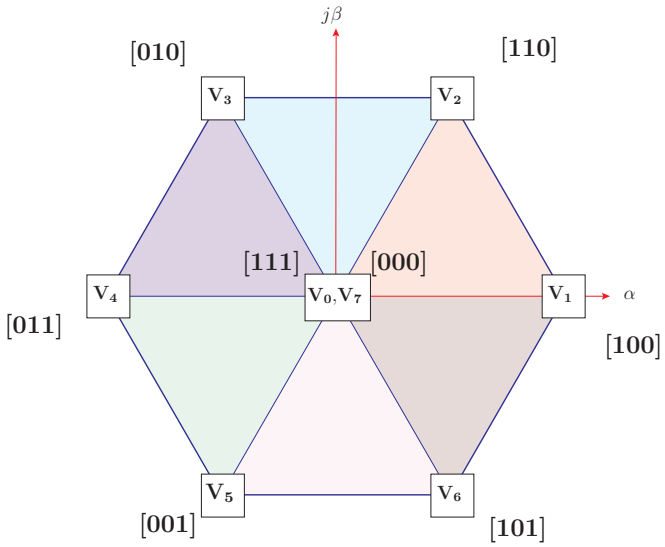

Figure 2.4: Space vector diagram for the 2L-VSI.

voltage vectors. For example, the vector combination [100] represents vector V_1 and so on [46].

The three-phase voltages for 2L-VSI with respect to input voltage and switching signals can be written as:

$$\begin{bmatrix} v_{as} \\ v_{bs} \\ v_{cs} \end{bmatrix} = v_{dc} \begin{bmatrix} s_a \\ s_b \\ s_c \end{bmatrix} \tag{2.37}$$

Notations of variables used in 2L-VSI is shown in the Table 2.2.

For motor-connected VSIs, it is typically necessary to estimate the inverter output voltages with regard to the neutral n of the motor. The inverter output voltages with regard to n are readily calculated using the "phase to neutral switching signals". The following is an offline calculation of the phase-neutral switching signals using the natural-frame switching signals.

$$\begin{bmatrix} s_{an} \\ s_{bn} \\ s_{cn} \end{bmatrix} = \begin{bmatrix} \frac{2}{3} & -\frac{1}{3} & -\frac{1}{3} \\ -\frac{1}{3} & \frac{2}{3} & -\frac{1}{3} \\ -\frac{1}{3} & -\frac{1}{3} & \frac{2}{3} \end{bmatrix} \begin{bmatrix} s_a \\ s_b \\ s_c \end{bmatrix}. \tag{2.38}$$

Table 2.2: Summary of the notation of variables for a 2L-VSI

Switching Combination	**Voltage Vector**	**Switching Vector**	**Upper-Leg Switching Signals**			**Phase to Neutral Switching Signals**			**Stationary Frame Switching Signals**	
s	**V**	$\mathbf{S_{abc}}$	s_a	s_b	s_c	s_{an}	s_{bn}	s_{cn}	s_α	s_β
$\mathbf{s_0}$	$\mathbf{V_0}$	[**000**]	0	0	0	0	0	0	0	0
$\mathbf{s_1}$	$\mathbf{V_1}$	[**100**]	1	0	0	$\frac{2}{3}$	$-\frac{1}{3}$	$-\frac{1}{3}$	$\frac{2}{3}$	0
$\mathbf{s_2}$	$\mathbf{V_2}$	[**110**]	1	1	0	$\frac{1}{3}$	$\frac{1}{3}$	$-\frac{2}{3}$	$\frac{1}{3}$	$\frac{\sqrt{3}}{3}$
$\mathbf{s_3}$	$\mathbf{V_3}$	[**010**]	0	1	0	$-\frac{1}{3}$	$\frac{2}{3}$	$-\frac{1}{3}$	$-\frac{1}{3}$	$\frac{\sqrt{3}}{3}$
$\mathbf{s_4}$	$\mathbf{V_4}$	[**011**]	0	1	1	$-\frac{2}{3}$	$\frac{1}{3}$	$\frac{1}{3}$	$-\frac{2}{3}$	0
$\mathbf{s_5}$	$\mathbf{V_5}$	[**001**]	0	0	1	$-\frac{1}{3}$	$-\frac{1}{3}$	$\frac{2}{3}$	$-\frac{1}{3}$	$-\frac{\sqrt{3}}{3}$
$\mathbf{s_6}$	$\mathbf{V_6}$	[**101**]	1	0	1	$\frac{1}{3}$	$-\frac{2}{3}$	$\frac{1}{3}$	$\frac{1}{3}$	$-\frac{\sqrt{3}}{3}$
$\mathbf{s_7}$	$\mathbf{V_0}$	[**111**]	1	1	1	0	0	0	0	0

In power converter analysis, it is usually convenient to express a set of switching signals as a variable. The many combinations that are conceivable for the switching states are identified by the switching state combination. In a 2L-VSI, for instance, switching state combinations are represented by the values $\mathbf{s_0}$ to $\mathbf{s_7}$.

The 2L-VSI output voltages in dq-frame are predicted similar to equation (2.37), that is,

$$\begin{bmatrix} v_{ds} \\ v_{qs} \end{bmatrix} = v_{dc} \begin{bmatrix} \cos\theta_r & \sin\theta_r \\ -\sin\theta_r & \cos\theta_r \end{bmatrix} \begin{bmatrix} s_\alpha \\ s_\beta \end{bmatrix} \tag{2.39}$$

where, s_α and s_β are the 2L-VSI switching signals in $\alpha\beta$-frame [46].

CHAPTER 3

Current Control of PMSM

3.1 Introduction

In the EV industry, MTPA control which belongs to the FOC family is widely accepted control method to obtain fixed switching frequency and good steady-state performance. Nevertheless, PI controllers are highly sensitive to the parameter variations.

More advanced control methods are needed to increase the energy conversion efficiency and dynamic performance for PMSM. Among the class of nonlinear control methods, PCC gained attention in power electronics research community as an attractive alternative to the classical control [54]. This is due to many superior characteristics such as intuitive concept, digital controller friendliness, fast dynamic response, and ability to handle constraints and nonlinearities. The work in [52] developed MPC methods for 2L-VSI fed IPMSM to accomplish fast dynamic response. However, in the classical PCC only one optimal voltage vector is applied to the inverter during entire sampling period, leading to high current ripple in steady-state and variable switching frequency operation [32]. To solve the variable switching frequency problem, the authors in [34] developed modulated PCC which optimizes the cost function in terms of duty cycles.

This chapter proposes a novel M^2PCC for 2L-VSI fed IPMSM for EV applications. The

proposed method provides the basis for combining salient features of the classical PCC and SVM into a reliable and effective control system to provide enhanced control performance. The proposed control method employs two independent cost functions to minimize the error between the reference and predicted currents.

3.2 Classical MTPA Control

The classical MTPA control for an IPMSM in EV application is shown in Fig. 3.1. In this method, the modulation stage uses a carrier waveform v_{cr} and input voltage v_{dc}, to produce gating signals for 2L-VSI. PWM and SVM [41] are popularly used modulation schemes.

3.2.1 Measurement of Feedback Variables

The first step in the MTPA strategy is to measure the feedback battery voltage and three-phase currents. The three-phase currents are converted to *dq*-frame using the models in (2.3).

3.2.2 Calculation of Reference Currents

For IPMSM, the saliency in the magnetic circuit of the rotor results in the high saliency ratio L_{qs}/L_{ds} of more than 1. This produces the reluctance torque in the rotor in additional to the existing electromagnetic torque [42] . Therefore, it is possible to operate motor with optimum values of i_{ds} and i_{qs} and obtain high torque for same stator current.

Using the drive cycle as an input, the vehicle control system calculates the reference mechanical rotor speed. A PI controller acts on the rotor speed error $\Delta\,\omega_m(k)$ to calculate the reference torque T_e^*, as demonstrated below:

$$T_e^*(k) = \left(k_p + \frac{k_i}{s}\right)\left[\omega_m^*(k) - \omega_m(k)\right] \tag{3.1}$$

where, s is the Laplace operator; k_p and k_i are the proportional and integral gains.

Standard Approach

The steady-state dq-axis stator flux linkages are obtained from as,

$$\left.\begin{aligned} \psi_{ds} &= L_{ds} i_{ds} + \psi_r \\ \psi_{qs} &= L_{qs} i_{qs} \end{aligned}\right\} \tag{3.2}$$

where, i_{ds} and i_{qs} are the stator currents , L_{ds} and L_{qs} are dq-axis inductances and ψ_r is peak value of flux linkages.

The electromagnetic torque of IPMSM can be calculated as follows:

$$\left.\begin{aligned} T_e &= \frac{P_m P_p}{\omega_r} = 1.5 P_p \left(\psi_{ds} i_{qs} - \psi_{qs} i_{ds}\right) \\ &= 1.5 P_p \left[\psi_r i_{qs} + \left(L_{ds} - L_{qs}\right) i_{ds} i_{qs}\right] \end{aligned}\right\} \tag{3.3}$$

where, P_m is the mechanical power input to IPMSM and P_p is number of pole pairs.

The MTPA strategy produces the maximum torque using the minimum values of i_{ds} and i_{qs} by adjusting the ratio between them. Therefore, the model in (3.3) can be re-written as,

$$T_e = 1.5 P_p \left[\psi_r i_{qs} + \left(L_{ds} - L_{qs}\right) \left(\sqrt{i_s^2 - i_{qs}^2}\right) i_{qs}\right]. \tag{3.4}$$

The model in (3.4) is differentiated with respect to i_{qs} to obtain the value for i_{ds}. The final model for i_{ds} is as follows:

$$i_{ds} = -\frac{\psi_r}{2\left(L_{ds} - L_{ds}\right)} \pm \sqrt{\frac{\psi_r^2}{4\left(L_{ds} - L_{ds}\right)^2} + i_{qs}^2}, \qquad L_{ds} \neq L_{qs}. \tag{3.5}$$

To obtain the minimum value for i_{ds}, the negative term is used in the right side of the expression.

From the models expressed in (3.3) and (3.4), the reference dq-axes currents to achieve

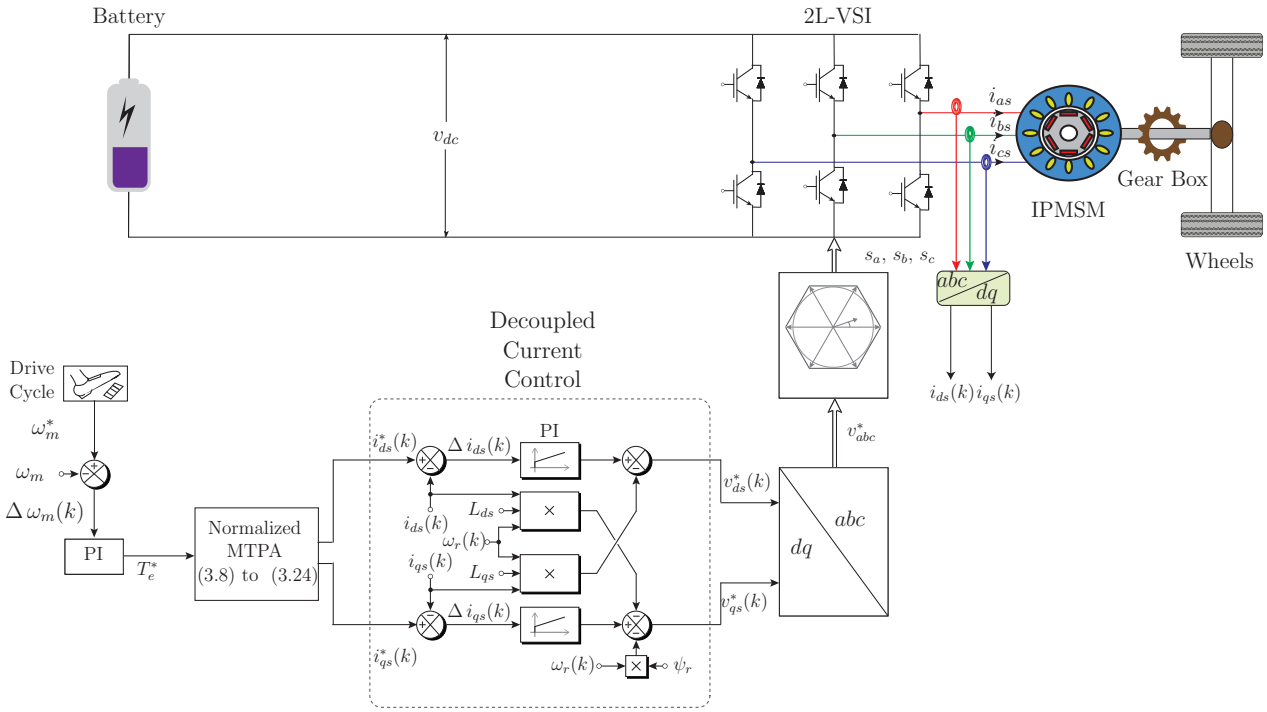

Figure 3.1: Block diagram for classical MTPA control of 2L-VSI with PMSM.

the MTPA operation are defined by the following:

$$i_{qs}^*(k) = \frac{T_e^*(k)}{1.5\,P_p\,[\psi_r + (L_{ds} - L_{qs})\,i_{ds}(k)]}, \tag{3.6}$$

$$i_{ds}^*(k) = -\frac{\psi_r}{2\,(L_{ds} - L_{qs})} - \sqrt{\frac{\psi_r^2}{4\,(L_{ds} - L_{qs})^2} + [i_{qs}^*(k)]^2}. \tag{3.7}$$

The analysis for the calculation of ω_m^*, T_e^*, i_{ds}^* and i_{qs}^* can be applied for any control method, including classical PCC and proposed M^{2}PCC method. With the standard approach discussed above, the generated reference currents are not accurate. So, normalization is done for torque and stator currents in order to perform the field weakening operations at overspeed conditions.

Normalized MTPA Approach

The equations discussed in the standard approach are very difficult to solve. The inductance parameters L_{ds} and L_{qs} are not equal in case of IPMSM, therefore it is very difficult to define the machine parameters and torque-speed characteristics of the motor. Due to this, it is very complex to minimize the stator currents in overspeed condition, as torque depends on the parameters of the motor. To overcome this problem, there is an interesting approach called standardization of torque and power [55]. This method allows elimination of parameters dependence in torque equation to minimize the currents in overspeed conditions.

Control diagram for normalized MTPA approach is shown in Fig. 3.2. Reference currents i^*_{ds} and i^*_{qs} are calculated using the control strategy as shown in Fig. 3.2. "params" in the figure represents the machine parameters like L_{ds}, L_{qs}, flux ψ_r, base current i_b and number of pole pairs P_p.

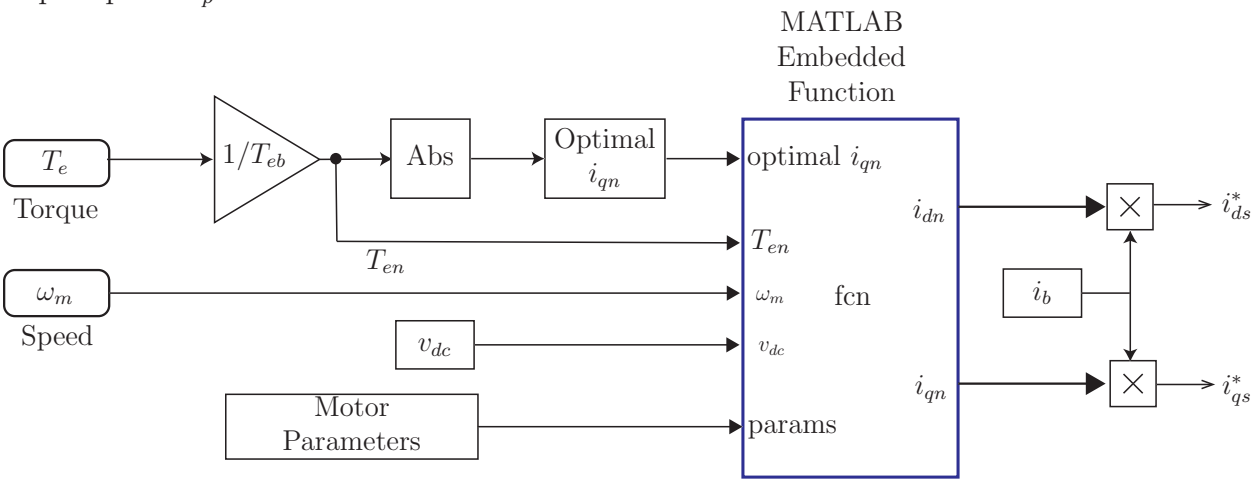

Figure 3.2: Control diagram for normalization approach.

During normal operation, (3.5) is used to determine the d-axis current. This value can be calculated using the speed regulator. But this approach is not applicable to control the machine torque in applications like EVs.

In normal operation, torque and currents are normalized as follow to make them inde-

pendent of parameters. The relation between real and normalized values are given in (3.8).

$$\left.\begin{aligned} T_e &= T_{eb} * T_{en}, \\ i_{qs} &= i_b * i_{qn}, \\ i_{ds} &= i_b * i_{dn}. \end{aligned}\right\} \tag{3.8}$$

Similar to (3.4), torque equation can be written as:

$$T_e = \frac{3}{2} P_p i_{qs} \left(\psi_r + \left(L_{ds} - L_{qs}\right) i_{ds}\right) \tag{3.9}$$

To make the torque equation independent of field and inductance parameters, (3.9) can be re-written as:

$$T_e = \frac{3}{2} P_p i_{qs} \psi_r \left(1 + \frac{\left(L_{ds} - L_{qs}\right) i_{ds}}{\psi_r}\right). \tag{3.10}$$

Since $L_{qs} > L_{ds}$ in IPMSM, (3.10) can be written as below to keep the base values positive.

$$T_e = \frac{3}{2} P_p i_{qs} \psi_r \left(1 + \frac{\left(L_{qs} - L_{ds}\right) i_{ds}}{\psi_r}\right). \tag{3.11}$$

From (3.11), the base current i_b can be written as:

$$i_b = \frac{\psi_r}{\left(L_{qs} - L_{ds}\right)}. \tag{3.12}$$

From (3.11), torque in terms of base current i_b can be modified into:

$$T_e = \frac{3}{2} P_p i_{qs} \psi_r \left(1 - \frac{i_{ds}}{i_b}\right). \tag{3.13}$$

The stator currents i_{ds} and i_{qs} are also normalized such that the torque equation is re-written as:

$$T_e = \frac{3}{2} P_p i_b \psi_r \frac{i_{qs}}{i_b} \left(1 - \frac{i_{ds}}{i_b}\right) \tag{3.14}$$

where, base torque T_{eb} is obtained by:

$$T_{eb} = \frac{3}{2} P_p i_b \psi_r. \tag{3.15}$$

Finally, the normalized torque is represented as:

$$T_{en} = i_{qn} \left(1 - i_{dn}\right). \tag{3.16}$$

The optimal trajectory is calculated as follows since there are infinity solutions for i_{dn} and i_{qn}.

$$I_{sn} = \sqrt{i_{dn}^2 + i_{qn}^2}. \tag{3.17}$$

The current in (3.17) is minimum when (3.16) is differentiated with respect to i_{qn} and is equated to zero. Therefore the normalized torque for minimal currents can be written as,

$$T_{en} = \frac{i_{qn}}{2} \left(\sqrt{4i_{qn}^2 + 1} + 1\right). \tag{3.18}$$

The exact solution for (3.28) in complex, as there are infinity values for i_{qn}. Since normalized values are utilized, a table for i_{qn} values may be computed offline.

Similarly, for overspeed operation the constraint in continuous operation is imposed by the voltage as shown below:

$$\sqrt{v_{ds}^2 + v_{qs}^2} = v_s \tag{3.19}$$

where, $v_s = \frac{v_{dc}}{\frac{\pi}{2}}$.

By combining (3.19) into (3.8), the following polynomial equation is obtained:

$$i_{qn}^4 + x_2 i_{qn}^2 + x_3 i_{qn} + x_4 = 0 \tag{3.20}$$

where,

$$\left.\begin{aligned} x_2 &= \frac{-v_s^2}{P_p^2 i_b^2 L_{qs}^2 \omega_m^2} + \frac{2\psi_r L_{ds}^2 + \psi_r^2}{i_b^2 L_{qs}^2} + \frac{L_{ds}^2}{L_{qs}^2}, \\ x_3 &= \frac{-2\psi_r L_{ds} T_{en}}{i_b^2 L_{qs}^2} - \frac{2L_{ds}^2 . T_{en}}{L_{qs}^2}, \\ x_4 &= \frac{L_{ds}^2 . T_{en}^2}{L_{qs}^2}. \end{aligned}\right\} \tag{3.21}$$

After multiple variable replacement in above equation, solution for i_{qn} is obtained as

$$i_{qn} = \frac{\sqrt{6}}{12} a_3 + \frac{1}{12}\sqrt{-48x_2 - 6a_2 - \frac{288x_4 + 24x_2^2}{a_2} - \frac{72x_3\sqrt{6}}{a_3}} \tag{3.22}$$

where,

$$\left.\begin{aligned} a_1 &= \sqrt{-768x_4^3 + 384x_4^2 x_2^2 - 48x_4 x_2^4 - 432x_4 x_3^2 x_2 + 81x_3^4 + 12x_3^2 x_2^3}, \\ a_2 &= 3\sqrt{-288x_4 x_2 + 108x_3^2 + 8x_2^3 + 12a_1}, \\ a_3 &= \sqrt{-4x_2 + a_2 + \frac{48x_4 + 4x_2^2}{a_2}}. \end{aligned}\right\} \tag{3.23}$$

The Embedded MATLAB Function block has been utilized in the implementation of this equation. To cut down on processing, it might be useful to make a three-dimensional lookup table offline. One drawback is that each time the settings are altered, the table needs to be produced again. It is more versatile to utilize normalized currents and torque, though, as the table becomes value independent. Based on the torque produced, corresponding internal voltage is calculated. If the internal voltage is greater than the source voltage v_s, trajectory is modified using the current in field weakening mode which is shown in (3.21). Else, if the internal voltage is less than the source voltage, current in the normal mode is used to modify the trajectory which is,

$$i_{qn} = \text{Table}\left(T_{en} = \frac{i_{qn}}{2}\left(\sqrt{4i_{qn}^2 + 1} + 1\right)\right). \tag{3.24}$$

3.2.3 Space Vector Modulation

SVM is most commonly used modulation scheme for 2L-VSI control. This is most efficient due to reason like better harmonic performance and enhanced voltage utilization compared to other modulation techniques [56].

Fig. 3.3 depicts a simulation model of SVM with six subsystems. The input variables are the three-phase modulating signals (i.e., v_a^*, v_b^*, and v_c^*) produced by a PI controller, and the output variables are upper-leg switching signals. SVM involves several design steps and complex modeling, thus incurring a high computational burden than sinusoidal PWM. The step-by-step procedure for designing SVM for a 2L-VSI is presented below.

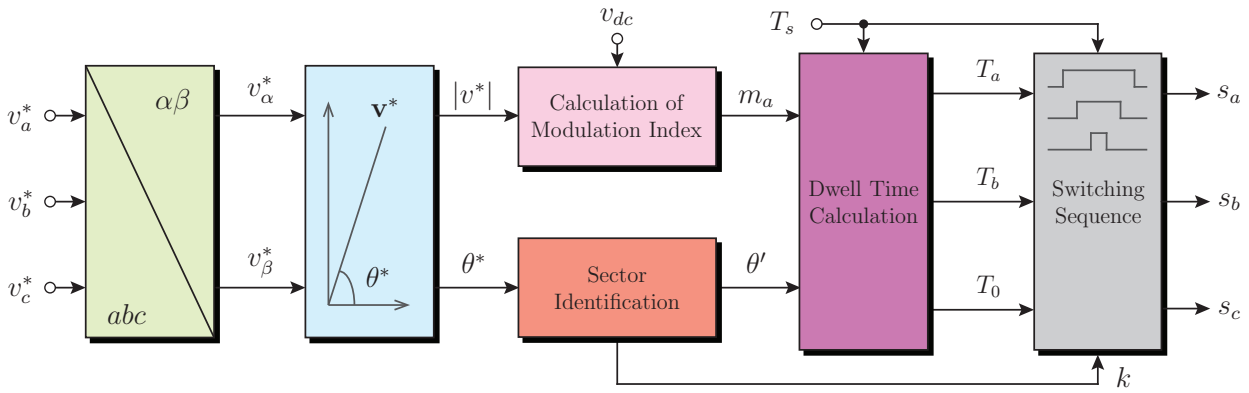

Figure 3.3: Simulation model of SVM for a 2L-VSI.

- **Design Step – 1:** The three-phase instantaneous voltage signals (i.e., v_a^*, v_b^*, v_c^*) are converted into stationary frame modulating signals (i.e., v_α^* and v_β^*) by using the $abc/\alpha\beta$ transformation given in (2.6). The reference voltage vector in $\alpha\beta$-frame is represented as $\mathbf{v}^* = v_\alpha^* + j\, v_\beta^*$.
- **Design Step – 2:** The stationary frame modulating signals are then transformed from

the Cartesian coordinates to the polar coordinates:

$$\mathbf{v}^* = |v^*|\, e^{j\theta^*}, \quad |v^*| = \sqrt{v_\alpha^{*2} + v_\beta^{*2}}, \quad \theta^* = \tan^{-1}\left(\frac{v_\beta^*}{v_\alpha^*}\right)\Bigg\} \tag{3.25}$$

where, $|v^*|$ is the length of the reference vector, and θ^* is the angle between $\mathbf{v}^*$ and α-axis shown in Figure 3.4. $|v^*|$ and θ^* are the peak value and frequency of the converter output voltage, respectively. By controlling the reference vector $\mathbf{v}^*$, the magnitude and frequency of the output voltage waveform are precisely regulated.

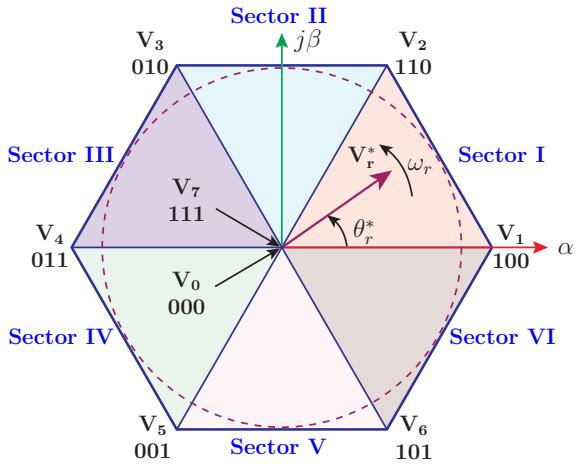

Figure 3.4: Space vector diagram for the 2L-VSI.

- **Design Step – 3:** The modulation index m_a is calculated based on the magnitude of the reference voltage and measured DC-link voltage:

$$m_a = \frac{\sqrt{3}\,|v^*|}{v_{dc}}. \tag{3.26}$$

- **Design Step – 4:** The sector number is computed according to the value of θ^*. The sector number is I when θ^* varies between zero and $\pi/3$ and increases by one when θ^* increases in multiples of $\pi/3$. Fig. 3.4 illustrates a space vector diagram with voltage vectors and sector numbers for a 2L inverter. The six active voltage vectors (i.e., $\mathbf{V_1}$ to

$\mathbf{V_6}$) form a regular hexagon with six equal sectors (i.e., I to VI). The zero voltage vectors $\mathbf{V_0}$ and $\mathbf{V_7}$ lie on the center of the hexagon and do not move in space. The redundant zero voltage vectors are used to minimize the VSI switching frequency or to accomplish other control objectives. The reference vector $\mathbf{v}^*$ rotates in space at an angular speed ω [57]. A modified reference voltage vector angle is also computed in a manner that its value always resides within zero and $\pi/3$, as demonstrated below.

$$\theta' = \theta^* - \frac{\pi}{3}(k-1) \tag{3.27}$$

where, $k = 1, \cdots, 6$ for sectors I to VI, respectively.

- **Design Step – 5:** $\mathbf{v}^*$ is synthesized by three nearby stationary vectors (i.e., two active vectors and one zero vector), based on which the gating signals are generated for the converter. Dwell times define the time duration wherein the reference vector $\mathbf{v}^*$ is switched onto the adjacent vectors during a sampling period T_s. The dwell times for two active vectors (i.e., T_a and T_b) and one zero vector (i.e., T_0) are determined with the following formulas:

$$\left.\begin{aligned} T_a &= T_s\, m_a \sin\left(\frac{\pi}{3} - \theta'\right), \\ T_b &= T_s\, m_a \sin\theta', \\ T_0 &= T_s - T_a - T_b. \end{aligned}\right\} \tag{3.28}$$

- *Design Step – 6:* According to the information about the dwell times, sampling time, and sector number, a switching logic is designed to produce the gating signals for the converter. When $\mathbf{v}^*$ resides in all six sectors. The minimum number of switching is involved in moving from one switching state to the next. The sampling period T_s is divided into seven segments for the selected vectors.

SVM provides better control and harmonic performance than sinusoidal PWM, but at

the expense of complex modeling and design procedures.

3.3 Predictive Current Control

The block diagram of predictive current control strategy or an IPMSM is shown in Fig. 3.5. The PCC method uses the system model to predict the future behavior of the variables to be controlled [56]. The cost function or the error between the reference and predicted value is calculated. The switching state that minimizes the cost function is selected and applied during the next sampling.

The design procedure for synchronous dq-frame PCC strategy is described below. The stator reference currents i_{ds}^* and i_{qs}^* are calculated similar to the MTPA control discussed earlier.

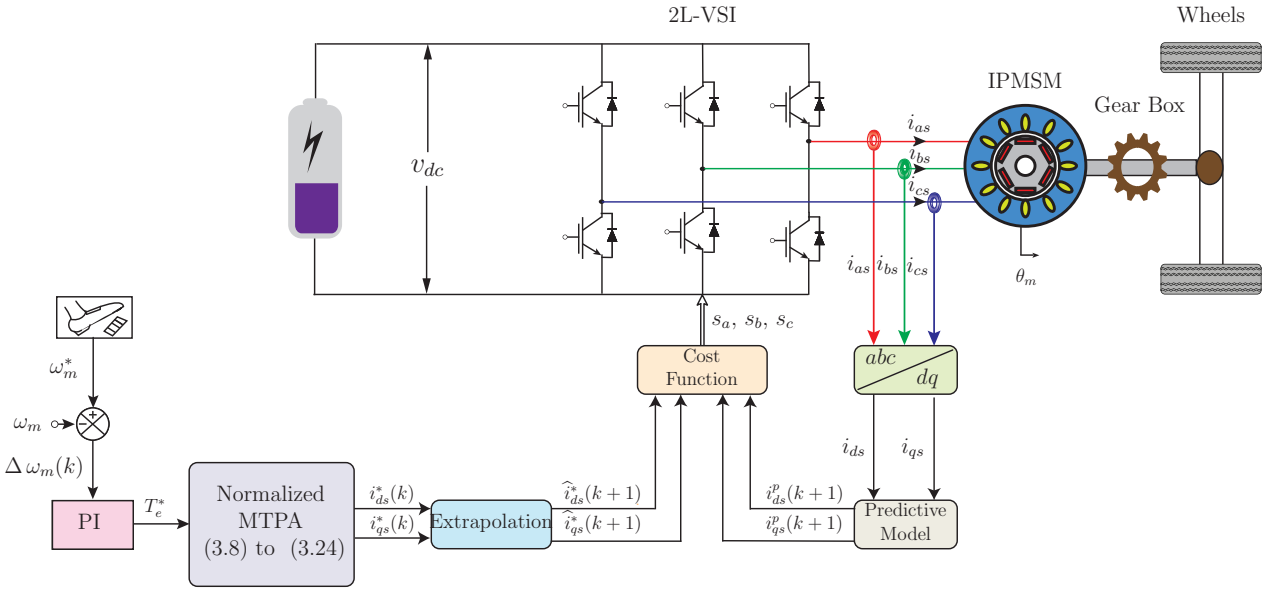

Figure 3.5: Block diagram of the PCC scheme for 2L-VSI in the PMSM-based EV application.

3.3.1 Extrapolation of Reference Currents

Owing to the DC nature of reference dq-axis currents, extrapolation is unnecessary in a steady-state. However, to improve the transient performance, a first-order Lagrange extrapolation can be used with the following representation:

$$\left.\begin{aligned} \widehat{i}^{*}_{ds}(k+1) &= 2\, i^{*}_{ds}(k) - i^{*}_{ds}(k-1), \\ \widehat{i}^{*}_{qs}(k+1) &= 2\, i^{*}_{qs}(k) - i^{*}_{qs}(k-1). \end{aligned}\right\} \tag{3.29}$$

3.3.2 Prediction of Future Behavior of Stator Currents

The future value of the dq-axis currents is assessed by the "predictive model" block, which combines the dq-frame discrete time model of currents with the 2L-VSI model as discussed in previous chapter. The overall sampled data model for the prediction of future values of dq-axis currents is formulated in terms of 2L-VSI switching signals as follows:

$$\begin{bmatrix} i^{p}_{ds}(k+1) \\ i^{p}_{ds}(k+1) \end{bmatrix} = \mathbf{\Phi_s}(k) \begin{bmatrix} i_{ds}(k) \\ i_{ds}(k) \end{bmatrix} + \mathbf{\Gamma_s} \left\{ v_{dc}(k) \begin{bmatrix} s^{p}_{d}(k) \\ s^{p}_{q}(k) \end{bmatrix} \right\} + \mathbf{\Gamma_w}(k) \tag{3.30}$$

where, superscript p denotes the predicted variable.

To minimize the number of online calculations, matrices $\mathbf{\Gamma_s}$, and $\mathbf{\Gamma_w}$ are defined offline. The state matrix $\mathbf{\Phi_s}(k)$ is computed online using the rotor speed $\omega_r(k)$ as input variable.

Fig. 2.4 shows the space vector diagram for a 2L-VSI, where the six active voltage vectors $\mathbf{V_1}$ to $\mathbf{V_6}$, which produce nonzero output voltage, form a regular hexagon with six sectors (I to VI) displaced by 60° in space [58]. The zero-voltage vectors $\mathbf{V_0}$ and $\mathbf{V_7}$ lies at the center of the hexagon. The discrete-time model in (3.30) is used to calculate the future behavior of dq-axis currents in terms of 2L-VSI switching signals. With eight combinations for the switching signals, eight predictions are obtained for dq-frame stator currents.

3.3.3 Cost Function Minimization

The cost function given below is formulated to minimize the error between predicted and extrapolated reference currents:

$$g_r(k) = \left[\widehat{i}^*_{ds}(k+1) - i^p_{ds}(k+1)\right]^2 + \left[\widehat{i}^*_{qs}(k+1) - i^p_{qs}(k+1)\right]^2. \tag{3.31}$$

Eight distinct cost function values ($g_0 \cdots g_7$) are produced by the model in (3.31), which correspond to the eight voltage vectors ($\mathbf{V_0} \cdots \mathbf{V_7}$) in Table 2.2. Finding the lowest cost function value and matching switching state combination is the goal of the cost function minimization subsystem. For instance, the appropriate switching state combination with $s_a = 1$, $s_b = 0$, and $s_c = 0$ is selected as an optimum actuation and applied directly to the 2L-VSI, providing that the cost function g_1 has a minimal value within the pool $g_0 \cdots g_7$. With the traditional PCC technique, the switching frequency becomes variable because there is no modulator. With this PCC method forces the synchronous-frame stator currents to track their respective reference currents during all the operating conditions.

3.3.4 Control Algorithm

The flowchart of the PCC algorithm for 2L-VSI is shown in Fig. 3.6. The method starts with initializing important parameters and then moves on to real-time voltage and current measurements. The algorithm then determines the error between the measured and reference currents and generates a reference current based on the intended values.

After that, a cost function that takes into account different performance standards is assessed. In order to accomplish the required current output, the control flow entails choosing the best voltage vector to minimize the cost function, figuring out which switching signals are suitable for the power electronic devices, and applying these signals. .In order to ensure

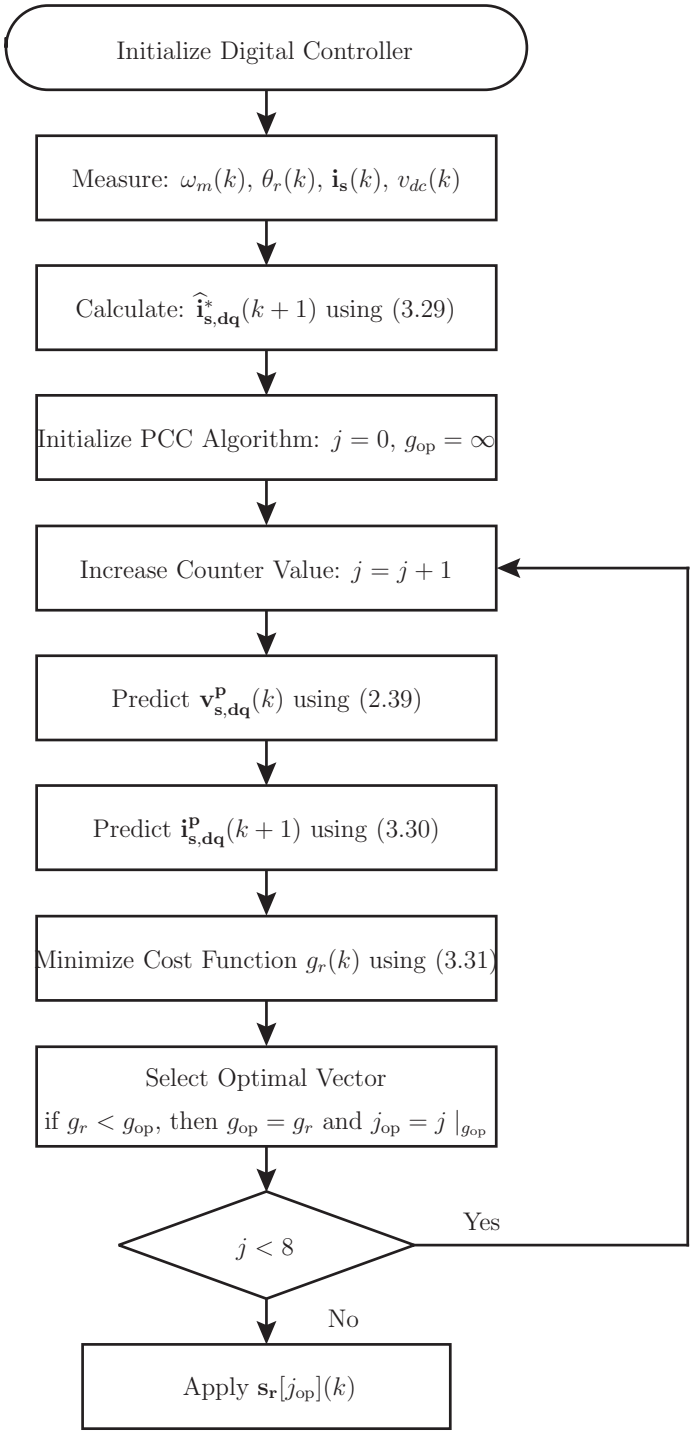

(a)

Figure 3.6: Flowchart of the PCC algorithm for IPMSM with 2L-VSI.

optimal system performance, the algorithm iteratively updates and modifies parameters, guaranteeing ongoing monitoring and dynamic adaptability. An optimal vector j_{op} and the corresponding switching signals that minimize the cost function are selected and directly applied to the 2L-VSI.

3.3.5 Multi-Step Prediction

Iterative, finite-horizon optimization of a plant model serves as the foundation for MPC. A cost-minimizing control strategy is calculated for a comparatively small time horizon in the future, $[k,k+T]$, based on a sample of the present plant state at time k. To be more precise, a cost-minimizing control strategy up to time $k+T$ is found by exploring state trajectories that originate from the present state using an online or real-time computation. The control method is applied just to the first step; after that, the plant state is sampled once again, and the computations are performed from the new current state onward, producing a new control and anticipated state route. Because the prediction horizon is always moving forward, MPC is also known as receding horizon control [59].

When constructing a MPC system, choosing the right temporal horizon is essential. In MPC, the term "time horizon" describes the period of time over which control inputs are optimized and future system behavior is forecast. The trade-off between computational complexity and control performance is strongly influenced by the temporal horizon selection. The factors should be taken into account while choosing the time horizon in MPC includes system dynamics, control objectives, prediction accuracy, constraint handling and sampling time. The time horizon can be classified into two main types: single-step time horizon and multiple-step time horizon. Single-step MPC is computationally less demanding compared to multiple-step MPC as it involves solving a smaller optimization problem. It is frequently used in applications like high speed motion control, automotive applications, HVAC systems

with relatively quick dynamics where longer-term forecast accuracy is not crucial. Similarly, multiple-step MPC makes managing complicated dynamics and restrictions easier and offers a more thorough picture of how the system will evolve in the future. It works well for processes with large time delays, systems with slower dynamics, or applications like chemical and oil-refinery processes where forecast accuracy over a long period of time is crucial. In this thesis, single-step prediction is chosen as shown in (3.30).

3.4 Modulated Model Predictive Current Control

This thesis presents an efficient M^{2}PCC for EV composed of IPMSM connected to 2L-VSI. Fig. 3.7 shows the structure of the proposed M^{2}PCC method for the IPMSM based EV application.

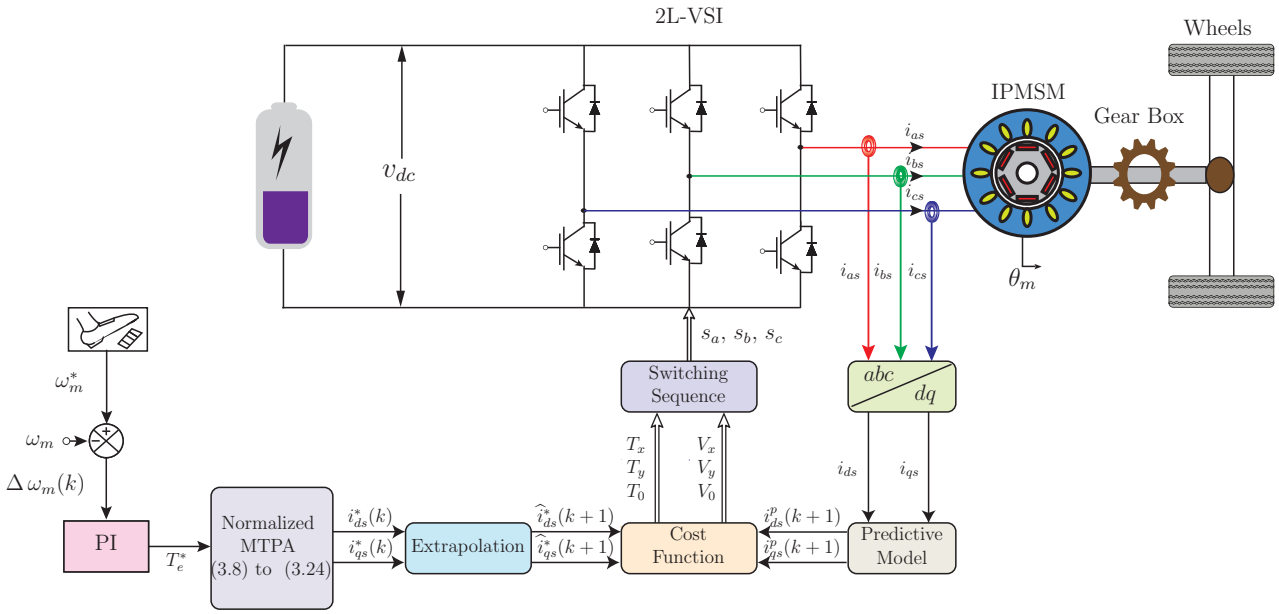

Figure 3.7: Block diagram of the M^{2}PCC scheme for 2L-VSI in the IPMSM-based EV application.

The proposed control method fulfils the control requirements such as improving dynamic response of the IPMSM motor and reduce the torque ripples under variable load conditions.

These objectives are achieved through the regulation of stator currents with fast transient response, smooth steady-state and fixed switching frequency operation simultaneously. The proposed controller predicts the future behavior of the stator currents using MTPA method, synchronous reference frame (dq) and cost function. Finally, the switching sequence is designed by the SVM using synchronous voltage vectors corresponding to the optimal cost function.

The outer control loop provides dq-axis reference currents i_{ds}^{*} and i_{qs}^{*} similar to the MTPA control. The reference dq-axis currents at (k) sampling instant are extrapolated to $(k+1)$ sampling instant similar to (3.29). The discrete-time model in (2.22) is used to predict the future behavior of $i_{ds}^{p}(k+1)$ and $i_{qs}^{p}(k+1)$ for the eight combinations of 2L-VSI switching signals.

3.4.1 Duty Cycles Calculation

For the 2L-VSI, the duty cycles for three stationary voltage vectors are computed as follows [56]:

$$\left.\begin{aligned} d_x &= \frac{g_y\, g_0}{g_x\, g_y + g_x\, g_0 + g_y\, g_0}, \\ d_y &= \frac{g_x\, g_0}{g_x\, g_y + g_x\, g_0 + g_y\, g_0}, \\ d_0 &= \frac{g_x\, g_y}{g_x\, g_y + g_x\, g_0 + g_y\, g_0}. \end{aligned}\right\} \tag{3.32}$$

The time durations for the vectors $\mathbf{V_x}$, $\mathbf{V_y}$ and $\mathbf{V_0}$ are calculated by,

$$\left.\begin{aligned} T_x &= d_x\, T_c, \\ T_y &= d_y\, T_c, \\ T_0 &= d_0\, T_c. \end{aligned}\right\} \tag{3.33}$$

In PCC method, the space vector diagram is divided into eight switching states for 2L-VSI. But, in proposed M^{2}PCC method, the space vector diagram is divided into six vectors

as shown in Fig. 3.4. In this method, the reference voltage vector that lies in optimal sector is computed by using 8 functional values. The active and zero vectors $\mathbf{V_x}$, $\mathbf{V_y}$ and $\mathbf{V_0}$ corresponding to the optimal sector are chosen in each sampling period to accomplish fixed switching frequency for 2L-VSI. The cost functions corresponding to the voltage vectors $\mathbf{V_x}$, $\mathbf{V_y}$ and $\mathbf{V_0}$ are defined by g_x, g_y and g_0, respectively.

For example, in sector I, g_x, g_y and g_0 are calculated for voltage vectors $\mathbf{V_x}$ (s_a, s_b, s_c = 100), $\mathbf{V_y}$ (110) and $\mathbf{V_0}$ (000), respectively. The Fig. 3.8 highlights synthesis of reference vector $\mathbf{V}^*$ from the adjacent stationary vectors in sector I.

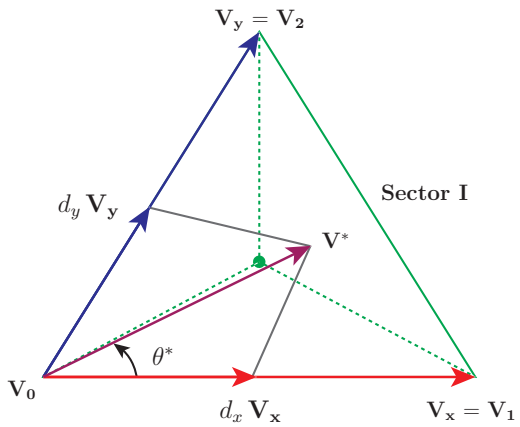

Figure 3.8: Synthesis of reference vector $\mathbf{V}^*$ from the adjacent stationary vectors for sector I.

Similarly, the duty cycles and time durations for each sector is calculated as shown in Table 3.1 using (3.32) and (3.33).

3.4.2 Optimized Cost Function

A new cost function is formulated below to compute the average reference current tracking error of the motor currents for each of the six sectors of 2L-VSI:

$$J(k) = d_x\, g_x + d_y\, g_y + d_0\, g_0. \tag{3.34}$$

Table 3.1: Summary of voltage vectors, duty cycles and time durations for each sector

Sector Number	Voltage Vector			Duty Cycles			Time Durations		
s	$\mathbf{V_x}$	$\mathbf{V_y}$	$\mathbf{V_0}$	d_x	d_y	d_0	T_x	T_y	T_0
I	$\mathbf{V_1}$	$\mathbf{V_2}$	$\mathbf{V_0}$	d_1	d_2	d_0	T_1	T_2	T_0
II	$\mathbf{V_3}$	$\mathbf{V_2}$	$\mathbf{V_0}$	d_3	d_2	d_0	T_3	T_2	T_0
III	$\mathbf{V_3}$	$\mathbf{V_4}$	$\mathbf{V_0}$	d_3	d_4	d_0	T_3	T_4	T_0
IV	$\mathbf{V_5}$	$\mathbf{V_4}$	$\mathbf{V_0}$	d_5	d_4	d_0	T_5	T_4	T_0
V	$\mathbf{V_5}$	$\mathbf{V_6}$	$\mathbf{V_0}$	d_5	d_6	d_0	T_5	T_6	T_0
VI	$\mathbf{V_1}$	$\mathbf{V_6}$	$\mathbf{V_0}$	d_1	d_6	d_0	T_1	T_6	T_0

Finally, the two active and a zero voltage vectors corresponding to the minimum cost value are synthesized by the modulation stage consisting of seven-segment switching sequence shown in Fig. 3.9, to produce switching signals for the 2L-VSI in the next sampling period. It should be noted that the classical SVM also uses seven-segment switching sequence to obtain fixed switching frequency. In contrast to the classical PCC method which applies a single voltage vector during entire sampling period, the proposed M^{2}PCC method applies more than one voltage vector to the 2L-VSI, leading to low current ripple. The switching frequency (f_{sw}) of the devices is equal to the carrier waveform frequency (=$1/T_c$ [57]).

3.4.3 Control Algorithm

The flowchart of the M^{2}PCC algorithm for 2L-VSI is shown in Fig. 3.10. After initializing the digital controller and calculating the reference stator currents, the PCC algorithm enters an iterative loop where the stator currents are predicted, and cost function values are calculated. Stored cost function values are used to calculate the duty cycles. An optimal vector i_{op} and the corresponding switching signals that minimize the new cost function are selected and directly applied to the VSI.

In summary, M^{2}PCC combines the principles of Model Predictive Control with mod-

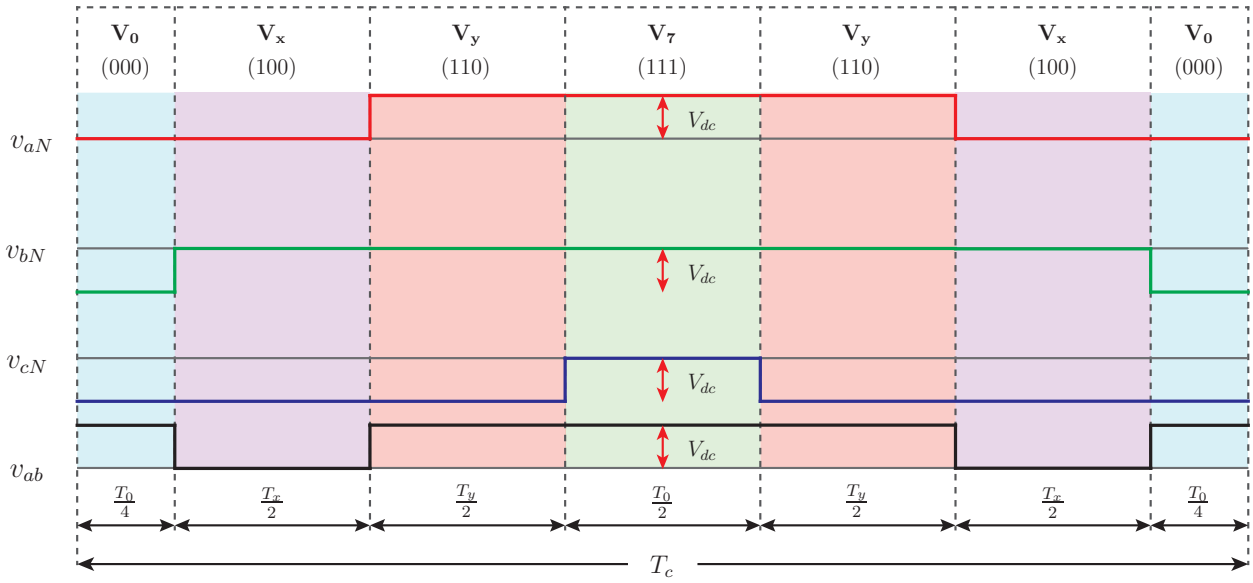

Figure 3.9: Symmetrically aligned n-type switching sequence in sector I.

ulation techniques to achieve precise and dynamic current regulation in power electronic systems. The flowchart represents a continuous feedback loop that iteratively adjusts the control inputs based on the measured and reference currents.

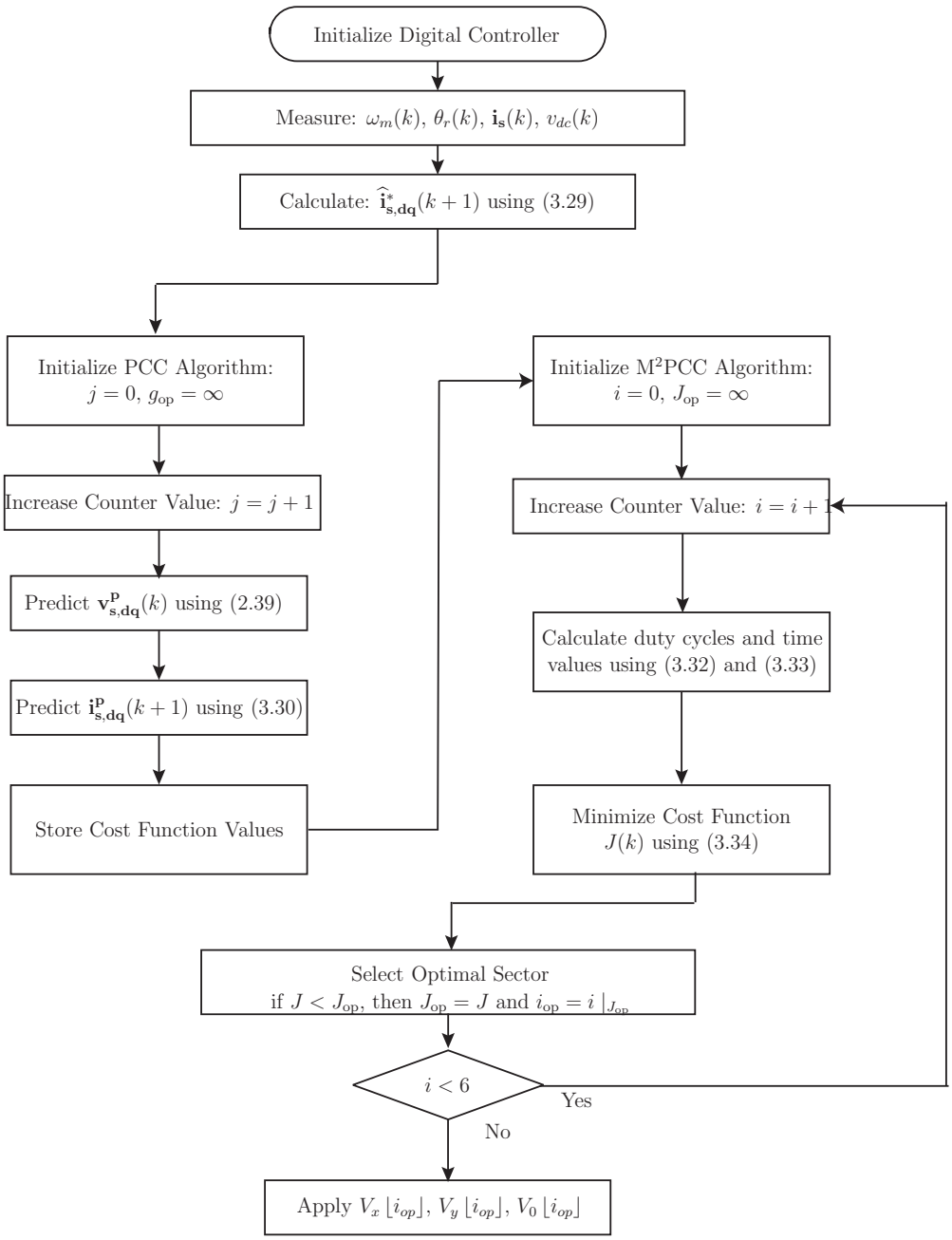

Figure 3.10: Flowchart of the M^{2}PCC algorithm for IPMSM with 2L-VSI.

CHAPTER 4

Simulation Results and Analysis

In this section, MATLAB simulations are conducted on classical PCC and proposed M^{2}PCC methods using the parameters in Table 4.1. The system performance during transient and steady-state conditions are presented in addition to the harmonic analysis.

Table 4.1: Parameters of the EV

Description	Variable	SI Value
Output power	P_s	205 kW
Rotor speed	N_m	4275 rpm
Frequency	F_s	213.75 Hz
Rated torque	T_m	429.765 N.m
No. of pole pairs	P_P	3
Rated line-line voltage	V_{LL}	164.164 V
Stator winding resistance	R_s	4.75 mΩ
d-axis inductance	L_{ds}	66.479 μF
q-axis inductance	L_{qs}	119.38 μF
Battery voltage	V_{bat}	350 V
Battery current	A_{bat}	230 Ah

4.1 Definitions of Performance Assessment Parameters

To assess the performance of different control schemes, the following parameters are defined by using the guidelines in [57].

Harmonics in EVs typically refer to harmonic distortions in the electric power supply,

which can affect the performance of electric motors and other power electronics. Harmonics are deviations from the fundamental frequency (usually 60 Hz or 50 Hz in power systems) and are often caused by non-linear loads, such as power electronic devices like inverters. Harmonics can impact motor performance in EVs by motor heating, voltage distortion, torque ripple, increase losses and electromagnetic interference. Total Harmonic Distortion (THD) and Weighted Total Harmonic Distortion (WTHD) are metrics used to quantify the distortion present in a waveform, typically in the context of electrical power systems.

THD is a measure of the harmonic content in a signal compared to the fundamental frequency. It is expressed as a percentage and can be written as,

$$\%\text{THD}_{is} = \frac{1}{3} \sum_{x=a,b,c} \frac{\sqrt{i_{2,x}^2 + i_{3,x}^2 + ... + i_{n,x}^2}}{i_{1,x}} \times 100 \tag{4.1}$$

where, $i_{n,x}$ and $i_{1,x}$ are the n^{th} order harmonic and fundamental components of phase-x measured currents, respectively.

WTHD is a variation of THD that assigns different weights to individual harmonics based on their importance in the system. This is often done to better represent the impact of certain harmonics on the overall system performance. It is also expressed as a percentage and can be written as,

$$\%\text{WTHD}_{is} = \frac{1}{3} \sum_{x=a,b,c} \frac{\sqrt{(w_2\, i_{2,x})^2 + (w_3\, i_{3,x})^2 + ... + (w_n\, i_{n,x})^2}}{i_{1,x}} \times 100 \tag{4.2}$$

where, w_2, w_3 and w_n are the weights assigned to each harmonic component.

The percentage mean absolute current reference tracking error ($\%\, e_{is}$) is defined as an absolute difference between the reference and measured current for m number of samples

with respect to the *rms* value of reference current:

$$\%\, e_{i_x} = \frac{\frac{1}{m}\sum_{k=0}^{m} |i_x^*(k) - i_x(k)|}{I_x^*} \times 100, \qquad x \in \{a,\, b,\, c\} \tag{4.3}$$

where, m represents the number of samples.

For three-phase currents, overall tracking error is computed as an average of tracking error in each phase, that is,

$$\%\, e_{is} = \frac{\%\, e_{ia} + \%\, e_{ib} + \%\, e_{ic}}{3}. \tag{4.4}$$

The switching frequency (f_{sw}) is calculated based on the number of cycles considered for the harmonic analysis. In this case 15 cycles in the simulation is considered for the harmonic analysis. The average device switching frequency obtained by the PCC scheme can be computed by measuring the cumulative number of switch changes and by dividing them with respect to the time period T considered for the measurement of switch changes. This approach is demonstrated for a two-level converter as follows:

$$f_{sw} = \frac{f_{sw,a} + f_{sw,b} + f_{sw,c}}{3} = \frac{n_{sw,a} + n_{sw,b} + n_{sw,c}}{3\,T} \tag{4.5}$$

where, $f_{sw,a}$, $f_{sw,b}$, and $f_{sw,c}$ are the switching frequencies of semiconductor devices in phase-a, -b, and -c, respectively. $n_{sw,a}$, $n_{sw,b}$, and $n_{sw,c}$ are number of switch changes in phase-a, -b, and -c, respectively.

4.2 Simulation Results for Classical Predictive Current Control

Transient performance of the motor at rated speed with step changes in torque is analyzed in this section. The simulation results for speed, torque, stator currents in natural (abc) and

synchronous (dq) reference frames are presented. The PCC method operates with T_s = 38 μs.

4.2.1 Transient Response

The dynamic performance of IPMSM is shown in Fig. 4.1. The overall performance of the motor from 0 to 2.5 seconds with multiple step changes in torque can be seen. For each step change in the torque, other parameters like speed, currents are changing. The detailed study on the performance of the motor for each step change is investigated in this section.

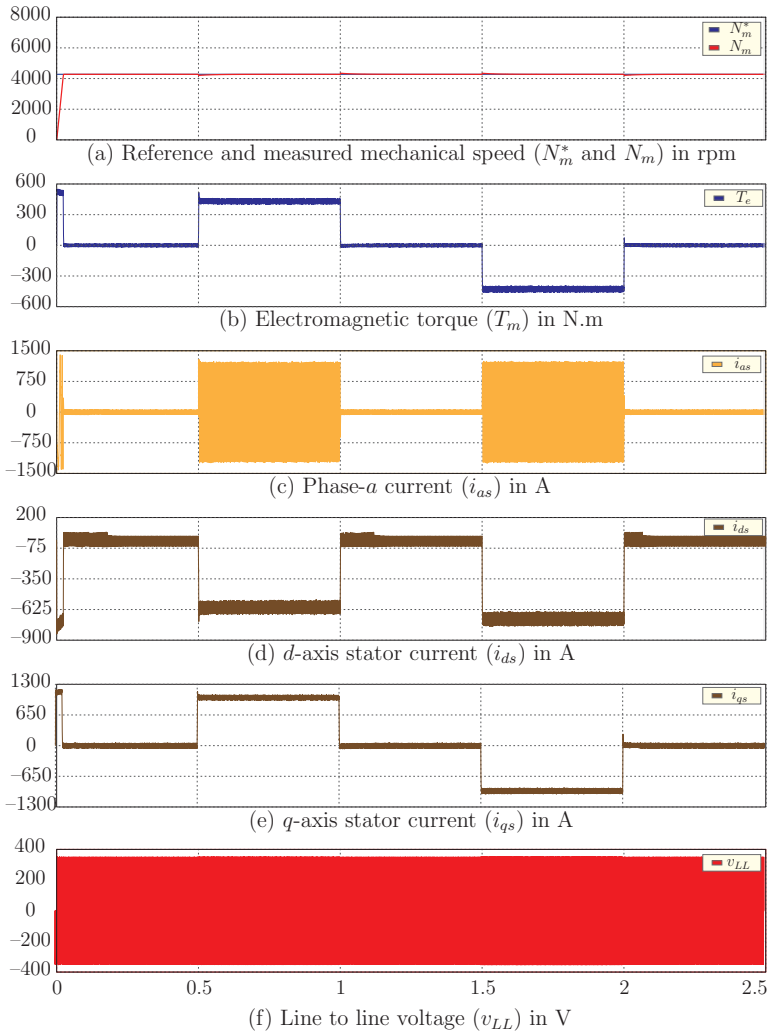

(a) Reference and measured mechanical speed (N_m^* and N_m) in rpm

(b) Electromagnetic torque (T_m) in N.m

(c) Phase-a current (i_{as}) in A

(d) d-axis stator current (i_{ds}) in A

(e) q-axis stator current (i_{qs}) in A

(f) Line to line voltage (v_{LL}) in V

Figure 4.1: Transient response for PCC method during step changes in load torque.

Case 1 : Step Change from 0 to T_m

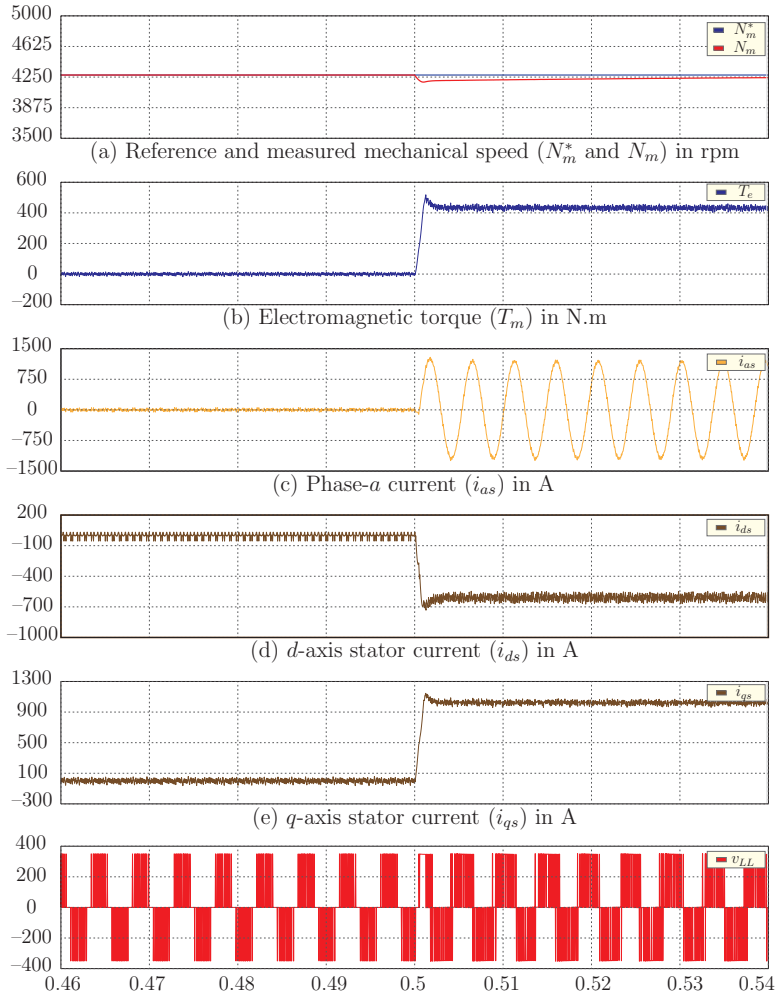

(a) Reference and measured mechanical speed (N_m^* and N_m) in rpm

(b) Electromagnetic torque (T_m) in N.m

(c) Phase-a current (i_{as}) in A

(d) d-axis stator current (i_{ds}) in A

(e) q-axis stator current (i_{qs}) in A

(f) Line to line voltage (v_{LL}) in V

Figure 4.2: Transient response for PCC method during step change from 0 to T_m.

In this case, the step change from 0 to rated torque T_m is analyzed. The resultant waveform for the step change from 0 to rated torque T_m is shown in Fig. 4.2. The rated torque is changes from 0 to T_m at 0.5 seconds. With the step change in the torque, there is a slight change in the speed and come back to its rated value in 0.03 seconds at 0.53 seconds. Also, d-axis current is decreased and q-axis current is increased linearly with the torque as shown in Fig. 4.2. d-axis current has come down to –600 A whereas it was –120 A before the step change, the respective fall time for this step is around 0.005 seconds. q-axis

current magnitude is –110 A and 80 A before and after the step change, respectively. The magnitudes of *abc* varied from –1200 to 1200 A. The magnitudes of line-line voltages remains same voltage of 300 V but with a small spike in the waveform at step change.

Case 2 : Step Change from T_m to 0

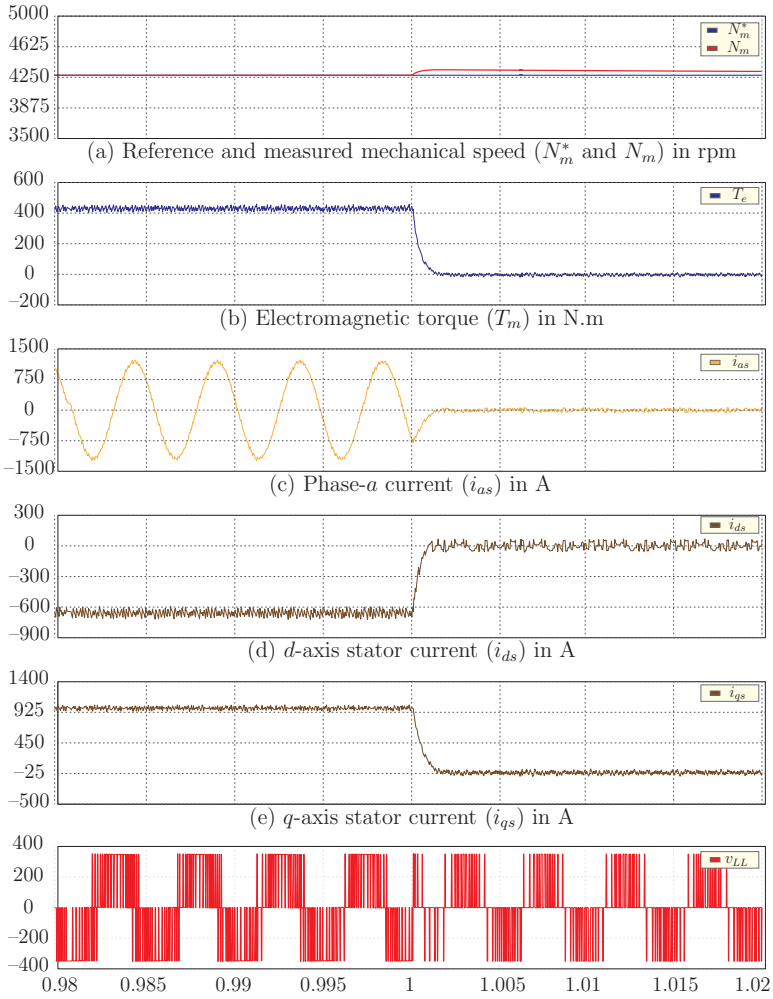

(a) Reference and measured mechanical speed (N_m^* and N_m) in rpm

(b) Electromagnetic torque (T_m) in N.m

(c) Phase-a current (i_{as}) in A

(d) d-axis stator current (i_{ds}) in A

(e) q-axis stator current (i_{qs}) in A

(f) Line to line voltage (v_{LL}) in V

Figure 4.3: Transient response for PCC method during step change from T_m to 0.

The simulation result for this case is shown in Fig. 4.3. In this case, the torque of the motor is decreased back to 0 from its rated value at 1 second. As a result, d-axis current increased from –700 A to 0, and q-axis current is increased to 0 from 930 A. During this

change, we can see the actual speed is not exactly following the reference speed. But after 0.05 seconds, speed came to its rated value. The magnitudes of I_{abc} currents and line-line voltage remain constant at 1100 A and 300 V respectively . d-axis has come to zero after 0.002 seconds.

Case 3 : Step Change from 0 to $-T_m$

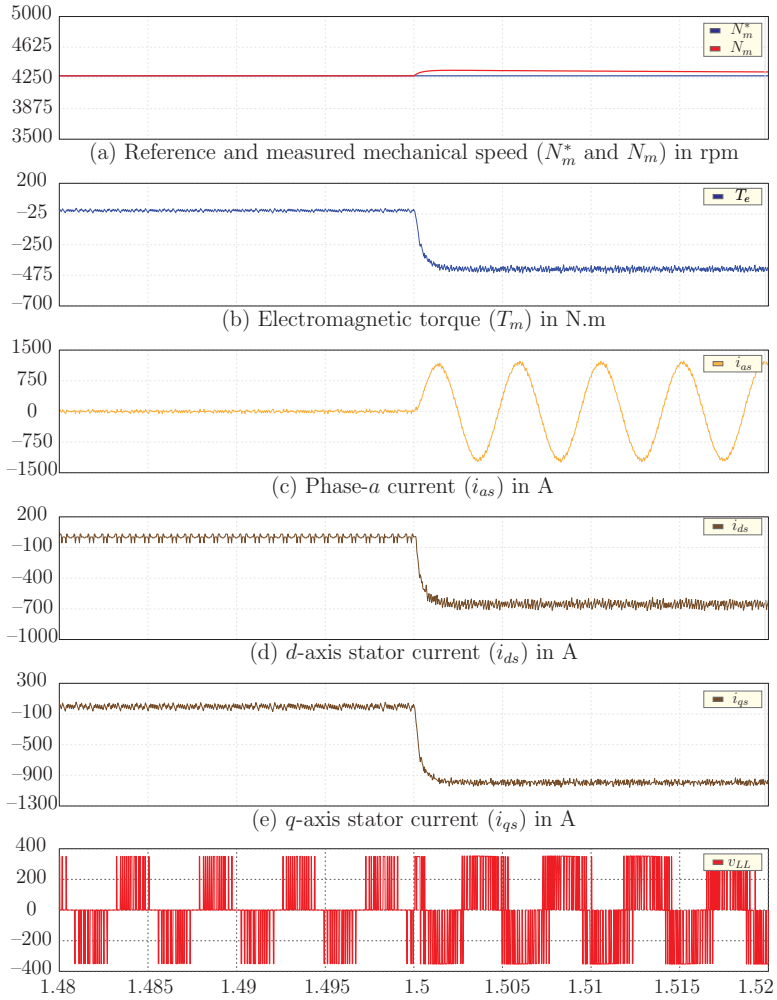

(a) Reference and measured mechanical speed (N_m^* and N_m) in rpm

(b) Electromagnetic torque (T_m) in N.m

(c) Phase-a current (i_{as}) in A

(d) d-axis stator current (i_{ds}) in A

(e) q-axis stator current (i_{qs}) in A

(f) Line to line voltage (v_{LL}) in V

Figure 4.4: Transient response for PCC method during step change from 0 to $-T_m$.

In this case with classical PCC, the torque is further decreased to negative T_m at 1.5 seconds. By decreasing the torque to negative, both dq-axis currents decreases as shown

in Fig. 4.4. With negative change in the rated torque at 1.5 seconds, the speed has some distortion and came back to the rated value in 0.02 seconds. Similarly, dq-axis currents reached –650 A and –1000 A respectively from zero.

Case 4 : Step Change from $-T_m$ to 0

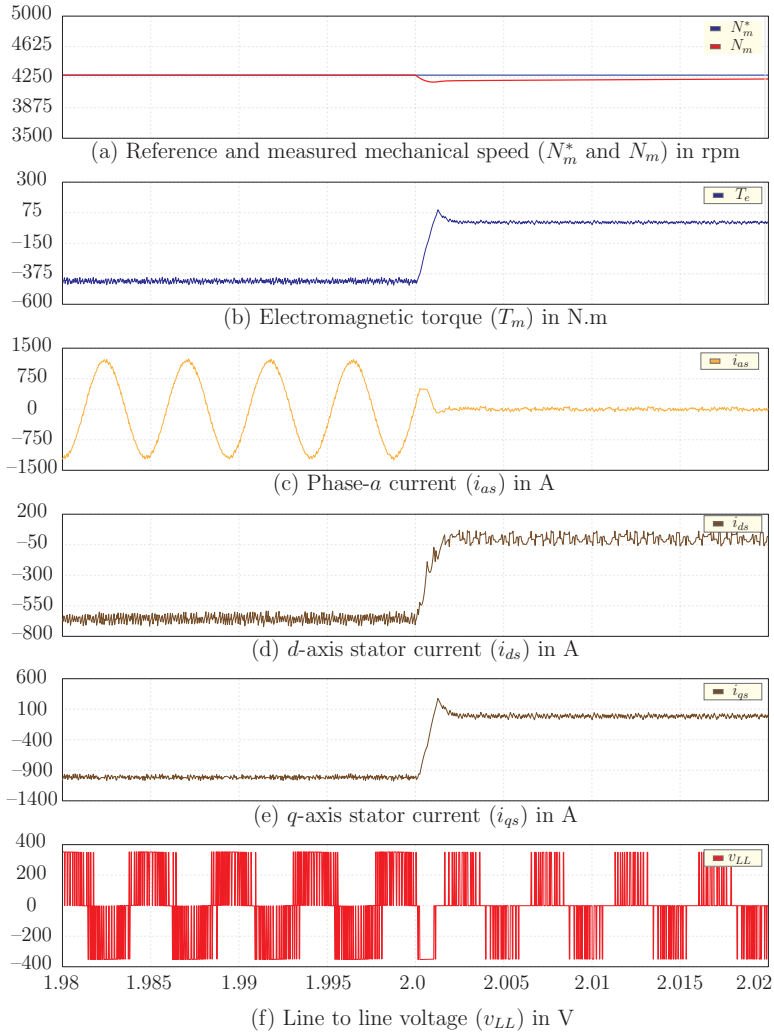

(a) Reference and measured mechanical speed (N_m^* and N_m) in rpm

(b) Electromagnetic torque (T_m) in N.m

(c) Phase-a current (i_{as}) in A

(d) d-axis stator current (i_{ds}) in A

(e) q-axis stator current (i_{qs}) in A

(f) Line to line voltage (v_{LL}) in V

Figure 4.5: Transient response for PCC method during step change from $-T_m$ to 0.

The last step change of the transient state is to change the torque back to 0 from $-T_m$. In this case with classical PCC, both dq-axis currents are increased when compared to case 3. The simulation results are shown in Fig. 4.5. This step change is applying at 2 seconds.

With positive change in the torque all other parameters reach to zero with minute distortions in speed at the step change.

4.2.2 Steady-State Response

The next case is to verify the steady-state (SS) performance of PMSM based EV by varying the torque of the motor with classical PCC. The rated torque has been changed to positive and negative value by running the motor at rated speed.

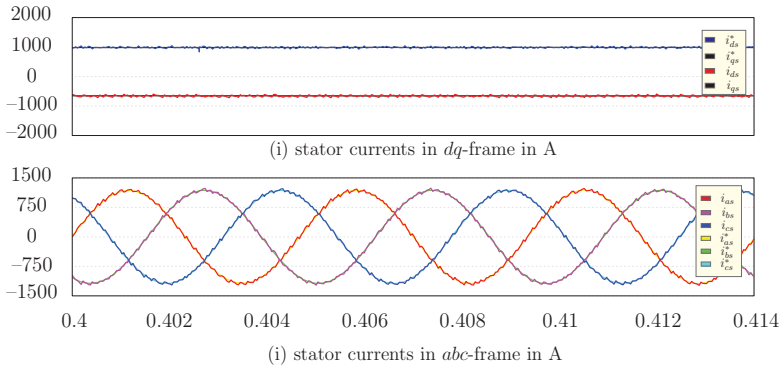

Figure 4.6: Steady state response for PCC with positive load torque.

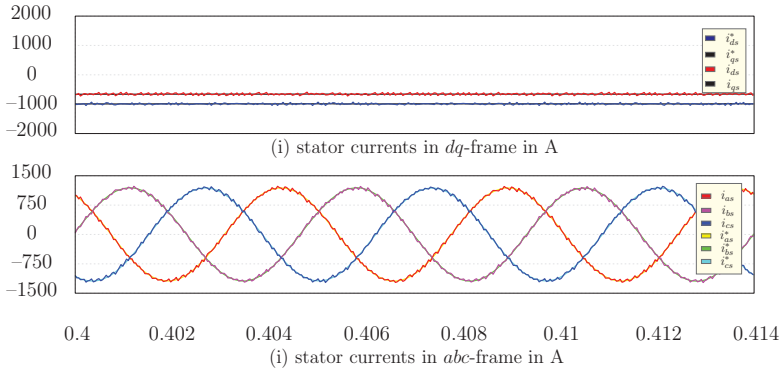

Figure 4.7: Steady state response for PCC with negative load torque.

Steady state responses for both positive and negative values of the rated torque are shown in Fig. 4.6 and Fig. 4.7 respectively. During the positive torque, the magnitudes of dq-axis currents are following the reference currents calculated by MTPA block. Three-phase

currents are also observed during this steady state condition.

During the negative torque, q-axis current remains same at –900 A. But the d-axis current decreased to –1000 A from –100 A. The magnitudes of abc currents remains same with 180 degrees phase shift as shown in Fig. 4.7.

4.2.3 Harmonic Analysis

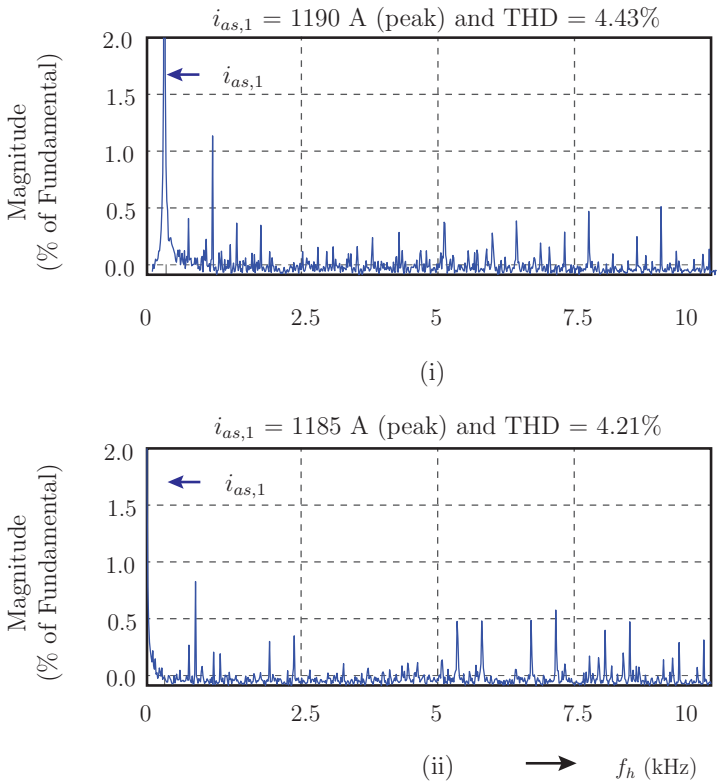

Figure 4.8: FFT analysis during rated speed condition for PCC method: (i) at positive torque (SS1) and (ii) at negative torque (SS2).

Fig. 4.8 shows the Fast Fourier Transform (FFT) analysis on phase-a current during rated speed rated torque conditions with the classical predictive control method. With the classical PCC method, spread spectrum of current harmonics is noticed with average f_{sw} = 4417 Hz and f_{sw} = 4688 Hz with positive and negative rated torque respectively . With the classical PCC method, spread spectrum of generator and grid current harmonics is noticed, which increases the harmonic filter design complexity. The harmonic components can be

observed in detail by zooming the high-resolution FFT plots. THD for both positive torque and negative torque is calculated as 4.43% and 4.21% respectively. The peak currents are observed as 1191 A and 1184 A.

4.3 Simulation Results for Modulated Model Predictive Current Control

Transient performance of the motor at rated speed with step changes in torque is analyzed in this thesis. The simulation results for speed, torque, stator currents in natural (abc) and synchronous (dq) reference frames.

4.3.1 Transient Response

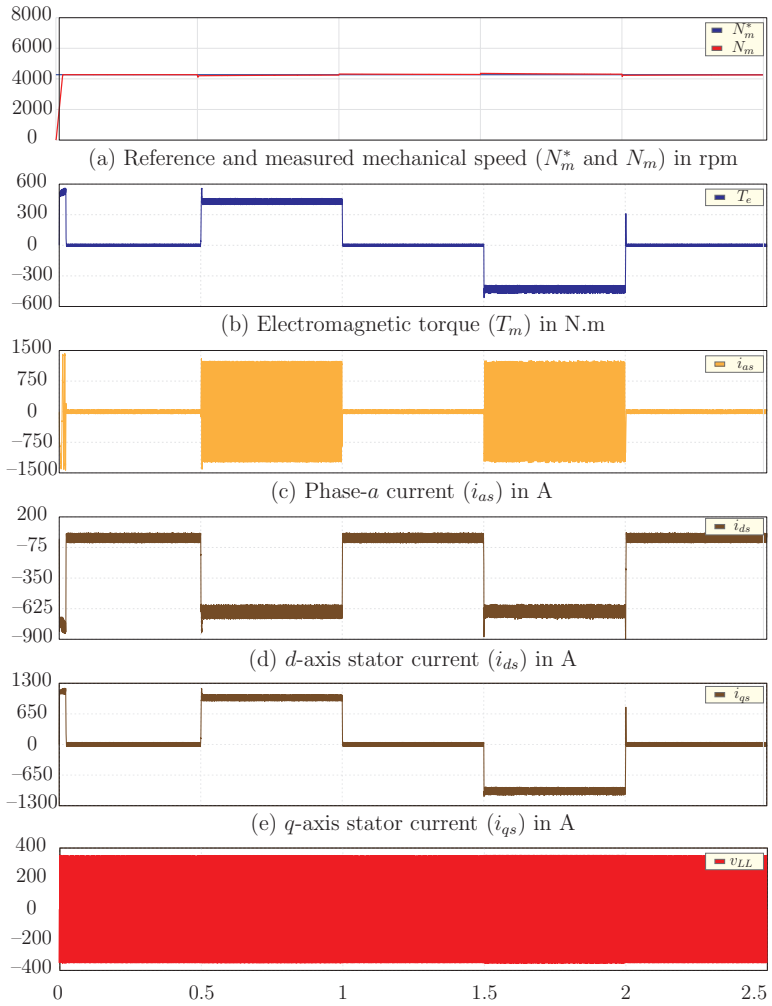

(a) Reference and measured mechanical speed (N_m^* and N_m) in rpm

(b) Electromagnetic torque (T_m) in N.m

(c) Phase-a current (i_{as}) in A

(d) d-axis stator current (i_{ds}) in A

(e) q-axis stator current (i_{qs}) in A

(f) Line to line voltage (v_{LL}) in V

Figure 4.9: Transient response for M^{2}PCC method during step changes in load torque.

The proposed M^{2}PCC method operates with $T_s = 100$ μs. The dynamic performance of

IPMSM is shown in Fig. 4.9. With the same step changes investigated for PCC, M^{2}PCC performance is also verified. The transient responses of M^{2}PCC scheme looks similar to that of PCC with little distortions.

Case 1 : Step Change from 0 to T_m

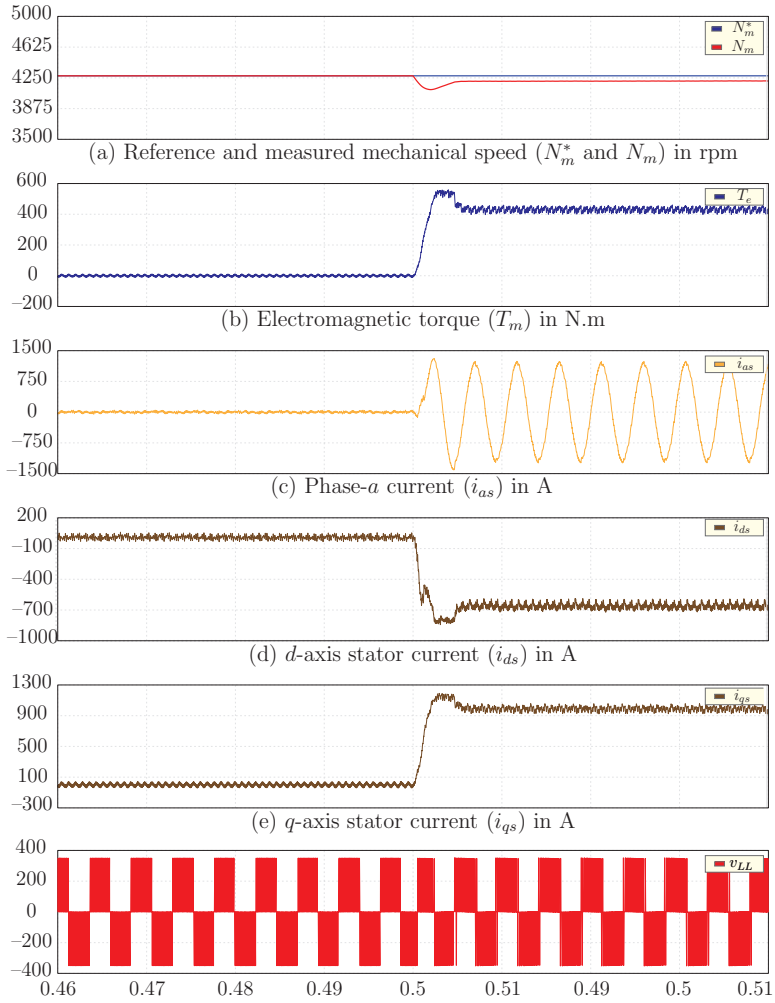

(a) Reference and measured mechanical speed (N_m^* and N_m) in rpm

(b) Electromagnetic torque (T_m) in N.m

(c) Phase-a current (i_{as}) in A

(d) d-axis stator current (i_{ds}) in A

(e) q-axis stator current (i_{qs}) in A

(f) Line to line voltage (v_{LL}) in V

Figure 4.10: Transient response for M^{2}PCC method during step change from 0 to T_m.

In this case, the first step change from 0 to rated torque T_m is analyzed. The results for the first step change in torque is shown in Fig. 4.10. With positive step change in the torque, there is a slight change in the speed. As a result, d-axis current is decreasing and

q-axis current is increasing. It takes 0.005 seconds to all the parameters to maintain constant value after the change at 0.5 seconds. For this step change, the magnitude of d-axis currents varies from 0 to –700 A. Similarly, q-axis currents varies from 0 to 800 A. Magnitudes of abc currents and v_{LL} voltages remains same as in PCC.

Case 2 : Step Change from T_m to 0

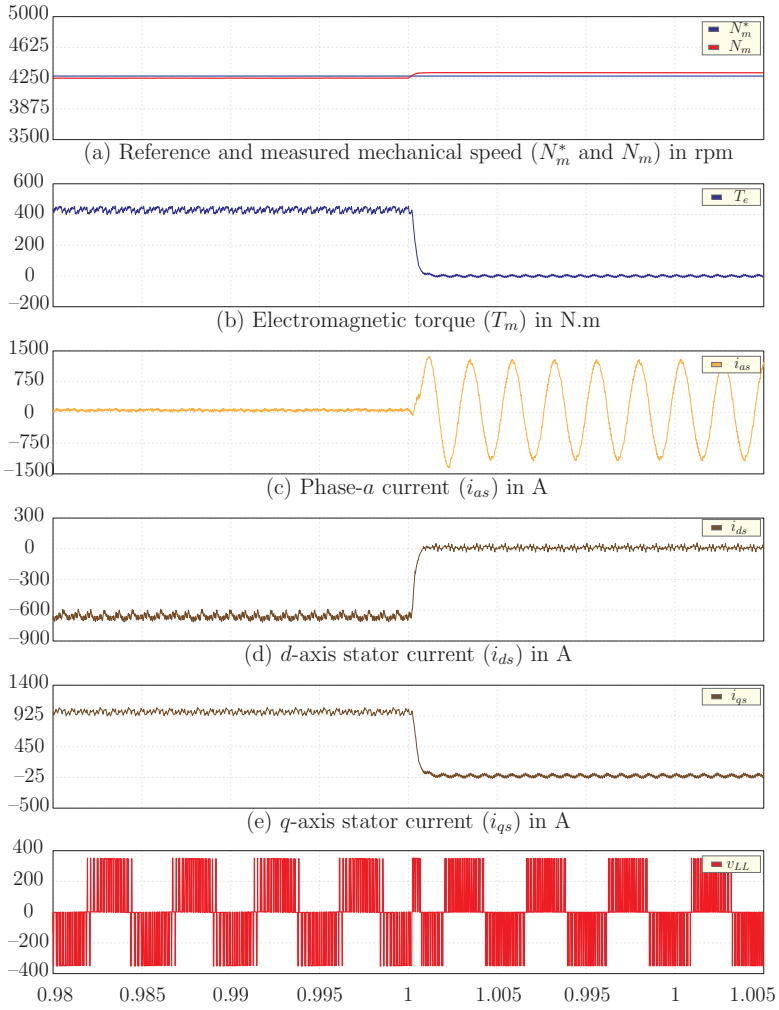

(a) Reference and measured mechanical speed (N_m^* and N_m) in rpm

(b) Electromagnetic torque (T_m) in N.m

(c) Phase-a current (i_{as}) in A

(d) d-axis stator current (i_{ds}) in A

(e) q-axis stator current (i_{qs}) in A

(f) Line to line voltage (v_{LL}) in V

Figure 4.11: Transient response for M^{2}PCC method during step change from T_m to 0.

In the proposed M^{2}PCC , the torque of the motor is changed back to 0 by which d-axis current increases and q-axis current is increased as shown in Fig. 4.11. When the torque gets

back to 0 from rated torque, all other parameters become zero from their initial values.

Case 3 : Step Change from 0 to $-T_m$

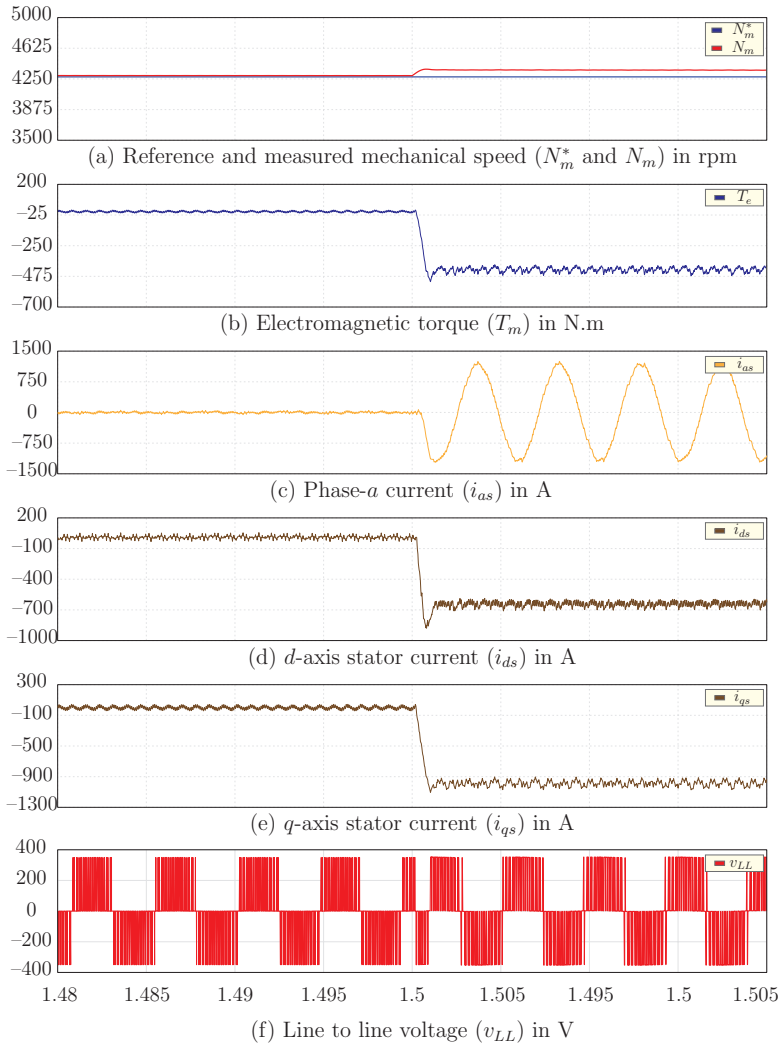

(a) Reference and measured mechanical speed (N_m^* and N_m) in rpm

(b) Electromagnetic torque (T_m) in N.m

(c) Phase-a current (i_{as}) in A

(d) d-axis stator current (i_{ds}) in A

(e) q-axis stator current (i_{qs}) in A

(f) Line to line voltage (v_{LL}) in V

Figure 4.12: Transient response for M^{2}PCC method during step change from 0 to $-T_m$.

Similar to classical PCC, both dq-axis currents decreases with decrease of torque from 0 to $-T_m$ as shown in Fig. 4.12. With negative change is torque, all other parameters become negative. But time taken to change the values is less compared to the PCC. dq-axis currents become –600 A and –1000 A respectively.

Case 4 : Step Change from $-T_m$ to 0

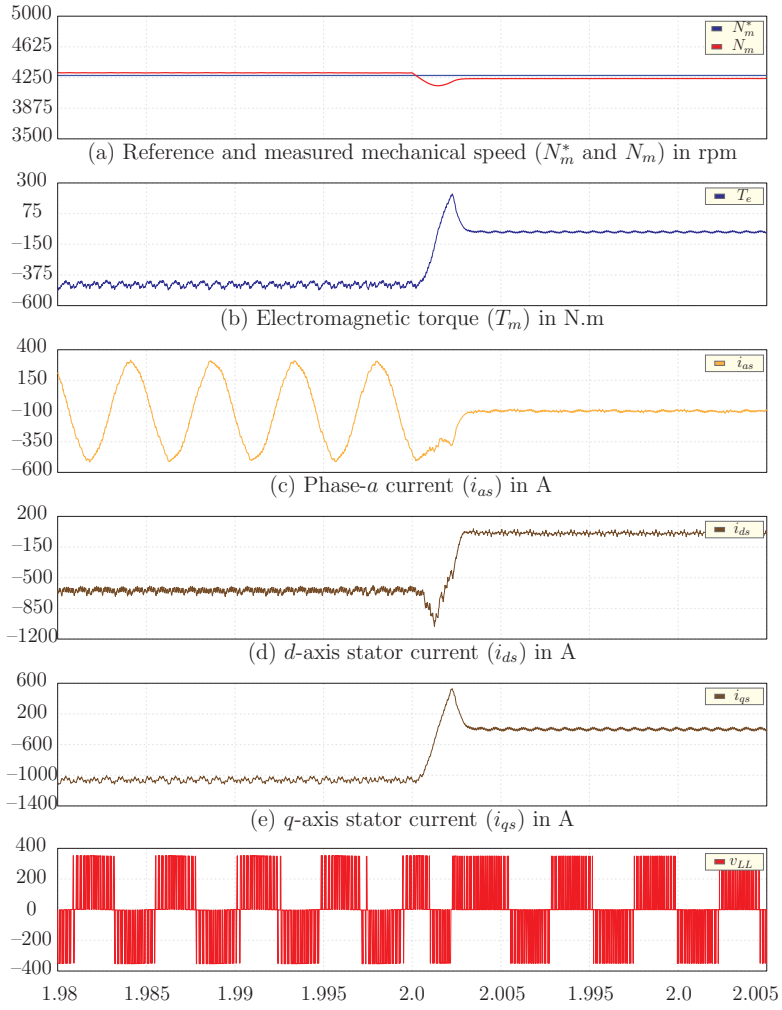

(a) Reference and measured mechanical speed (N_m^* and N_m) in rpm

(b) Electromagnetic torque (T_m) in N.m

(c) Phase-a current (i_{as}) in A

(d) d-axis stator current (i_{ds}) in A

(e) q-axis stator current (i_{qs}) in A

(f) Line to line voltage (v_{LL}) in V

Figure 4.13: Transient response for M^{2}PCC method during step change from $-T_m$ to 0.

In the proposed M^{2}PCC method, with step change of torque from $-T_m$, the dq-axis currents are increased similar to that of PCC. Simulation results for this case is shown in Fig. 4.13. When torque become from its negative rated value, all other parameters again get back to 0.

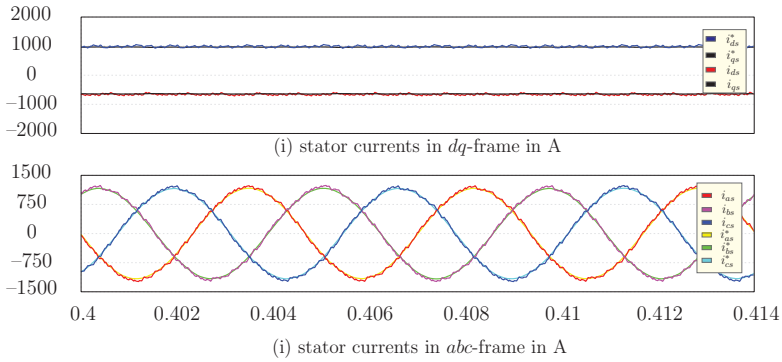

Figure 4.14: Steady state response for M^{2}PCC with positive load torque.

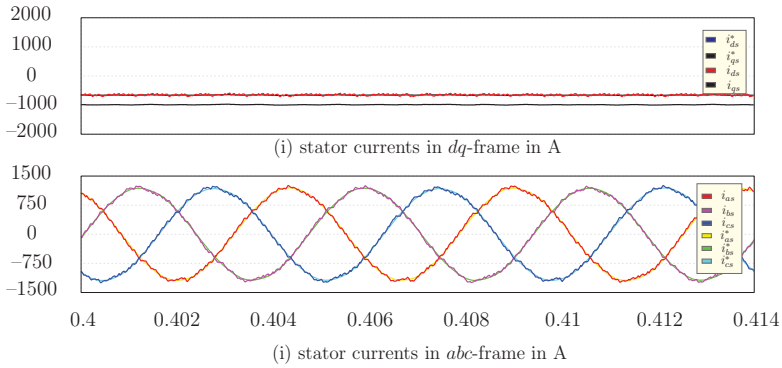

Figure 4.15: Steady state response for M^{2}PCC with negative load torque.

4.3.2 Steady-State Response

The next case is to verify the steady state performance of PMSM based EV by varying the torque of the motor with proposed M^{2}PCC. The rated torque has been changed to positive and negative value by running the motor at rated speed. Steady state responses for both positive and negative values of the rated torque are shown in Fig. 4.14 and Fig. 4.15 respectively.

With the positive torque, the magnitudes of both *dq*-axis currents and *abc* currents are similar to that of PCC. But the waveforms are smoother. Similarly, with negative torque there is a phase shift in *abc*-currents. From the plots it is clear that the proposed M^{2}PCC method has better steady state response than PCC comparatively.

4.3.3 Harmonic Analysis

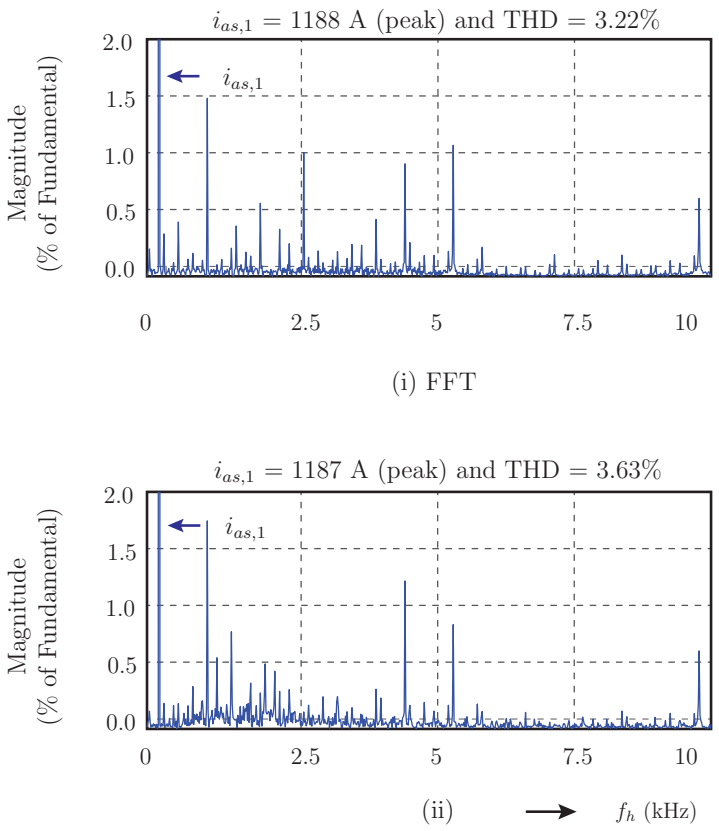

Figure 4.16: FFT analysis during rated speed condition for M^{2}PCC method : (i) at positive torque (SS1) and (ii) at negative torque (SS2).

Fig. 4.16 shows the FFT analysis on phase-a current during rated speed rated torque conditions with the proposed M^{2}PCC method . With the M^{2}PCC method, the harmonics are concentrated around the switching frequency ($1/T_c$ or 5000 Hz) and its multiples. With the fixed switching frequency operation, the THD of currents with M^{2}PCC method should be lower than the classical PCC method operating at twice the sampling frequency.

4.4 Comparison of Results

Table 4.2 shows the comparison between the classical PCC and proposed M^{2}PCC methods under steady-state. The sampling time T_s is set to 38 μs for classical PCC to increase the

Table 4.2: Comparison of steady-state performance

Case	Classical PCC (SS1)	Classical PCC (SS2)	Proposed M^{2}PCC (SS1)	Proposed M^{2}PCC (SS2)
f_{sw} (Hz)	4417	4688	5000	5000
$\%e_{is}$	3.76	3.30	3.81	3.54
rms i_{as} (A)	1191	1184	1188	1186
$\%\text{THD}_{is}$	4.43	4.21	3.22	3.63
$\%\text{WTHD}_{is}$	4.9	4.78	1.52	1.38

average switching frequency and to better compare it to the proposed control method. The switching frequency is fixed at 5000 Hz for M^{2}PCC method and is variable and less than 5000 Hz with classical PCC. The current tracking error, THD [60] and WTHD for the stator currents with M^{2}PCC method is lower than the classical PCC method during both steady-state conditions.

CHAPTER 5

CONCLUSIONS

EVs have proven their significance in the automobile sector with enormous growth in the last decade. The high reliability, high efficiency, and high-performance operation of PMSM made it the most popular choice for EV applications. The PMSM-based EVs are currently among the popular products of most EV manufacturers. In the EV industry, linear control methods are widely commercialized. The linear control exhibits fixed switching frequency operation and low steady-state errors; however, the transient response is sluggish. The sluggish dynamic response is unfavorable during wide dynamic-range operation of EVs. The MPC method was researched as a simple and best alternative to solve the sluggish dynamic response problem of classical linear control. However, the classical MPC method achieves fast transient response at the expense of high current ripple in steady-state and variable switching frequency operation. The works in this thesis solved the problems in the current literature by combining the operating principles of classical linear control and MPC methods, resulting more attractive and efficient controller for EVs. The developed control methods exhibit fast transient response as in the classical MPC, and fixed switching frequency operation and low steady-state error as in the classical linear control.

In this thesis, PCC and M^{2}PCC methods are developed and tested for the PMSM + 2L-VSI configuration for battery EV applications. The outcome of this research exhibited

that proposed control methods are best alternative to the classical linear control in EVs, which are highly sensitive to the parameter variations and nonlinearities caused by speed, torque, converters, and battery conditions. The research results presented in this thesis show that the proposed M^2PCC method outperforms the classical MPC method in terms of the current calculations, THD and WTHD for motor and stator currents, during all steady-state operating conditions. In contrast to the classical PCC method which applies a single voltage vector during entire sampling period, the proposed M^2PCC method applies more than one voltage vector to the traction inverter, leading to low current ripple. The simulation results prove the superiority of the proposed predictive control methods in extracting power from the battery and feeding to wheels with fast dynamic response and less steady-state error. With the proposed methods, the switching harmonics are concentrated around the converter switching frequency, which is a favorable characteristic to filter the harmonics easily.

The major contributions of this thesis are summarized as follows:

- **Control of the PMSM based EV with 2L-VSI:** In this thesis, M^{2}PCC method is developed for a 2L-VSI in PMSM based EVs. The developed controller optimized the motor cost function with two active and a zero voltage vectors and generated switching signals to the 2L-VSI through a SVM stage. The proposed control method fulfilled the control requirements such as speed control, torque control and dq-axis stator current control. The developed control method resulted in simultaneous fast transient response, smooth steady-state response and fixed switching frequency operation.
- **Comparison of Different Control Techniques of PMSM:** In this thesis, the comparison of results for various control methods are studied for both steady state and transient responses of PMSM. From this study it is explained how classical linear control of PMSM is more efficient in steady state condition, however with sluggish transient response. Similarly, for predictive current control, the transient response is faster, with high steady state error. The proposed M^{2}PCC method solved the drawbacks in the previous two control methods.

The following future research works are suggested as an extension to the knowledge presented in this thesis.

- Design of M^{2}PCC method for the NPC inverter.
- Design of modulated model predictive torque control method for the 2L-VSI.
- Design of modulated model predictive torque control method for the NPC inverter.
- Experimental validation of proposed control methods.

REFERENCES

[1] Jeffrey D Watkiss and Douglas W Smith. The energy policy act of 1992-a watershed for competition in the wholesale power market. *Yale J. on Reg.*, 10:447, 1992.

[2] Pierpaolo Cazzola, Marine Gorner, R Schuitmaker, and E Maroney. Global EV outlook 2016. *International Energy Agency, France*, 2023.

[3] Michael Liebreich. Bloomberg new energy finance summit. *London: Bloomberg New Energy Finance*, pages 1–10, 2017.

[4] Ali Emadi, Young Joo Lee, and Kaushik Rajashekara. Power electronics and motor drives in electric, hybrid electric, and plug-in hybrid electric vehicles. *IEEE Transactions on Industrial Electronics*, 55(6):2237–2245, 2008.

[5] David Wenzhong Gao, Chris Mi, and Ali Emadi. Modeling and simulation of electric and hybrid vehicles. *Proceedings of the IEEE*, 95(4):729–745, 2007.

[6] Ronald Jurgen. *Hybrid Electric Vehicles (HEV)*, pages 189–189. 2002.

[7] A. Emadi, K. Rajashekara, S.S. Williamson, and S.M. Lukic. Topological overview of hybrid electric and fuel cell vehicular power system architectures and configurations. *IEEE Transactions on Vehicular Technology*, 54(3):763–770, 2005.

[8] Alireza Khaligh and Zhihao Li. Battery, ultracapacitor, fuel cell, and hybrid energy storage systems for electric, hybrid electric, fuel cell, and plug-in hybrid electric vehicles: State of the art. *IEEE Transactions on Vehicular Technology*, 59(6):2806–2814, 2010.

[9] Sergio Vazquez, Srdjan M. Lukic, Eduardo Galvan, Leopoldo G. Franquelo, and Juan M. Carrasco. Energy storage systems for transport and grid applications. *IEEE Transactions on Industrial Electronics*, 57(12):3881–3895, 2010.

[10] H. Shimizu, J. Harada, C. Bland, K. Kawakami, and L. Chan. Advanced concepts in electric vehicle design. *IEEE Transactions on Industrial Electronics*, 44(1):14–18, 1997.

[11] Z. Q. Zhu and David Howe. Electrical machines and drives for electric, hybrid, and fuel cell vehicles. *Proceedings of the IEEE*, 95(4):746–765, 2007.

[12] Anurag M. Lulhe and Tanuja N. Date. A technology review paper for drives used in electrical vehicle (EV) & hybrid electrical vehicles (HEV). In *2015 International Conference on Control, Instrumentation, Communication and Computational Technologies (ICCICCT)*, pages 632–636, 2015.

[13] D. G. Dorrell, M. Popescu, L. Evans, D. A. Staton, and A. M. Knight. Comparison of permanent magnet drive motor with a cage induction motor design for a hybrid electric vehicle. In *The 2010 International Power Electronics Conference - ECCE ASIA -*, pages 1807–1813, 2010.

[14] Heping Liu, Youwei Zhou, Yu Jiang, Lin Liu, Tongbing Wang, and Bo Zhong. Induction motor drive based on vector control for electric vehicles. In *2005 International Conference on Electrical Machines and Systems*, volume 1, pages 861–865 Vol. 1, 2005.

[15] Zhang Qianfan, Cui Shumei, and Tian Xinjia. Hybrid switched reluctance motor applied in electric vehicles. In *2007 IEEE Vehicle Power and Propulsion Conference*, pages 359–363, 2007.

[16] Namitha Murali, S. Ushakumari, and Mini V. P. Performance comparison between different rotor configurations of PMSM for EV application. In *2020 IEEE REGION 10 CONFERENCE (TENCON)*, pages 1334–1339, 2020.

[17] A. Lesnicar and R. Marquardt. An innovative modular multilevel converter topology suitable for a wide power range. In *2003 IEEE Bologna Power Tech Conference Proceedings,*, volume 3, pages 6 pp. Vol.3–, 2003.

[18] J. Rodriguez, Jih-Sheng Lai, and Fang Zheng Peng. Multilevel inverters: a survey of topologies, controls, and applications. *IEEE Transactions on Industrial Electronics*, 49(4):724–738, 2002.

[19] Arvid Merkert, Tobias Krone, and Axel Mertens. Characterization and scalable modeling of power semiconductors for optimized design of traction inverters with Si- and SiC-devices. *IEEE Transactions on Power Electronics*, 29(5):2238–2245, 2014.

[20] Srdjan Srdic, Chi Zhang, and Srdjan Lukic. A low-inductance sectional busbar for snuberless operation of SiC-based EV traction inverters. In *2019 IEEE Energy Conversion Congress and Exposition (ECCE)*, pages 6805–6809, 2019.

[21] Z. John Shen and Ichiro Omura. Power semiconductor devices for hybrid, electric, and fuel cell vehicles. *Proceedings of the IEEE*, 95(4):778–789, 2007.

[22] EV extend - inverter kit for 2018-2023 Nissan Leaf, 2018.

[23] Different types of EV batteries: Greencars, 2023.

[24] Habib-ur Rehman and Longya Xu. Alternative energy vehicles drive system: Control, flux and torque estimation, and efficiency optimization. *IEEE Transactions on Vehicular Technology*, 60(8):3625–3634, 2011.

[25] Hassam Muazzam, Mohamad Khairi Ishak, Athar Hanif, A.I. Bhatti, Nor Ashidi Mat Isa, and Muhammad Nasiruddin Mahyuddin. Vector control of IPMSM used in electric vehicles. In *2022 13th Asian Control Conference (ASCC)*, pages 1317–1321, 2022.

[26] Matthew Liam De Klerk and Akshay Kumar Saha. A comprehensive review of advanced traction motor control techniques suitable for electric vehicle applications. *IEEE Access*, 9:125080–125108, 2021.

[27] Ahmed Salem and Mehdi Narimani. A review on multiphase drives for automotive traction applications. *IEEE Transactions on Transportation Electrification*, 5(4):1329–1348, 2019.

[28] Tomokazu Mishima, Kouhei Akamatsu, and Mutsuo Nakaoka. A high frequency-link secondary-side phase-shifted full-range soft-switching PWM DC-DC converter with ZCS active rectifier for EV battery chargers. *IEEE Transactions on Power Electronics*, 28(12):5758–5773, 2013.

[29] Md. Abdus Samad Kamal, Masakazu Mukai, Junichi Murata, and Taketoshi Kawabe. Model predictive control of vehicles on urban roads for improved fuel economy. *IEEE Transactions on Control Systems Technology*, 21(3):831–841, 2013.

[30] Mehrdad Ehsani, Krishna Veer Singh, Hari Om Bansal, and Ramin Tafazzoli Mehrjardi. State of the art and trends in electric and hybrid electric vehicles. *Proceedings of the IEEE*, 109(6):967–984, 2021.

[31] Jos Rodriguez, Jorge Pontt, Csar A. Silva, Pablo Correa, Pablo Lezana, Patricio Cortes, and Ulrich Ammann. Predictive current control of a voltage source inverter. *IEEE Transactions on Industrial Electronics*, 54(1):495–503, 2007.

[32] Shajjad Chowdhury, Patrick Wheeler, Zhen Huang, Marco Rivera, and Chris Gerada. Fixed switching frequency predictive control of an asymmetric source dual inverter system with a floating bridge for multilevel operation. *IET Power Electronics*, 12(3):450–457, 2019.

[33] L. Malesani, P. Mattavelli, and S. Buso. Robust dead-beat current control for PWM rectifiers and active filters. *IEEE Transactions on Industry Applications*, 35(3):613–620, 1999.

[34] Luca Tarisciotti, Pericle Zanchetta, Alan Watson, Jon C. Clare, Marco Degano, and Stefano Bifaretti. Modulated model predictive control for a three-phase active rectifier. *IEEE Transactions on Industry Applications*, 51(2):1610–1620, 2015.

[35] Luca Tarisciotti, Andrea Formentini, Alberto Gaeta, Marco Degano, Pericle Zanchetta, Roberto Rabbeni, and Marcello Pucci. Model predictive control for shunt active filters with fixed switching frequency. *IEEE Transactions on Industry Applications*, 53(1):296–304, 2017.

[36] M. Jankovic, P. Ninkovic, and Z. Janda. A novel approach to current-mode control of the constant frequency power converters. In *Proceedings of IEEE International Symposium on Industrial Electronics*, volume 1, pages 488–492 vol.1, 1996.

[37] Jiayang Wu, Sinan Li, Siew-Chong Tan, and S. Y. Ron Hui. Capacitor-clamped llc resonant converter for constant power EV charging with fixed operation frequency. In *2020 IEEE Applied Power Electronics Conference and Exposition (APEC)*, pages 3478–3483, 2020.

[38] Xue Li, Jiuchun Jiang, Caiping Zhang, Le Yi Wang, Linfeng Zheng, et al. Robustness of soc estimation algorithms for EV lithium-ion batteries against modeling errors and measurement noise. *Mathematical Problems in Engineering*, 2015, 2015.

[39] Omar Hegazy, Joeri Van Mierlo, and Philippe Lataire. Analysis, modeling, and implementation of a multidevice interleaved DC/DC converter for fuel cell hybrid electric vehicles. *IEEE Transactions on Power Electronics*, 27(11):4445–4458, 2012.

[40] Sungwoo Lee, Bohwan Choi, and Chun T Rim. Dynamics characterization of the inductive power transfer system for online electric vehicles by laplace phasor transform. *IEEE Transactions on Power Electronics*, 28(12):5902–5909, 2013.

[41] Matthias Preindl and Silverio Bolognani. Model predictive direct torque control with finite control set for PMSM drive systems, Part 1: Maximum torque per ampere operation. *IEEE Transactions on Industrial Informatics*, 9(4):1912–1921, 2013.

[42] S. Morimoto, K. Hatanaka, Y. Tong, Y. Takeda, and T. Hirasa. Servo drive system and control characteristics of salient pole permanent magnet synchronous motor. *IEEE Transactions on Industry Applications*, 29(2):338–343, 1993.

[43] Lizhi Qu, Liyan Qu, and Wei Qiao. A linear active disturbance rejection controller-based sensorless control scheme for PMSM drives. In *2019 IEEE Energy Conversion Congress and Exposition (ECCE)*, pages 792–797, 2019.

[44] Ping Lin, Zhen Wu, Kun-Zhi Liu, and Xi-Ming Sun. A class of linear–nonlinear switching active disturbance rejection speed and current controllers for PMSM. *IEEE Transactions on Power Electronics*, 36(12):14366–14382, 2021.

[45] Branko Majmunović, Tomislav Dragičević, and Frede Blaabjerg. Multi objective modulated model predictive control of stand-alone voltage source converters. *IEEE Journal of Emerging and Selected Topics in Power Electronics*, 8(3):2559–2571, 2020.

[46] M. Rivera, F. Morales, C. Baier, J. Muñoz, L. Tarisciotti, P. Zanchetta, and P. Wheeler. A modulated model predictive control scheme for a two-level voltage source inverter. In *2015 IEEE International Conference on Industrial Technology (ICIT)*, pages 2224–2229, 2015.

[47] Hamid Mahmoudi, Mohsen Aleenejad, and Reza Ahmadi. Torque ripple minimization for a permanent magnet synchronous motor using a modified quasi-Z-source inverter. *IEEE Transactions on Power Electronics*, 34(4):3819–3830, 2019.

[48] Cristian Garcia, Jose Rodriguez, Shafiq Odhano, Pericle Zanchetta, and S. Alireza Davari. Modulated model predictive speed control for PMSM drives. In *2018 IEEE International Conference on Electrical Systems for Aircraft, Railway, Ship Propulsion and Road Vehicles & International Transportation Electrification Conference (ESARS-ITEC)*, pages 1–6, 2018.

[49] L. Bigarelli, A. Lidozzi, M. Di Benedetto, L. Solero, S. Odhano, and P. Zanchetta. Modulated optimal model predictive control for variable speed gen-sets. In *2018 IEEE Energy Conversion Congress and Exposition (ECCE)*, pages 6859–6865, 2018.

[50] Fan Zhang, Tao Peng, Hanbing Dan, Jianheng Lin, and Mei Su. Modulated model predictive control of permanent magnet synchronous motor. In *2018 IEEE International Conference on Industrial Electronics for Sustainable Energy Systems (IESES)*, pages 130–133, 2018.

[51] Cristian F. Garcia, Cesar A. Silva, Jose R. Rodriguez, Pericle Zanchetta, and Shafiq A. Odhano. Modulated model-predictive control with optimized overmodulation. *IEEE Journal of Emerging and Selected Topics in Power Electronics*, 7(1):404–413, 2019.

[52] Venkata Yaramasu and Bin Wu. *Control of PMSG WECS with Back-to-Back Connected Converters*, pages 285–328. 2017.

[53] Ahmed M. Omara and Michael A. Sleptsov. Performance assessment of battery-powered electric vehicle employing PMSM powertrain system. In *2017 IEEE Conference of Russian Young Researchers in Electrical and Electronic Engineering (EIConRus)*, pages 963–968, 2017.

[54] Apparao Dekka, Bin Wu, Venkata Yaramasu, and Navid R Zargari. Integrated model predictive control with reduced switching frequency for modular multilevel converters. *IET Electric Power Applications*, 11(5):857–863, 2017.

[55] Olivier Tremblay. Parameters estimation and vector control of internal permanent magnet synchronous machine, 08 2008.

[56] Venkata Yaramasu and Bin Wu. *Overview of Digital Control Techniques*, pages 91–116. 2017.

[57] V Yaramasu. Predictive control of multilevel converters for megawatt wind energy conversion systems. *Ryerson University*, 2014.

[58] Venkata Yaramasu and Bin Wu. *Modeling of Power Converters for Model Predictive Control*, pages 149–176. 2017.

[59] Sergio Vazquez, Carlos Montero, Carlos Bordons, and Leopoldo G Franquelo. Model predictive control of a VSI with long prediction horizon. In *2011 IEEE International Symposium on Industrial Electronics*, pages 1805–1810. IEEE, 2011.

[60] Marco Rivera, Venkata Yaramasu, Jose Rodriguez, and Bin Wu. Model predictive current control of two-level four-leg inverters—Part II: Experimental implementation and validation. *IEEE Transactions on Power Electronics*, 28(7):3469–3478, 2013.